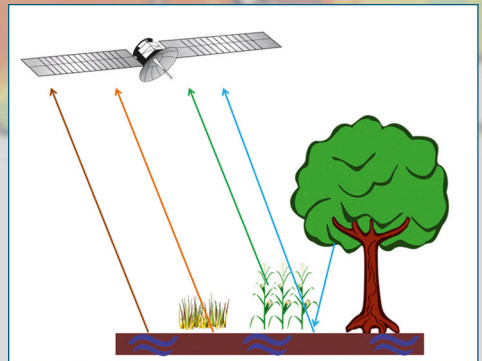


Statistical analysis and combination of active and passive microwave remote sensing methods for soil moisture retrieval

Kathrina Rötzer



Energie & Umwelt/
Energy & Environment
Band/ Volume 321
ISBN 978-3-95806-143-9

Forschungszentrum Jülich GmbH
Institute of Bio- and Geosciences
Agrosphere (IBG-3)

Statistical analysis and combination of active and passive microwave remote sensing methods for soil moisture retrieval

Kathrina Rötzer

Schriften des Forschungszentrums Jülich
Reihe Energie & Umwelt / Energy & Environment

Band / Volume 321

ISSN 1866-1793

ISBN 978-3-95806-143-9

Bibliographic information published by the Deutsche Nationalbibliothek.
The Deutsche Nationalbibliothek lists this publication in the Deutsche
Nationalbibliografie; detailed bibliographic data are available in the
Internet at <http://dnb.d-nb.de>.

Publisher and
Distributor: Forschungszentrum Jülich GmbH
Zentralbibliothek
52425 Jülich
Tel: +49 2461 61-5368
Fax: +49 2461 61-6103
Email: zb-publikation@fz-juelich.de
www.fz-juelich.de/zb

Cover Design: Grafische Medien, Forschungszentrum Jülich GmbH

Printer: Grafische Medien, Forschungszentrum Jülich GmbH

Copyright: Forschungszentrum Jülich 2016

Schriften des Forschungszentrums Jülich
Reihe Energie & Umwelt / Energy & Environment, Band / Volume 321

D 5 (Diss., Bonn, Univ., 2016)

ISSN 1866-1793
ISBN 978-3-95806-143-9

The complete volume is freely available on the Internet on the Jülicher Open Access Server (JuSER)
at www.fz-juelich.de/zb/openaccess.



This is an Open Access publication distributed under the terms of the [Creative Commons Attribution License 4.0](https://creativecommons.org/licenses/by/4.0/),
which permits unrestricted use, distribution, and reproduction in any medium, provided the original work is properly cited.

Abstract

Knowledge about soil moisture and its spatio-temporal dynamics is essential for the improvement of climate and hydrological modeling, including drought and flood monitoring and forecasting, as well as weather forecasting models. In recent years, several soil moisture products from active and passive microwave remote sensing have become available with high temporal resolution and global coverage. However, for the improvement of a soil moisture product and for its proper use in models or other applications, validation and evaluation of its spatial and temporal patterns are of great importance.

In chapter 2 the Level 2 Soil Moisture and Ocean Salinity (SMOS) soil moisture product and the Advanced Scatterometer (ASCAT) surface soil moisture product are validated in the Rur and Erft catchments in western Germany for the years 2010 to 2012 against a soil moisture reference created by a hydrological model, which was calibrated by in situ observations. Correlation with the modeled soil moisture reference results in an overall correlation coefficient of 0.28 for the SMOS product and 0.50 for ASCAT. While the correlation of both products with the reference is highly dependent on topography and vegetation, SMOS is also strongly influenced by radiofrequency interferences in the study area. Both products exhibit dry biases as compared to the reference. The bias of the SMOS product is constant in time, while the ASCAT bias is more variable. For the investigation of spatio-temporal soil moisture patterns in the study area, a new validation method based on the temporal stability analysis is developed. Through investigation of mean relative differences of soil moisture for every pixel the temporal persistence of spatial patterns is analyzed. Results indicate a lower temporal persistence for both SMOS and ASCAT soil moisture products as compared to modeled soil moisture. ASCAT soil moisture, converted to absolute values, shows highest consistence of ranks and therefore most similar spatio-temporal patterns with the soil moisture reference, while the correlation of ranks of mean relative differences is low for SMOS and relative ASCAT soil moisture products.

Chapter 3 investigates the spatial and temporal behavior of the SMOS and ASCAT soil moisture products and additionally of the ERA Interim product from a weather forecast model reanalysis on global scale. Results show similar temporal patterns of the soil moisture products, but high impact of sensor and retrieval types and therefore higher deviations in absolute soil moisture values. Results are more variable for the spatial patterns of the soil moisture products: While the global patterns are similar, a ranking of mean relative differences reveals that ASCAT and ERA Interim products show most similar spatial soil moisture patterns, while ERA and SMOS products show least similarities. Patterns are generally more similar between the products in regions with low vegetation. The relationships of spatial mean and spatial variance is influenced by sensor and retrieval characteristics

in the SMOS product, in particular during wet periods. For ASCAT and ERA products the major influencing factor was found to be the precipitation patterns of the respective regions. The impact factors on spatial variance were found to be highly dependent on the retrieval methods of the respective products. The investigation of the scaling properties of the soil moisture products shows that changes of support scales do not have an influence on the spatial variance for any of the products. Increasing extent areas lead to an increase of spatial variance for all products, in most cases, in particular for the ERA Interim product, according to a power law.

Chapter 4 focuses on the retrieval of vegetation parameters, as vegetation cover was found to be a major factor to reduce the accuracy of the soil moisture products in the previous chapters. One solution to deal with this problem is the use of additional sensor data. In addition to a radiometer the NASA Aquarius satellite offers a radar on the same platform. Therefore, Aquarius active microwave data are used to retrieve vegetation optical depth for further use in passive microwave soil moisture retrieval. A relationship between the Radar Vegetation Index (RVI), calculated from Aquarius radar backscattering coefficients and vegetation optical depth retrieved from brightness temperatures in the Land Parameter Retrieval Model (LPRM) is established on a global basis. This relationship is then used to calculate a new set of vegetation optical depth from RVI. It shows similar global spatial patterns as the original dataset and SMOS vegetation optical depth. In a selected region in the US Midwest, a closer examination of the newly derived vegetation optical depth is conducted. It was found to be able to reproduce the spatial and temporal patterns of the vegetation optical depth from LPRM. Furthermore, the influence of the vegetation optical depth derived from RVI on soil moisture retrieval is tested with the L-MEB model. A comparison to soil moisture retrieved with the original optical depth showed very similar results in terms of temporal and spatial patterns. This new method to derive vegetation optical depth from radar measurements will be an advantage for the new NASA Soil Moisture Active Passive (SMAP) mission, which consists of a radiometer and a radar, as optical depth can be calculated without time lag from observations of the satellite in the high resolution of the radar.

In general, this thesis analyzes the different accuracy levels of global soil moisture products and identifies the major influencing factors on this accuracy based on a small catchment example. On global scale, structural differences between soil moisture products were investigated, in particular the representation of spatial and temporal patterns as well as a general scaling law of soil moisture variability with extent scale. Both studies identified vegetation to have a high impact on accuracy. Therefore, an improved method to consider vegetation characteristics in soil moisture retrieval from satellite data was developed. The knowledge gained by this thesis will help to improve soil moisture retrieval of current and future microwave remote sensors, such as SMAP.

Zusammenfassung

Fundierte Kenntnisse über Bodenfeuchte und deren räumliche und zeitliche Dynamik sind von entscheidender Bedeutung für die Verbesserung von Klima- und hydrologischen Modellen, insbesondere zur Überwachung und Vorhersage von Dürren und Hochwassern, sowie auch für Wettervorhersagemodelle. In den letzten Jahren wurde eine Reihe von Bodenfeuchteprodukten aus Satellitendaten von aktiven und passiven Mikrowellensensoren entwickelt. Diese Produkte sind global und in hoher zeitlicher Auflösung verfügbar, jedoch sind Validierung und Evaluierung der räumlichen und zeitlichen Muster erforderlich zur Verbesserung dieser Bodenfeuchteprodukte und deren fachgemäße Verwendung in Modellen und anderen Anwendungsgebieten.

In Kapitel 2 werden die Bodenfeuchte des Soil Moisture and Ocean Salinity (SMOS) Level 2 Produkts und des Advanced Scatterometer (ASCAT) in den Einzugsgebieten von Rur und Erft im Westen Deutschlands für die Jahre 2010-2012 gegen eine modellierte Bodenfeuchtereferenz, die mit in situ-Messungen kalibriert wurde, validiert. Das SMOS Produkt zeigt eine generelle Korrelation von 0.28 mit der modellierten Referenz, das ASCAT Produkt einen Korrelationskoeffizienten von 0.50. Während bei beiden Produkten eine starke Abhängigkeit der Korrelation von Topographie und Vegetation besteht, zeigte das SMOS Produkt auch einen starken Einfluss von Frequenzinterferenzen im Untersuchungsgebiet. Beide Produkte weisen eine Abweichung gegenüber der feuchteren Referenz auf, die beim SMOS Produkt zeitlich stabil ist, und sich beim ASCAT Produkt deutlich variabler zeigt. Für die Untersuchung der räumlich-zeitlichen Muster der Bodenfeuchte im Untersuchungsgebiet wird eine neue Validierungsmethode basierend auf der „temporal stability analysis“ entwickelt. Ausgehend von der mittleren relativen Differenz der Bodenfeuchte für jedes Pixel wird die zeitliche Persistenz der räumlichen Muster untersucht. Im Vergleich zur modellierten Referenz zeigen die Ergebnisse eine kleinere zeitliche Persistenz der beiden Produkte. Das in absolute Bodenfeuchtwerte konvertierte ASCAT Produkt besitzt die höchste Übereinstimmung der Ränge der mittleren relativen Differenzen und damit die ähnlichsten räumlich-zeitlichen Muster im Verhältnis zur Referenz, während die Rangkorrelation der mittleren relativen Differenzen für SMOS und relative ASCAT-Werte gering ist.

Kapitel 3 untersucht das räumliche und zeitliche Verhalten der SMOS und ASCAT Bodenfeuchteprodukte sowie des Bodenfeuchteproduktes von ERA Interim, einer Reanalyse eines Wettervorhersagemodells auf globaler Skala. Die drei Bodenfeuchteprodukte zeigen ähnliche zeitliche Muster, aber auch einen starken Einfluss vom Sensortyp und von der Methode zur Ableitung der Bodenfeuchte aus den Messdaten und damit hohe Abweichungen in den absoluten Werten. Die Untersuchung der räumlichen Muster zeigte variabelere Ergebnisse: Während alle Produkte ein

ähnliches globales Verteilungsmuster aufweisen, zeigt eine Untersuchung der Rangkorrelation, dass die Muster der Produkte von ASCAT und ERA am ähnlichsten sind, während die Produkte von ERA und SMOS die geringste Übereinstimmung offenbaren. Im Allgemeinen gleichen sich die Muster der Bodenfeuchteverteilung bei den unterschiedlichen Produkten am stärksten in Regionen mit niedriger Vegetation. Die Beziehung von räumlichem Mittel und räumlicher Varianz der Bodenfeuchte wird beim SMOS Produkt von den Charakteristiken des Sensors und der Ableitungsmethode beeinflusst, besonders in nassen Perioden. Für die Produkte von ASCAT und ERA wurde als größter Einflussfaktor die zeitliche Niederschlagsverteilung ermittelt. Die Einflussfaktoren auf die räumliche Varianz stellten sich als stark abhängig von Sensortyp und Ableitungsmethode des jeweiligen Produkts heraus. Die Untersuchung von Skalierungseigenschaften zeigte keinen Einfluss des „support scale“ auf die räumliche Varianz der Produkte. Die Vergrößerung des „extent scale“ dagegen führte zu einem Anstieg der räumlichen Varianz aller Produkte, in den meisten Fällen, besonders beim ERA Produkt, gemäß einer Potenzfunktion.

Kapitel 4 beschäftigt sich mit der Ableitung von Vegetationsparametern, da sich die Vegetation in den vorherigen Kapiteln als einer der Haupteinflussfaktoren für die Reduktion der Genauigkeit der Bodenfeuchteprodukte erwiesen hat. Eine Möglichkeit der Herangehensweise an das Problem ist die Nutzung von zusätzlichen Sensordaten. Der NASA Satellit Aquarius bietet zusätzlich zu einem Radiometer einen Radarsensor. In dieser Studie werden Radardaten von Aquarius verwendet um die optische Dichte der Vegetation zu ermitteln, welche wiederum für die Ableitung der Bodenfeuchte aus den Radiometerdaten verwendet werden kann. Eine Beziehung zwischen dem Radar Vegetation Index (RVI), berechnet aus den Rückstreuoeffizienten von Aquarius, und der optischen Dichte der Vegetation, ermittelt aus den Strahlungstemperaturen von Aquarius im Land Parameter Retrieval Model (LPRM), wird auf globaler Basis etabliert. Dieser Zusammenhang wird dann genutzt um einen neuen Datensatz der optischen Dichte der Vegetation aus dem RVI zu berechnen. Die auf diese Weise ermittelte optische Dichte zeigt die gleichen globalen räumlichen Muster wie der Originaldatensatz und wie die optische Dichte des SMOS Produktes. In einem ausgewählten Gebiet im mittleren Westen der USA wird eine genauere Analyse der neu berechneten optischen Dichte durchgeführt. Es stellte sich heraus, dass es möglich ist die räumlichen und zeitlichen Muster der optischen Dichte aus dem LPRM zu reproduzieren. Außerdem wurde der Einfluss der aus dem RVI ermittelten optischen Dichte der Vegetation auf die Ableitung der Bodenfeuchte getestet. Ein Vergleich mit Bodenfeuchte, berechnet mit der optischen Dichte aus dem LPRM, zeigt ähnliche räumliche und zeitliche Muster. Diese neue Methode zur Berechnung der optischen Dichte aus Radarmessungen wird von Vorteil für die neue NASA Mission Soil Moisture Active Passive (SMAP) sein, die aus einem Radiometer und einem Radar besteht. Die optische Dichte der Vegetation kann

somit ohne Zeitverzögerung aus Beobachtungen des Satelliten in der hohen Auflösung des Radars abgeleitet werden.

Diese Arbeit analysiert die Genauigkeit von globalen Bodenfeuchteprodukten und identifiziert deren Haupteinflussfaktoren basierend auf dem Beispiel eines kleinen Einzugsgebiets. Auf globaler Skala werden die strukturellen Differenzen zwischen den Bodenfeuchteprodukten analysiert, besonders die Repräsentation von räumlichen und zeitlichen Mustern und ein generelles Potenzgesetz der Bodenfeuchtevarianz mit steigender Ausdehnung des Untersuchungsgebiets. Beide Studien zeigten einen hohen Einfluss der Vegetation auf die Genauigkeit der Bodenfeuchteprodukte. Deshalb wurde eine Methode zur verbesserten Bestimmung von Vegetationscharakteristiken bei der Ableitung der Bodenfeuchte aus Satellitendaten entwickelt. Die Erkenntnisse, die in dieser Arbeit gewonnen wurden, werden helfen die Bodenfeuchteprodukte aktueller und zukünftiger Mikrowellensensoren, zum Beispiel von SMAP, zu verbessern.

Content

Abstract	I
Zusammenfassung.....	III
Content.....	VI
List of Abbreviations & Symbols.....	X
List of Tables.....	XII
List of Figures.....	XIII
1 Introduction.....	1
1.1 Background & Motivation	1
1.2 Measuring soil moisture	2
1.3 Theory of soil moisture retrieval from remote sensing measurements	3
1.3.1 Passive microwave remote sensing	3
1.3.2 Active microwave remote sensing	5
1.3.3 Characteristics of remote sensing methods.....	6
1.4 Satellite sensors for soil moisture monitoring	7
1.5 Soil moisture retrieval algorithms	8
1.6 Methods for soil moisture product analysis.....	9
1.7 General aim and structure of the thesis.....	10
2 Catchment scale validation of SMOS and ASCAT soil moisture products using hydrological modeling and temporal stability analysis.....	12
2.1 Introduction.....	12
2.2 Material and Methods.....	15
2.2.1 Study area.....	15
2.2.2 Data	16
2.2.2.1 SMOS soil moisture product	16
2.2.2.2 ASCAT soil moisture product.....	18
2.2.2.3 In situ data.....	19

2.2.3	Methods	20
2.2.3.1	WaSiM-ETH.....	20
2.2.3.2	Correlation analysis	21
2.2.3.3	Temporal stability analysis	22
2.3	Results and Discussions	24
2.3.1	Validation of modeled soil moisture	24
2.3.2	Time series	25
2.3.3	Correlation coefficients and biases for the whole study area	29
2.3.4	Temporal stability analysis	34
2.4	Conclusions.....	38
3	Spatio-temporal variability of global soil moisture products	39
3.1	Introduction.....	39
3.2	Material and Methods.....	42
3.2.1	The Soil Moisture Products	42
3.2.1.1	SMOS Soil Moisture Product	42
3.2.1.2	ASCAT Soil Moisture Product	43
3.2.1.3	ERA Interim Soil Moisture	43
3.2.2	Study areas	44
3.2.3	Methods	48
3.2.3.1	Temporal Stability Analysis	48
3.2.3.2	Spatial variability and its time-variant and time-invariant contributors	49
3.2.3.3	Spatial scales of soil moisture	51
3.3	Results and Discussion.....	52
3.3.1	Global	52
3.3.1.1	Temporal means.....	52
3.3.1.2	Temporal stability.....	53
3.3.2	Selected regions	54

3.3.2.1	Time series of spatial mean.....	54
3.3.2.2	Spatial mean and variance	55
3.3.2.3	Contributions to the spatial variance.....	58
3.3.3	Scaling.....	61
3.4	Conclusions.....	68
4	Relationship of Vegetation Optical Depth and Radar Vegetation Index for the Aquarius mission.....	70
4.1	Introduction.....	70
4.2	Data and Methods	72
4.2.1	Data	72
4.2.1.1	Aquarius	72
4.2.1.2	IGBP	73
4.2.1.3	SMOS product	73
4.2.1.4	MODIS NDVI	74
4.2.2	Methods	74
4.2.2.1	RVI	75
4.2.2.2	LPRM.....	76
4.2.2.3	L-MEB	77
4.2.2.4	Sample area.....	78
4.3	Results and discussions	79
4.3.1	LPRM results.....	79
4.3.1.1	Vegetation optical depth.....	79
4.3.1.2	Soil moisture.....	81
4.3.2	Global Relationship for RVI and VOD	82
4.3.3	VOD derived from RVI	84
4.3.4	Performance of the optical depth retrieved from RVI in the sample area	86
4.4	Conclusions.....	92

5	Synthesis.....	93
5.1	Final Conclusions	93
5.2	Outlook	96
	Bibliography.....	97
	Acknowledgements.....	112

List of Abbreviations & Symbols

a	Area of scale
$A_{n,t}$	Temporal anomaly of soil moisture
AMSR	Advanced Microwave Scanning Radiometer
ASCAT	Advanced Scatterometer
c	Scaling law parameter
e	Emissivity
Γ	Vegetation transmissivity
$\delta_{n,t}$	Relative difference of soil moisture
$\bar{\delta}(n)$	Mean relative difference of soil moisture
ECMWF	European Centre for Medium Range Weather Forecast
ERA	ECMWF re-analysis
ESA	European Space Agency
h	Roughness height
IGBP	International Geosphere-Biosphere Programme
ISEA-4H9	Icosahedral Snyder Equal Area Earth Fixed (grid)
k	Dielectric constant
l	Correlation length
LAI	Leaf Area Index
L-MEB	L-band Microwave Emission of the Biosphere
LPRM	Land Parameter Retrieval Model
μ	Fractal power (of scaling law)
MPDI	Microwave Polarization Difference Index
MRD	Mean relative difference
NASA	National Aeronautics and Space Administration
NDVI	Normalized Difference Vegetation Index
ω	Single scattering albedo

Q	Polarization mixing factor
r	Reflectivity
RFI	Radio frequency interference
RMSE	Root mean square error
RMSD	Root mean square difference
RVI	Radar Vegetation Index
σ_0	Backscattering coefficient
$\sigma(\delta_i)$	Standard deviation of mean relative difference
$\sigma^2(t)$	Spatial variance of soil moisture
s	RMS height
SM	Soil moisture
SMAP	Soil Moisture Active Passive
SMOS	Soil Moisture and Ocean Salinity
SOMO PPF	Soil Moisture Product Processing Facility
τ	Vegetation optical depth
T	Physical temperature
TB	Brightness temperature
$\theta_{n,t}$	Soil moisture observation at location n and time t
$\bar{\theta}(n)$	Temporal mean soil moisture
$\bar{\theta}(t)$	Spatial mean soil moisture
u	Incidence angle
USCRN	US Climate Reference Network
VOD	Vegetation optical depth
VWC	Vegetation water content
WARP	Water Retrieval Package

List of Tables

Table 2.1: Correlation coefficients and biases of modeled soil moisture to SMOS and absolute and relative ASCAT soil moisture	30
Table 3.1: Description of study areas.....	47
Table 3.2: Slope (fractal power μ_s), intercept ($\log c_s$), and coefficient of determination (R^2) for support scale changes	63
Table 3.3: Slope (fractal power μ_e), intercept ($\log c_e$), and coefficient of determination (R^2) for extent scale changes.....	65
Table 4.1: Coefficients of the IGBP specific polynomials	84
Table 4.2: Biases between VOD_{RVI} and VOD_{LPRM} for different IGBP land use classes	86

List of Figures

Fig. 2.1: Location and land use of the study area the TERENO test sites	16
Fig. 2.2: Time series and scatterplots of in situ measurements and model results of soil moisture	25
Fig. 2.3: Time series of SMOS and modeled soil moisture.....	27
Fig. 2.4: Time series of absolute ASCAT and modeled soil moisture	28
Fig. 2.5: Time series of relative ASCAT and modeled soil moisture	28
Fig. 2.6: Correlation coefficients of modeled soil moisture with SMOS soil moisture, ASCAT absolute soil moisture, and ASCAT relative soil moisture for each pixel.....	29
Fig. 2.7: Influence of RFI on SMOS correlation coefficients.....	30
Fig. 2.8: Seasonal correlation coefficients and biases	32
Fig. 2.9: Bias of modeled soil moisture to SMOS soil moisture, ASCAT absolute soil moisture, and ASCAT relative soil moisture for each pixel	33
Fig. 2.10: Mean relative differences and their standard deviations (SMOS).....	35
Fig. 2.11: Mean relative differences and their standard deviations (ASCAT absolute)	35
Fig. 2.12: Mean relative differences and their standard deviations (ASCAT relative).....	35
Fig. 2.13: Comparison of ranks of the MRDs.....	37
Fig. 3.1: Köppen-Geiger climate classes and selected regions.....	44
Fig. 3.2: Climate charts for stations in the selected study regions	46
Fig. 3.3: Location and sizes of areas for support and extent scale studies with climate regions	48
Fig. 3.4: Temporal means over the whole study period	53
Fig. 3.5: Global correlation of ranks of MRDs for different climate zones	54
Fig. 3.6: Time series of spatial mean for the selected regions.....	55

Fig. 3.7: Relationship of $\theta(t)$ and $\sigma^2(t)$ of soil moisture for the selected regions.....	57
Fig. 3.8: Relationship of $\theta(t)$ and $\sigma^2(t)$ for in situ measurements.....	58
Fig. 3.9: Time series of percentages of the single contributors to $\sigma^2(t)$ for the selected regions.....	60
Fig. 3.10: Relationship of support scale and extent scale area vs. $\sigma^2(t)$	62
Fig. 3.11: Temporal evolution of slope (fractal power μ_e) of the relationship log extent area vs. $\log \sigma^2(t)$	66
Fig. 3.12: Relationship of extent scale area vs. $\sigma^2(t)$	67
Fig. 4.1: Overview of the study concept.....	75
Fig. 4.2: Location and land use of the sample area.....	78
Fig. 4.3: Maps of VOD_{LPRM} , VOD_{SMOS} , NDVI and their biases, and correlations.....	80
Fig. 4.4: Maps of SM_{LPRM} , SM_{SMOS} , their biases and correlations	82
Fig. 4.5: Relationship of RVI and VOD_{LPRM}	83
Fig. 4.6: Maps of VOD_{RVI} and biases to VOD_{LPRM}	85
Fig. 4.7: Maps of the sample area showing VOD_{RVI} , VOD_{LPRM} , and VOD_{SMOS} and scatterplot of VOD_{LPRM} and VOD_{RVI}	87
Fig. 4.8: Time series of IGBP mean of optical depth	88
Fig. 4.9: Maps of the sample area showing $SM_{LMEB/RVI}$, $SM_{LMEB/LPRM}$, SM_{SMOS} , and SM_{LPRM}	89
Fig. 4.10: Time series of IGBP mean of soil moisture.....	90
Fig. 4.11: Maps of bias and correlation of $SM_{LMEB/LPRM}$ and $SM_{LMEB/RVI}$	91

1 Introduction

1.1 Background & Motivation

Soil moisture strongly impacts our climate system (Seneviratne *et al.*, 2010). It controls evaporation of water from soils and the transpiration of plants. Accordingly, it is a major influence factor on the land energy balance, as more than half of the total solar energy absorbed by land surfaces is used in the process of evapotranspiration (Trenberth *et al.*, 2009; Jung *et al.*, 2010). The amount of evapotranspiration influences the partitioning of incoming energy into latent and sensible heat fluxes, and therefore it is directly coupled to air temperature (Zhang *et al.*, 2009). This coupling effect has been shown to be important in particular in the occurrence of heat waves (Differbaugh *et al.*, 2007; Miralles *et al.*, 2014). Other processes are also influenced by soil moisture. Precipitation can be impacted by the soil water content, either by moisture recycling, meaning that evapotranspired water contributes directly to the amount of precipitation, or by indirect interactions like impacting the boundary-layer stability and the formation of precipitation. Through the advection of evaporated moisture even non-local feedbacks can be found (Rowell and Blondin, 1990). Surface heterogeneity of soil moisture also plays a role for the generation of mesoscale features and precipitation patterns (Koster *et al.*, 2003; Guillod *et al.*, 2015). In a variety of modeling studies the impact of soil moisture on large scale circulation patterns has been shown. Haarsma *et al.* (2009), for example, showed the effect of soil moisture on pressure systems during a heat wave, while Douville (2002) found a relevant impact on African monsoon.

The role of soil moisture for the continental water cycle is equally important through its high influence on various hydrological fluxes. Through evapotranspiration, which is highly influenced by soil moisture availability, 60 % of the land precipitation returns to the atmosphere (Oki and Kanae, 2006). Furthermore, soil moisture controls the partitioning of rainfall into runoff and infiltration. Saturation of the soil will increase runoff, increasing the possibility of soil erosion or floods (Kerr, 2006). Infiltration water influences groundwater recharge (Sophocleous, 2002) and the root water uptake of plants (Musters and Bouten, 2000), which again interacts with plant transpiration.

Moreover, biophysical processes, like the germination of seeds, plant growth and plant nutrition, microbial decomposition of soil organic matter or nutrient transformation in the root zone are also highly dependent on the availability of soil moisture (Bittelli, 2011). Thereby, droughts are strongly endangering food security (Sheffield *et al.*, 2014).

Soil moisture also takes influence on biochemical processes, such as the exchange of trace gases on land through its role for vegetation. The terrestrial carbon cycle, for example, is impacted by the amount of plant available soil water content through the coupling of plant transpiration and photosynthesis (Reichstein *et al.*, 2002).

Thus, a precise quantification of soil moisture is important for improving climate modeling and weather prediction models as well as land surface modeling. It is similarly important for the improvement of hydrological modeling, including runoff forecasting and natural risk assessment. A frequently used method for the application of soil moisture in models is through data assimilation, where the soil moisture content predicted by the model is updated when new observations are available (Reichle *et al.*, 2004). Information about soil moisture can be used for the monitoring of vegetation and can be beneficial for the modeling of infectious diseases, which are forced by weather and environmental parameters (Wagner *et al.*, 2013a).

1.2 Measuring soil moisture

There is a wide range of possibilities for soil moisture measurements on point scale, for example capacitance sensors, time domain reflectometry, electrical resistivity measurements, heat pulse sensors, fiber optic sensors or gravimetric sampling (Vereecken *et al.*, 2008). On the scale of headwater catchments, wireless soil moisture networks proved to provide good results (Bogena *et al.*, 2010). Cosmic ray sensors integrate soil moisture over a larger area, and hydrogeophysical methods, in particular ground penetrating radar, electromagnetic induction, and electrical resistivity tomography provide information about a larger soil volume than point measurements on field scale (Vereecken *et al.*, 2014). These methods, however, can be work intensive and costly, when high temporal and spatial coverage is required. Many applications, like land surface and weather forecast models, require large scale or even global information about soil moisture. In sufficient temporal and spatial resolution, this information can only be provided by other models or satellite remote sensing.

Simulated global soil moisture products are available from different models: The Global Land Data Assimilation System (Rodell *et al.*, 2004) and the Integrated Forecast Model of the European Centre for Medium Range Weather Forecast (ECMWF), for example, provide operational analyses of soil moisture. From ECMWF, also long-term time series of soil water content, retrieved with a single version of the Integrated Forecast Model, are available. The ECMWF re-analyses (ERA) ERA 40 (Uppala *et al.*, 2005), ERA Interim (Dee *et al.*, 2011), and ERA Interim/Land (Balsamo *et al.*, 2015) give

consistent soil moisture data over the entire retrieval period (Albergel *et al.*, 2012), which is 1957-2002, 1979-present, and 1979-2010, respectively.

Remote sensing as well proved to be able to deliver the required soil moisture information with high coverage and in reasonable temporal and spatial resolution (Kerr, 2006). Remotely sensed soil moisture products were used for runoff forecasting (Scipal *et al.*, 2005) and the estimation of antecedent soil moisture conditions (Brocca *et al.*, 2009a). They were also applied for flood (Wanders *et al.*, 2014) and drought monitoring (Bolten *et al.*, 2010), in crop yield forecast models (de Wit and van Diepen, 2007) and for vegetation monitoring (Gouveia *et al.*, 2009). Another application is the modeling of infectious – for example mosquito-borne - diseases (Chuang *et al.*, 2012). Remotely sensed soil moisture products are assimilated into hydrological models for runoff forecasting (Brocca *et al.*, 2012), into weather prediction models (Scipal *et al.*, 2008; Muñoz-Sabater *et al.*, 2012), and into land surface models (Reichle and Koster, 2005).

Nevertheless, the coarse resolution of remotely sensed soil moisture products is a limiting factor for some application. Thus, several downscaling algorithms have been developed, most of them based on the application of visible and infrared remote sensing observations with high resolution (Merlin *et al.*, 2010; Piles *et al.*, 2011; Chakrabarti *et al.*, 2015).

1.3 Theory of soil moisture retrieval from remote sensing measurements

Currently, microwave remote sensing, both active and passive, is considered the best method for soil moisture retrieval from space (Wang and Qu, 2009). It is independent of illumination and of cloud conditions. Various remote sensing satellites differing in sensing technique (active/passive), frequency, and retrieval methods are used for the monitoring of soil moisture

1.3.1 Passive microwave remote sensing

The ability to retrieve soil moisture from passive microwave remote sensing, which measures the natural microwave radiation emitted from the soil, is based on the large differences of the dielectric constants of water (~80) and dry soil (~4) (Schmugge *et al.*, 1974; Njoku and Entekhabi, 1996). An increase of soil moisture will therefore lead to an increase of the complex dielectric constant, consisting of a real and an imaginary part. While the real part of the dielectric constant describes the propagation characteristics of energy passing upward, the imaginary part contains the energy losses.

The determination of the soil dielectric constant needs to take into account its single components, for example air, water and rock and influencing factors like temperature, salinity, and soil texture. Several models have been developed to calculate the complex soil dielectric constant. These models are generally empirical or semi-empirical and based on soil properties (Srivastava *et al.*, 2015). The Wang-Schmugge dielectric mixing model (Wang and Schmugge, 1980), for example, is an empirical model with a focus on the impact of bound water on the dielectric constant. The semi-empirical Dobson approach (Dobson *et al.*, 1985) considers the physical aspects of the dielectric properties of free water through the Debye equations and additionally uses fitting parameters from 5 soil types with sand fractions < 50 %. It is valid for a large range of microwave frequencies. The semi-empirical model of Mironov (Mironov *et al.*, 2009) is a generalized refraction dielectric mixing model. It is mineralogy-based and is validated for a large range of soil textures, including the ones of the Dobson model.

By knowing the dielectric constant of the soil, smooth surface reflectivity r_s can be determined through the Fresnel reflection equations by considering the incidence angle of satellite observations. Kirchhoff's law relates surface reflectivity to smooth surface emissivity e_s , which determines the soil radiation together with the physical temperature of the soil T_s [K]. Therefore, the soil microwave emission, expressed in brightness temperatures TB [K], can be approximated by

$$TB = e_s T_s \quad (1.1)$$

The smooth surface emissivity has to be corrected by surface roughness effects, as roughness increases surface scattering and therefore decreases reflectivity and increases emissivity. Rough surface emissivity e_r is most commonly calculated through the semi-empirical expression of Wang and Choudhury (1981), where surface roughness is described by the roughness height h and the polarization mixing factor Q

$$e_{rp} = [(1 - Q) r_{sp} + Q r_{sq}] \exp(-h \cos(u)) \quad (1.2)$$

with p and q denoting the polarization and u referring to the incidence angle of the observation.

Vegetation cover influences the microwave signal of the soil, which is measured by sensors above the canopy: It scatters and attenuates or absorbs the radiation from the soil, and it emits its own radiation and adds it to the soil signal. An increase of canopy height and density therefore leads to a

decrease of sensitivity of the measured signal for soil moisture (Jackson and Schmugge, 1991). The radiation measured by a microwave sensor from above a canopy can be expressed in the simple radiative transfer equation of the $\tau - \omega$ model of Mo *et al.* (1982), which is the basis for the forward simulation of brightness temperatures in most algorithms for soil moisture retrieval from passive microwave observation. It is given by

$$TB_p = e_r T_s \Gamma_p + (1 - \omega_p) T_c (1 - \Gamma_p) + (1 - \omega_p) T_c (1 - \Gamma_p) (1 - e_r) \Gamma_p \quad (1.3)$$

where T_c denotes the physical temperature of the vegetation canopy, while the vegetation is described through single scattering albedo ω and the vegetation transmissivity Γ . The first component of equation (1.3) describes the signal from the soil, attenuated through the vegetation canopy. The second term defines the upward radiation emitted from the canopy layer. The third part accounts for the downward radiation from the vegetation, which is reflected by the soil surface and attenuated by the canopy layer before reaching the sensor. The vegetation transmissivity is defined in terms of vegetation optical depth τ as

$$\Gamma = \exp^{-\tau/\cos(u)} \quad (1.4)$$

Vegetation optical depth (VOD) depicts the attenuation of the soil radiation through the canopy layer and is linearly related to the vegetation water content (VWC, Jackson and Schmugge, 1991). VOD is furthermore dependent on sensing frequency and the geometrical structure of the vegetation (Njoku and Entekhabi, 1996), which is characterized by an empirically derived b-parameter according to frequency and vegetation type in the linear relationship with VWC (Van de Griend and Wigneron, 2004).

1.3.2 Active microwave remote sensing

Soil moisture retrieval from active microwave remote sensing is equally based on the contrast of the dielectric constants of water and dry soil (Dobson and Ulaby, 1986). A radar emits a microwave signal and measures the quantity of energy backscattered to the sensor. When the emitted energy reaches the soil surface, it can be scattered, transmitted or absorbed. The distribution of the quantities of these processes is controlled by the boundary conditions at the air-soil interface, for example surface roughness and slope, and by the dielectric properties of the soil. The complex dielectric permittivity of soil k can again be derived through a dielectric mixing model (see sec. 1.3.1). The air-soil interface

can be described through an empirical model or through a correlation function. The correlation function can be expressed by root mean square (RMS) height and correlation length (Oh *et al.*, 1992). Vegetation cover adds backscatter to the soil signal, and it can attenuate the soil signal through volume scattering. The vegetation layer can be described by the characterization of vegetation structure. A vegetation index derived directly from radar observations is for example the Radar Vegetation Index (RVI), which is calculated from backscattering coefficients of different polarizations (Kim and van Zyl, 2009). Another possibility for vegetation characterization is the use of the dielectric constant of vegetation or of VOD and VWC (Ulaby *et al.*, 1979). Total radar scattering cross-section σ_{pq}^t [dB] in polarization pq can therefore be described as

$$\sigma_{pq}^t = \sigma_{pq}^s(k, s, l) \exp(-\tau_{pq}(VWC)) + \sigma_{pq}^c(VWC) + \sigma_{pq}^{sc}(VWC, k, s, l) \quad (1.4)$$

where the first term represents the scattering cross-section of the soil surface σ_{pq}^s , attenuated by vegetation twice (downward and upward). The second term σ_{pq}^c determines the scattering cross-section volume of the vegetation canopy and the third part σ_{pq}^{sc} describes the scattering interactions between soil and vegetation. s and l refer to the RMS height and correlation length, respectively, of the correlation function for the soil surface.

1.3.3 Characteristics of remote sensing methods

In theory, L-band microwave observation (generally at 1.4 GHz) has several advantages for the estimation of soil moisture compared to measurements at higher frequencies (Kerr *et al.*, 2012; Vitucci *et al.*, 2013). The longer wavelength of L-band (15-30 cm, 1-2 GHz) compared to other operational systems (e.g. C-band: 3.8-7.5 cm, 4-8 GHz, X-band: 2.5-3.8 cm, 8-12 GHz) leads to a higher vegetation penetration depth (Njoku and Entekhabi, 1996) and a higher soil penetration depth, which is about 3-5 cm for L-band systems (Escorihuela *et al.*, 2010) and decreases to 0.5-2 cm for C-band systems (Wagner *et al.*, 1999a), depending on the moisture condition of the soil. Passive microwave remote sensing systems are in general less sensitive to the effects of surface roughness and vegetation structure than active systems (Kerr, 2006), leading to less noise in the passive observations. An advantage of active soil moisture remote sensing, however, is the generally higher energy level and therefore higher spatial resolution of current active sensors (Wang and Qu, 2009). Moreover, observations from active systems are less affected by radiofrequency interferences (RFI).

Contamination of a measured signal with RFI occurs, where signals from man-made sources are emitted in the protected band and mistakenly detected by the sensor. RFI occurrences are regularly detected in L-band, in particular over continental areas in Europe, South-Eastern Asia, and the Middle East (Daganzo-Eusebio *et al.*, 2013). Several strategies were developed to detect and mitigate RFI (Misra and Ruf, 2008; Oliva *et al.*, 2012; Piepmeier *et al.*, 2014).

1.4 Satellite sensors for soil moisture monitoring

Within the last years, a variety of missions, which can be used for soil moisture monitoring, were developed. Several remote sensing missions using radiometers are currently in service. The Advanced Microwave Scanning Radiometer 2 (ASMR-2) onboard the Global Change Observation Mission 1 - Water (Okuyama and Imaoka, 2015) and Windsat, the radiometer of the Coriolis mission (Gaiser *et al.*, 2004), measure at different frequencies between 6 and 37 GHz. AMSR-2 delivers two soil moisture products retrieved with different algorithms (Kim *et al.*, 2015). From Windsat, a soil moisture product is retrieved from 10.7, 18.7, and 37 GHz channels (Li *et al.*, 2010). The European Space Agency's (ESA) Soil Moisture and Ocean Salinity (SMOS) mission (Kerr *et al.*, 2001) is the first directly designed for the remote sensing of soil moisture. It carries a radiometer recording brightness temperatures at L-band on a three day basis. Its measuring performance is 0.8 to 3.0 K for the radiometric sensitivity with a spatial resolution of 30 to 50 km. (Kerr *et al.*, 2001).

Several active microwave sensors with different spectral resolutions are also applicable for soil moisture monitoring. There is the Advanced Land Observing Satellite-2 mission carrying a L-band radar (Rosenqvist *et al.*, 2007), and the RADARSAT 2 mission (Morena *et al.*, 2004), the Compact-SAR on the Radar Imaging Satellite (RISAT) (Misra *et al.*, 2013), and the synthetic aperture radar on Sentinel-1 (Torres *et al.*, 2012), measuring in C-band. The X-band radars TerraSAR-X (Werninghaus and Buckreuss, 2010) and Tandem-X (Krieger *et al.*, 2007) can also be used for soil moisture monitoring, when no vegetation covers the soil (Aubert *et al.*, 2011). The Advanced Scatterometer (ASCAT) is a real aperture radar operating in C-band onboard the MetOp satellite, a meteorological mission with a sun-synchronous orbit. A triplet of backscattering coefficients at three incidence angles is produced at every measurement with a spatial resolution of 25 to 50 km. Global coverage of the ASCAT is one to two days (Bartalis *et al.*, 2007; Naeimi *et al.*, 2009).

Aquarius (Le Vine *et al.*, 2007), a joint mission of National Aeronautics and Space Administration (NASA) and the Argentine Space Agency (Comisión Nacional de Actividades Espaciales), is primarily designed for measuring sea surface salinity, but a soil moisture product is also retrieved (Bindlish *et*

et al., 2015). Brightness temperatures and backscattering coefficients are recorded by a radiometer and a radar, both measuring at L-band. The instruments are arranged in a pushbroom configuration at three incidence angles and measure in a resolution of 100 km. The satellite achieves global coverage in 7 days.

The recently launched Soil Moisture Active Passive (SMAP) satellite (Entekhabi *et al.*, 2010) also consists of a radiometer and a radar, measuring in the same frequencies as Aquarius, but with a distinctly higher resolution of 3 km for the radar and 36 km of the radiometer in a single angle of 40° and a global coverage within 3 days. Three soil moisture products are available from this mission, one retrieved from the radar instrument (Das *et al.*, 2011; Das *et al.*, 2014), one from the radiometer, and a combined product in an intermediate resolution of 9 km.

1.5 Soil moisture retrieval algorithms

Soil moisture is derived from the observations of these missions through several different approaches. Retrieval from the passively sensed brightness temperatures is generally conducted by simulating brightness temperatures as close as possible to the observations and inversion to soil moisture. The inversion is based on the concept of Mo *et al.* (1982) for most of the approaches currently in operational use. There are different ways of accessing VOD in the algorithms. The Single Channel Algorithm (Mladenova *et al.*, 2014; Bindlish *et al.*, 2015) is applied for the retrieval of the Aquarius soil moisture product and is the baseline algorithm for the SMAP passive soil moisture product. It retrieves soil moisture from h-polarized brightness temperatures, while VOD is approached through its relationship to VWC obtained from auxiliary data. The SMOS retrieval algorithm (Kerr *et al.*, 2012) is mainly based on the L-band Microwave Emission of the Biosphere (L-MEB) model (Wigneron *et al.*, 2007). It retrieves soil moisture and VOD simultaneously from dual-polarization and multi-angular observations by minimizing a cost function. The retrieval of VOD requires an initialization value which is again taken from auxiliary data under use of the linear relationship to VWC. The Land Parameter Retrieval Model (LPRM, Owe *et al.*, 2001; Owe *et al.*, 2008) is for example used for soil moisture retrieval from AMSR-2 (Parinussa *et al.*, 2015) and for the ESA Climate Change Initiative soil moisture product (Dorigo *et al.*, 2015). Like the SMOS Level 2 processor, it retrieves soil moisture and VOD simultaneously, whereas it derives VOD analytically from the Microwave Polarization Difference Index (MPDI, Meesters *et al.*, 2005).

The algorithms available for active soil moisture remote sensing make use of quite variable approaches. The SMAP baseline algorithm is the Time-Series Data Cube Approach (Kim, S. *et al.*,

2012), a multichannel algorithm that inverts a forward scattering model and retrieves RMS height s and the dielectric constant by minimizing a cost function. Vegetation effects are quantified by auxiliary data or by the backscattering coefficient in HV-polarization, which is known to be vegetation sensitive. Other approaches suggest using a change detection method for retrieving soil moisture. The method of Kim and van Zyl (2009) retrieves volumetric soil moisture by assuming surface roughness and vegetation constant over a longer period of time than the changes in soil moisture. The ASCAT soil moisture product (Bartalis *et al.*, 2007) is also retrieved through a change detection approach. It uses the method of Wagner *et al.* (1999a), where the observed normalized backscattering coefficients are scaled between the lowest and highest backscattering coefficients of a long-term time-series. This results in an index between 0 and 1, stating the degree of saturation of the soil, which can be converted to absolute soil moisture values through wilting point and saturation point of the respective soil. The influence of the vegetation is determined through the long-term seasonal behavior of the relationship between backscattering coefficient and incidence angle.

For the SMAP mission, approaches to combine active and passive remote sensing observations to a merged soil moisture product with intermediate resolution are developed. The change detection method of Piles *et al.* (2009) is based on the linear dependence of change in backscattering coefficients on soil moisture change at the radiometer resolution and the temporal change in backscatter at radar resolution on the previous day soil moisture data. Zhan *et al.* (2006) developed a Bayesian merging approach, where radar measurements are used to downscale radiometer observations. The spatial variability technique of Das *et al.* (2011) blends radar measurements and radiometer-based soil moisture by using the linear dependence of backscatter change to soil moisture change. The statistical disaggregation approach of Das *et al.* (2014) is the current SMAP baseline algorithm. It is built on the correlation between temporal fluctuations of brightness temperatures and backscatter in simultaneous observations at the same incidence angle. Brightness temperatures are downscaled using fine-resolution backscattering coefficients and soil moisture is then retrieved from the downscaled brightness temperatures.

1.6 Methods for soil moisture product analysis

The diverse sensors and differences in the retrieval algorithms can introduce structural deviances, as well as errors in the soil moisture products. Therefore, the characterization and validation of the products is essential. However, the validation of global remotely sensed soil moisture products is difficult due to their coarse resolution. In situ measurements are mostly only available on point-scale

and are not available globally. Therefore, validation has to be conducted on single pixels with in situ point measurements or sensor networks (Jackson *et al.*, 2012). Other possibilities are the validation through modeled soil moisture (dall'Amico *et al.*, 2012; Jakkila *et al.*, 2014), through airborne remotely sensed data (dall'Amico *et al.*, 2013; Montzka *et al.*, 2013) or the comparison of several satellite remote sensing products (Parrens *et al.*, 2012; Leroux *et al.*, 2013). The most common validation method is the use of correlation metrics, of root means square error (RMSE) and bias to a reference soil moisture (Al Bitar *et al.*, 2012; Albergel *et al.*, 2012; Lacava *et al.*, 2012). Another approach is the assimilation of several soil moisture products into a model and the comparison of the performance metrics (Pan *et al.*, 2012).

While validation of the products with common metrics gives valuable information about the deviances of a product from another measurement, it does not evaluate the correct retrieval of the area-wide variability. Therefore, the evaluation of the spatial and temporal patterns of a soil moisture product also needs to be considered. The spatio-temporal variability can be addressed by a temporal stability analysis (Vachaud *et al.*, 1985) and by investigating the relationship of spatial mean and spatial variance. The concept of temporal stability is mainly used as a method to minimize locations of soil moisture measurements on field scale while retrieving the same information about soil moisture variability (Brocca *et al.*, 2009b; Cosh *et al.*, 2004; Zhao *et al.*, 2013), but the information can also be used to characterize the distribution of soil moisture in time and space. The relationship of spatial mean and spatial variance of soil moisture was mainly investigated on small scale until now and it was found to be varying in different study areas (Bell *et al.*, 1980; Famiglietti *et al.*, 1998; Famiglietti *et al.*, 1999; Brocca *et al.*, 2007). Differences of relationships are caused by a variety of factors like topography, radiation, soil characteristics, vegetation, and land use, with different strength of influence in the respective study areas.

1.7 General aim and structure of the thesis

Through the mentioned methods it is possible to exhibit the systematic and statistical characteristics of the investigated soil moisture product. These characteristics are important to be aware of in the selection process of one or more products for application. Through the knowledge about the products' performance and their structural differences on local and global scale, their applicability for a specific project can be evaluated. Moreover, the factors triggering errors and differences between the products can be identified. These factors and the problems they are inducing can then

be addressed and improvements can be made, for example through implementation of advanced parameterization in the retrieval algorithms.

This thesis analyzes two soil moisture products from different sensors on catchment scale and globally, presenting their structural differences and errors and investigating the origins of these errors. Finally, it approaches a new method combining data from two sensors to solve one big problem of soil moisture retrieval, the characterization of the vegetation layer influencing remotely sensed measurements.

The thesis is structured into three main parts. Chapter 2 focuses on the validation of SMOS and ASCAT soil moisture products on catchment scale. The validation is conducted in the Rur and Erft catchments in western Germany through a soil moisture reference created by a hydrological model. It investigates the performance of the two products in an area with heterogeneous land use and analyzes the influencing factors on possible deviances from the reference.

In chapter 3, the analysis of the same remotely sensed soil moisture products is enhanced to global scale, including additionally the modeled soil moisture product of the ERA Interim reanalysis. The temporal and spatial characteristics are analyzed globally and for selected regions within various climate regions based on the Köppen-Geiger climate classification (Peel *et al.*, 2007). In this chapter, structural and statistical differences of the products are analyzed and the factors leading to these differences are determined. The suitability of their application in specific regions is investigated. Furthermore, the effect of changing scales on the products is analyzed.

Chapter 4 focuses on the retrieval of vegetation parameters from active remote sensing, as vegetation was found to be a major drawback for the accuracy of the soil moisture products. The approach establishes a relationship between the RVI, calculated from Aquarius radar backscattering coefficients, and VOD, retrieved with the LPRM from Aquarius radiometer brightness temperatures on a global basis. This relationship is used to calculate a new set of VOD, which is then analyzed on its accuracy, taking into account SMOS VOD. Moreover, in a selected region, the influence of the VOD retrieved from RVI on soil moisture retrieval is tested.

Finally, chapter 5 summarizes the main conclusions of this work and gives a brief outlook on possible further research.

2 Catchment scale validation of SMOS and ASCAT soil moisture products using hydrological modeling and temporal stability analysis¹

2.1 Introduction

Soil moisture is a key factor both in climate and hydrology: Affecting soil evaporation and transpiration, it impacts the heat and mass transfers between soil and atmosphere. Moreover, it influences the partitioning of rainfall into runoff and infiltration. Thus, area-wide time series of soil moisture are important for climate and hydrological modeling such as flood forecasting, as well as for numerical weather prediction, for example at the ECMWF (Muñoz-Sabater *et al.*, 2012; Scipal *et al.*, 2008).

In situ soil moisture for a certain area and for a specific moment in time can be acquired through different measurement techniques like gravimetric sampling or TDR sensors (Vereecken *et al.*, 2014), but this is very time-consuming in case large areal coverage is needed. Using wireless sensor networks, it is possible to obtain time series of soil moisture from the field to the headwater catchment scale (Bogena *et al.*, 2010). However, for weather forecasting or hydrological applications representative soil moisture data for larger regions or even with global coverage is needed (Scipal *et al.*, 2008). Apart from modeling, the only way to provide soil moisture data at that scale is through remote sensing (Kerr, 2006).

Therefore, different sensors and methods have been tested for their applicability in soil moisture estimation, especially in the microwave region of the electromagnetic spectrum. Synthetic aperture radars, scatterometers and passive radiometers are the most important sensor types used for soil moisture applications (Fang and Lakshmi, 2014; Wang and Qu, 2009).

Currently operational sensors that are being used for retrieving soil moisture include the ASCAT onboard the meteorological satellite MetOp-A (Bartalis *et al.*, 2007) and the AMSR-2 on the Global Change Observation Mission - Water (Su *et al.*, 2013). Since the launch of the SMOS satellite, there is also a mission specifically designed for remote sensing of soil moisture (Kerr *et al.*, 2010). The

¹ Adapted from: Rötzer, K., Montzka, C., Bogena, H., Wagner, W., Kerr, Y.H., Kidd, R., Vereecken, H. (2014): Catchment scale validation of SMOS and ASCAT soil moisture products using hydrological modeling and temporal stability analysis. *J. Hydrol.* 519, 934–946.

combined active and passive instruments, Aquarius (Luo *et al.*, 2013) and the SMAP (Entekhabi *et al.*, 2010), which was launched recently, also provide soil moisture products.

The remote sensing based methods of soil moisture estimation are differing in their sensing technique (active or passive), in frequency and in retrieval method. Thus, the resulting soil moisture products show different spatial resolutions and characteristics. Although current C-band active systems can provide higher spatial resolutions (Wang and Qu, 2009) and are less affected by RFI, L-band radiometry presently is considered to be the most promising technique for the estimation of soil moisture (Kerr *et al.*, 2012), not only because of the higher soil penetration depth compared to higher frequencies, but also because of better vegetation penetration (Njoku and Entekhabi, 1996). Additionally, passive systems are less sensitive to the effects of surface roughness and vegetation structure than active systems (Kerr, 2006). Depending on sensing frequency, satellite measurements are valid for different soil volumes which again are reliant on a wide range of surface conditions. For C-band systems like ASCAT and AMSR-2, soil penetration depth is between 0.5 and 2 cm (Bartalis *et al.*, 2007; Naeimi *et al.*, 2009). L-band systems, like SMOS, Aquarius, and SMAP, have a higher average soil penetration depth in the range of about 3-5 cm (Escorihuela *et al.*, 2010).

However, since soil moisture remote sensing is influenced by a large number of factors (e.g. atmospheric conditions, vegetation, soil surface roughness etc.), the application and parameterization of retrieval methods is not straightforward. A wide range of retrieval methods has been developed, which produce different kinds of soil moisture products. For instance, a method for soil moisture retrieval from scatterometer data, which is based on change detection, was developed by Wagner *et al.* (1999a) for the European Remote Sensing Satellite. The resulting product consists of relative values of surface soil moisture. This method is now applied to ASCAT, the successor of this mission.

In contrast, retrieval of soil moisture from SMOS relies on a radiative transfer model, resulting in volumetric soil water content. The SMOS mission's main objective is to provide global maps of soil moisture with accuracy higher than $0.04 \text{ m}^3/\text{m}^3$ (Kerr *et al.*, 2001).

Covering large areas as compared to common ground measurements, which reveal high variability on small scales, validation of the soil moisture products is not straightforward. Nevertheless, point scale in situ measurements are often used for the examination of remotely sensed low resolution soil moisture. Al Bitar *et al.* (2012) and Jackson *et al.* (2012) found high correlation coefficients and low RMSE values as well as biases for the SMOS product (version 4.00) with in situ measurements from different sites spread over the United States. Bircher *et al.* (2013) discovered good capture of

precipitation and soil moisture dynamics, but a significant dry bias of SMOS compared to in situ data for the Skjern River Catchment in Denmark.

Another frequently applied option is the validation with modeled soil moisture, which accounts for the whole extent of a pixel. For example, dall'Amico *et al.* (2012) found low correlation coefficients between SMOS (version 4.00) and modeled soil moisture for the Upper Danube Catchment in Germany, with correlation of mostly below 0.3 and biases between 0.11 and 0.3 m³/m³. This was charged to the presence of RFI. Brocca *et al.* (2011) compared CDF-matched ASCAT surface soil moisture to in situ and modeled data of test sites of four different European countries and found correlation coefficients between 0.64 and 0.81 and an average root mean square difference (RMSD) of 0.143 for relative soil moisture.

Albergel *et al.* (2012) compared SMOS (version 4.00) and ASCAT products to in situ soil moisture from more than 200 stations in Africa, Australia, Europe, and the United States. They found a generally good performance of both products, with slightly higher performances of ASCAT: Normalized time series of SMOS and in situ data showed an overall correlation coefficient of 0.55 (bias: 0.122, RMSD: 0.243), for ASCAT the correlation coefficient was 0.55 (bias: 0.056, RMSD: 0.247). In all studies moderate to large dry biases for the SMOS soil moisture were observed.

In order to facilitate a comparison with the aforementioned validation studies, we used the same correlation and bias statistics for the validation of the SMOS and ASCAT soil moisture products. In addition, we introduced temporal stability analysis as a method for spatio-temporal validation through a rank stability correlation. Until now, the temporal stability concept was mainly used as a method to minimize locations of soil moisture measurements on field scale through finding a reduced number of sampling locations which are representative for the whole area (Brocca *et al.*, 2009b; Cosh *et al.*, 2004; Vachaud *et al.*, 1985; Zhao *et al.*, 2013). An overview of applications of temporal stability, methods for the analysis and influence factors is given in Vanderlinden *et al.* (2012).

In this study, we analyzed the SMOS Level 2 soil moisture product (SMOS Level 2 Processor, version 5.51) and time series of soil moisture derived from ASCAT (Water Retrieval Package (WARP) software, version 5.5) of the years 2010 to 2012 for the Rur and Erft catchments in Germany by using soil moisture information derived from the hydrological model WaSiM-ETH as reference data. Modeled reference, validated by in situ data, was used rather than in situ data to account for the different spatial resolutions of the soil moisture products. Another advantage is the possibility to study a larger area with several pixels, although in situ measurements are not available for all of these pixels. Furthermore, the temporal stability analysis method developed by Vachaud *et al.* (1985)

was introduced as an advanced validation approach. This method was used to determine the ability of a sensor to capture the spatial and temporal soil moisture patterns rather than absolute values. With this approach the information content of the soil moisture signal can be evaluated without the influence of a potential bias.

In the following section, the SMOS and ASCAT soil moisture products, the model used to calculate the reference data and the method of the temporal stability analysis are described. Sec. 2.3.1 validates the soil moisture reference through in situ data, sec. 2.3.2 and 2.3.3 analyze the individual accuracy of both SMOS and ASCAT soil moisture products and their suitability for the further use in numerical weather prediction and hydrological modeling by comparing them to the soil moisture reference. Finally, sec. 2.3.4 discusses the results of the temporal stability analysis and its use as a validation method.

2.2 Material and Methods

2.2.1 Study area

The study area is located in the west of Germany in the region next to the Belgian-Dutch-German border and contains the catchments of the rivers Rur and Erft (Montzka *et al.*, 2013). It covers a total area of 4125 km². The river Rur originates in the Eifel Mountains, discharges into the river Maas and has a total length of 165 km, while the river Erft is a tributary of the Rhine and has a length of 107 km (Bogena *et al.*, 2005). The study area can be divided into a northern and a southern part (Fig. 2.1). The northern region is rather plain. It has a relatively low annual long-term precipitation of 650-850 mm, while annual potential evapotranspiration ranges from 580 to 600 mm. As the soils mainly evolved from loess, which accumulated on Tertiary and Quaternary depositions of Rhine and Maas, and the principal land use type is agricultural land (Montzka *et al.*, 2008a). The southern part is located in the Eifel low mountain range. Annual long-term precipitation is higher than in the northern part due to the mountainous influence with 850 – 1300 mm, while annual potential evapotranspiration shows moderate values of 450 - 550 mm. The bedrock consists of Devonian and Carboniferous sedimentary rocks with low permeability and small groundwater storage volumes, causing high interflow and low groundwater runoff rates. Here, the predominant land use types are forest and grassland.

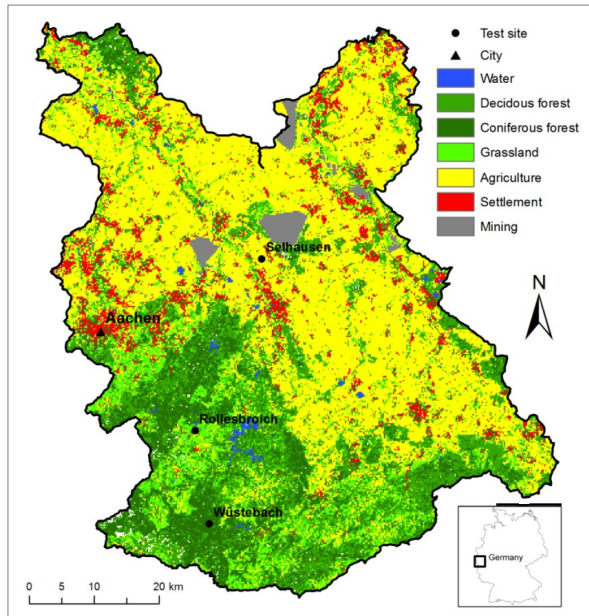


Fig. 2.1: Location and land use of the study area the TERENO test sites.

2.2.2 Data

2.2.2.1 SMOS soil moisture product

Launched in 2009, SMOS is a sun-synchronous orbiting satellite operating at an altitude of 755 km. The radiometer system onboard SMOS records two-dimensional brightness temperatures in the L-band at 1.4 GHz on a three day basis. Its measuring performance is 0.8 to 3.0 K for the radiometric sensitivity with a spatial resolution of 30 to 50 km. (Kerr *et al.*, 2001).

In this study we used the SMOS soil moisture product of 2010 -2012, produced in the SMOS Level 2 Processor version 5.51. The products are provided on the ISEA-4H9 (Icosahedral Snyder Equal Area Earth Fixed) grid with approximately 15 km distance between grid points.

The Level 2 processor (Kerr *et al.*, 2012) is a physically based algorithm applying Level 1C product brightness temperature at different incidence angles as input. In addition, the processor uses different kinds of auxiliary data: static data like land use and soil texture maps and dynamic data, such as snow or temperature, which are obtained from ECMWF forecasts.

For the retrieval of soil moisture for one pixel a working area of 123 x 123 km is set up, which is considered to be the maximum extent contributing to the SMOS signal. The portions of contributions

are determined through weighing by the antenna pattern. In many cases, different kinds of land use are present in the working area and contribute to the measured brightness temperature. To account for that, the different land use types are determined and their fractions are estimated. Retrieval of state variables like soil moisture, but also VOD and the dielectric permittivity, only takes place for the dominant fraction, the largest fraction of study area. For the remaining land use classes default models calculate the state of the variables. The default models are only driven with physical parameters obtained from auxiliary data and there may be small differences from the retrieval models. These default contributions are assumed to be constant and stay fixed during retrieval, their contributions to the measured brightness temperatures are determined according to their cover fractions. Thus, the retrieved soil moisture is only valid for the dominant cover fraction.

In a decision tree the forward model for the dominant fraction is chosen. For the nominal case, a low vegetated pixel without snow cover, and for the forest case, the forward models are based on the τ - ω approach (Mo *et al.*, 1982). τ and ω hereby refer to the VOD and the single scattering albedo, respectively. For calculation of the atmospheric contribution, molecular oxygen, water vapour, clouds, and rain are taken into account through an absorption coefficient (Kerr *et al.* 2011). Bare soil emission is simulated using Fresnel laws, whereby the Mironov semi-physical model (Mironov *et al.*, 2009) is used for the determination of dielectric permittivity. It was first implemented in the Level 2 Processor version 5.51, replacing the Dobson semi-empirical model (Dobson *et al.*, 1985). Surface roughness is taken into account through the correction of the smooth soil reflectivity with the empirical relationship of Wang and Choudhury (1981), as proposed by Escorihuela *et al.* (2007).

The chosen forward model aims to minimize a cost function through minimizing the sum of squared weighted differences between modeled brightness temperature and the measured brightness temperature of the dominant soil cover type (Kerr *et al.*, 2012).

For this study only data from ascending overpasses were used to prevent from influences concerning differences between morning and evening overpasses as reported in Rowlandson *et al.* (2012). Through threshold filtering with the soil moisture data quality index $SM_DQX > 0.06$ outliers were removed. All data were tested on raised flags in the snow and frost occurrence, and where flags were raised the data were removed. Additionally, the data were tested on the influence of RFI through the confidence flags $FL_RFI_Prone_H$ and $FL_RFI_Prone_V$. The retrieval cases for all pixels in the study area are nominal for most time of the year, only in late autumn, winter and early spring sometimes cases for snow retrieval were identified.

2.2.2.2 ASCAT soil moisture product

ASCAT is a real aperture radar onboard the MetOp-A satellite operating in the C-band at 5.255 GHz. A triplet of backscattering coefficients at three incidence angles is produced within every measurement. The satellite has a sun-synchronous orbit in an altitude of 837 km. Coverage is almost daily with a spatial resolution of 25 to 50 km (Bartalis *et al.*, 2007; Naeimi *et al.*, 2009).

Time series of relative soil moisture for the years 2010 - 2012 were retrieved from 25 km resolution ASCAT backscattering coefficients at Vienna University of Technology using the WARP 5.5 software. It is delivered on a discrete global grid with grid point distances of about 12.5 km.

The retrieval of relative soil moisture from ASCAT backscattering coefficients is based on the change detection method of Wagner *et al.* (1999a). First, the backscattering coefficients are resampled to a discrete global grid (Bartalis *et al.*, 2006a). Then, they are extrapolated to a reference incidence angle of 40° using a second order polynomial. The influence of the vegetation is determined through the relationship between backscattering coefficient and incidence angle. While the backscattering coefficient decreases with higher incidence angles, for both, bare and vegetated soil, backscattering is higher for bare soil than for vegetated soil at low incidence angles, but lower at high incidence angles. Thus, the curves of bare and vegetated soil will cross over at a specific angle. At this “crossover angle”, which is different for dry and wet conditions, the influence of vegetation is assumed to be least (Wagner *et al.*, 1999b). By considering the crossover angles, dry and wet reference backscattering coefficients are determined from long-term time series derived from the measurements of the European Remote Sensing satellites and ASCAT for every grid point. Finally, the dry and wet references are used for scaling the backscattering coefficients, assuming a linear relationship between the backscattering coefficient and surface soil moisture, and resulting in relative soil water content of the surface soil layer with values from 0 to 100 %, stating the degree of saturation of the topmost soil layer of 0.5 - 2 cm, as the extreme values of the backscattering coefficients are considered to represent a completely dry soil and saturated soil conditions of the grid point (Bartalis *et al.*, 2008).

Filtering of the ASCAT soil moisture product was done using the advisory flags provided with the soil moisture product. The flags are not derived from scatterometer data and contain information on snow and frozen soil probability. They are based on long-term climate information, the fraction of water, derived from the Global Lakes and Wetlands Database Level 3 product, and the topographic complexity representing the standard deviation of elevation from GTOPO30 data and normalized to values between 0 and 100 %. This information is given for every pixel. Snow and frost probability

have one value for every pixel and every day of the year (Bartalis *et al.*, 2008). The filtering included the removal of all data points for which the flags indicated the possibility of snow or frozen soil.

2.2.2.3 In situ data

In situ data from three different test sites within the study area were used to validate the hydrological model. The test sites are part of the Terrestrial Environmental Observatories (TERENO) initiative (Zacharias *et al.*, 2011), which are typical for the different land use types of the region and where in situ soil moisture is recorded on a regular basis. The location of the test sites is illustrated in Fig. 2.1.

The agricultural test site Selhausen is located in the northern part of the study area at an altitude of 102 – 110 m above sea level (a.s.l.), with a mean annual temperature of 9.8°C, and an average precipitation of 690 mm per year. Dominant soils are (gleyic) Cambisol and Luvisol. In situ soil moisture is obtained on permanently bare soil from three Stevens Hydra Probe sensors at soil depth of 4 cm and 7 cm in 10 minute resolution. For comparison with modeled soil moisture the mean of one hour, over the two depths, and of all three Hydra Probe sensors was taken. Data was available for the whole period of this study except October 2010.

Rollesbroich is a grassland site, located in the southern part of the study area and covering an area of 27 ha with altitudes ranging between 474 and 518 m a.s.l.. Mean annual temperature and precipitation are 7.7° C and 1033 mm, respectively. Main soils at this site are (gleyic) Cambisol, Stagnosol and Cambisol-Stagnosol. In situ soil moisture for April, May and June 2010 was measured every ten minutes using three CR 1000 Time Domain Reflectometry sensors at a depth of 10 cm. Hourly averages were taken over all sensors. Since May 2011 a wireless sensor network with 84 nodes covering 13 ha and using SPADE sensors (Qu *et al.*, 2013), provides soil moisture data every 15 minutes for three depths (5, 20 and 50 cm). In this study we used the spatial mean of hourly averaged measurements at 5 cm depth for the comparison with modeled soil moisture.

The third test site used in this study is the forest site Wüstebach covering an area of 38.5 ha. It is located in the southern part at an altitude of 600 m a.s.l. on average and has a mean annual precipitation of 1200 mm. The predominant soil type is cambisols (Montzka *et al.*, 2013). In situ data of the test site were obtained from a wireless sensor network of 600 EC-5 sensors and 300 5 TE sensors (Decagon Devices, Pullman, WA) covering an area of 27 ha and measuring soil moisture through capacitance method at 150 locations at three depths of 5, 20 and 50 cm (Rosenbaum *et al.*, 2012). The temporal measurement frequency was 15 minutes (Bogena *et al.*, 2010). For comparison

with modeled soil moisture we calculated the spatial mean of the hourly averaged measurements of all locations at a depth of 5 cm.

2.2.3 Methods

2.2.3.1 WaSiM-ETH

The grid-based hydrological model WaSiM-ETH version 8.8 (Schulla and Jasper, 2007) was used to calculate distributed hourly soil moisture of the study area for the years 2010 to 2012 with a horizontal spatial resolution of 200 m. A spin-up period of one year was used, which is appropriate given the fact that this study mainly focuses on the top soil moisture. The soil was discretized in different layers of which the topmost layer was chosen to be 0 - 5 cm, in order to take into account the penetration depth of C- and L-band microwave sensors. Since the sensors typically show smaller penetration depths for high soil moisture values, discrepancies during very wet soil conditions are expected.

Meteorological forcing data (Temperature, precipitation, relative humidity, sunshine duration and wind velocity) were obtained from 62 stations, mainly operated by the German Weather Service (DWD). 19 of these stations are located within the study area and 43 stations are within a maximum distance of 50 km to the study area. Precipitation is interpolated by height regression within the model. It is corrected separately for rain and snow, differentiated through a threshold temperature. For both cases there is a fixed correction parameter, while wind speed is used as a second correction term. Each of three height ranges is subdivided into 10 subranges, and temperature and wind speed are interpolated for the middle of each of these subranges. The correction equation is applied to the precipitation value of the center of the subranges. New height gradients are then calculated from the corrected precipitation. Height regression is also used for the interpolation of temperature, while wind speed, sunshine duration and relative humidity are interpolated by inverse distance weighting. Other input data were terrain elevation, taken from the Digital Elevation Model for North Rhine-Westphalia (DGM 25 NRW), and land use and degree of imperviousness, which were derived from multispectral satellite data of Landsat ETM+ (Montzka *et al.*, 2008a; Montzka *et al.*, 2008b). The soil hydraulic properties were derived from the Soil Information System of the Federal State of North Rhine-Westphalia with a scale of 1:50000.

WaSiM-ETH was developed to investigate the spatial and temporal variability of hydrological processes in complex river basins. It uses the approach of Peschke (1977) for the calculation of infiltration, which is based on the Green-Ampt method (Green and Ampt, 1911), and a discrete

formulation of the Richards equation for simulating water dynamic in the soil zone. The Richards equation is applied to predict the vertical flow of water in the unsaturated multi-layer soil zone between two soil layers. The hydraulic properties of the soil are calculated using the relations proposed by van Genuchten (1980): The soil water retention curve is estimated for different soil textures through five independent parameters (residual water content, saturated water content, and shape factors α , n , and m). A vertical one-dimensional finite difference scheme is applied to solve the Richards equation for a discrete soil layer. In the following step, vertical fluxes between the soil layers are calculated. Then interflow is generated, and after that exfiltration from groundwater into rivers and infiltration from rivers are calculated. The scheme starts with the lowest soil layer that was completely saturated at the last step or with the uppermost layer if there was no saturation in the last step. Upper boundary condition is the amount of infiltration and the lower boundary condition is the depth of the groundwater table. Removal of water for evapotranspiration is done at each time step before the soil water transport scheme starts.

Potential evapotranspiration is estimated through the Penman-Monteith equation (Monteith and Unsworth, 1990). Actual evapotranspiration is derived from potential evapotranspiration through a reduction approach that takes into account the influence of the soil water content. The model considers soil moisture changes induced by topographic gradients and fluctuations of the groundwater table. Minimum input data to the model are time series of temperature and precipitation as well as grid data on topography, land use and soil properties (Jasper *et al.*, 2006).

Validation of the model was carried out through in situ data of the TERENO sites within the study area, which are described in sec. 2.2.2.3.

2.2.3.2 Correlation analysis

Correlation analysis was performed on the filtered SMOS and ASCAT soil moisture products in relation to the soil moisture reference at the same area, which was averaged over the extent of the respective pixels. These pixels are produced by amplifying the area around the respective grid points by using a nearest neighbor method. Nevertheless, it has to be kept in mind that this is just an approximation of the area that influences the soil moisture value of this grid point.

As the modeled reference and the SMOS soil moisture product are both given in absolute volumetric soil moisture content, while the ASCAT product gives the relative saturation of the soil, a direct comparison is complicated. Thus, the latter was rescaled to volumetric values through multiplying the relative values with porosity data that are estimated from texture characteristics of the Harmonized World Soil Database with the equations of Saxton and Rawls (Saxton and Rawls 2006;

Wagner *et al.* 2013b). An additional comparison was performed with the original relative soil moisture values of the ASCAT product and relative modeled values. For this, the absolute modeled soil moisture was scaled between 0 and 1 using the minimum and maximum values of every grid cell. Pearson's correlation coefficients were calculated and tested on their significance; only correlation coefficients with $p < 0.05$ were used for this study. Bias was calculated through

$$bias = \frac{1}{M} \sum_{m=1}^M (SM_{mod} - SM_{sat}) \quad (2.1)$$

where m is the number of observation pairs and SM_{mod} and SM_{sat} are the modeled soil moisture and satellite soil moisture product, respectively. All studies were carried out for March to November of the respective years, as during winter not enough soil moisture product values were left after filtering (i.e. frozen conditions) to perform a reasonable statistical analysis.

In a separate analysis the influence of different numbers of observation on the correlation analysis was investigated. A statistically comparable control sample was created by counting the observations of the products and selected the same sampling size at random for every week. This resulted primarily in a reduced number of ASCAT observations, which is higher than the number of SMOS observations due to higher spatial and temporal resolution of the data. The correlation analysis for the whole study area was repeated with this dataset.

2.2.3.3 Temporal stability analysis

The temporal stability analysis was tested as a new method to validate soil moisture products.

To assess the temporal stability of the SMOS and ASCAT soil moisture products, mean relative differences (MRD) of every pixel and their standard deviations were calculated and ranked for the two products and their corresponding averaged modeled soil moisture according to the method of Vachaud *et al.* (1985). In this method the relative difference $\delta_{n,t}$ is calculated for every soil moisture value $\theta_{n,t}$ at location n and time t

$$\delta_{n,t} = \frac{\theta_{n,t} - \bar{\theta}(t)}{\bar{\theta}(t)} \quad (2.2)$$

where $\bar{\theta}(t)$ is the mean value over the whole area for one time step

$$\bar{\theta}(t) = \frac{1}{N} \sum_{n=1}^N \theta_{n,t} \quad (2.3)$$

Then mean relative difference $\bar{\delta}(n)$ and standard deviation $\sigma(\bar{\delta}(n))$ are calculated over all time steps for every location:

$$\bar{\delta}(n) = \frac{1}{T} \sum_{t=1}^T \delta_{n,t} \quad (2.4)$$

and

$$\sigma(\bar{\delta}(n)) = \sqrt{\frac{1}{T-1} \sum_{t=1}^T (\delta_{n,t} - \bar{\delta}(n))^2} \quad (2.5)$$

This analysis gives information about the stability of the spatial distribution of soil moisture from one time step to another. Higher standard deviations of MRD indicate a lower persistence of soil moisture distribution in time.

The rankings of MRDs illustrate the distribution of soil moisture in the study area. Generally, drier (wetter) areas will get a low (high) MRD and with that low (high) rank. Therefore, the similarity of ranks of modeled soil moisture and soil moisture products is a measure of the similarity of their spatial distribution.

The analysis was conducted for the SMOS product, for absolute and relative ASCAT soil moisture, and the respective averaged modeled soil moisture from WaSiM-ETH. Moreover, the SMOS product was directly compared to the ASCAT product. To avoid biased results through missing values, only data of the days on which retrievals for all pixels completely located in the study area were available were included in the analysis. Modeled soil moisture was taken for the same time steps.

2.3 Results and Discussions

2.3.1 Validation of modeled soil moisture

A comparison of the WaSiM-ETH soil moisture simulation with the in situ measurements at the TERENO test sites is shown in Fig. 2.2. As the in situ soil moisture measurements are partly influenced by freezing during winter time (January, February and December) all following analyses were restricted to the period of March to November. It has to be considered, that the in situ data was measured with different sensor types at each site.

For the test site Selhausen, the correlation coefficient was 0.80, indicating that the model captures soil moisture dynamics very well, which can also be seen in the corresponding time series (Fig. 2.2 a)). The bias of $-0.05 \text{ m}^3/\text{m}^3$ and the RMSE of $0.07 \text{ m}^3/\text{m}^3$ can be explained by the measurement depth of the in situ data, which is a mean of measurements in 4 cm and 7 cm depth, while the model simulates a depth of 5 cm, and the fact that the in situ data was obtained from a permanent bare soil, while for hydrological modeling crop-covered agricultural land was assumed as it was indicated by the Landsat ETM+ land use information of this area.

The WaSiM-ETH model was also able to capture the soil moisture dynamics of the Rollesbroich and Wüstebach test sites ($R = 0.84$ and 0.63 , respectively). However, again biases of $-0.05 \text{ m}^3/\text{m}^3$ and $0.05 \text{ m}^3/\text{m}^3$, respectively, were observed. For Rollesbroich, RMSE is $0.06 \text{ m}^3/\text{m}^3$. In situ data for the year 2010 was measured at a depth of 10 cm, while the rest was done at 5 cm depth with a wireless sensor network. In 2010 and 2011, the year the network was installed, the model seems to overestimate soil moisture, while for 2012 the measurements are captured better. For Wüstebach, the fluctuations of modeled soil moisture are higher than of the in situ data, which explains the higher RMSE of $0.09 \text{ m}^3/\text{m}^3$, although the general trend is reproduced. Though, the standard deviation of in situ soil moisture is quite high, and mostly modeled data is within this range. Additionally, it is possible that the application of the pedotransfer function of Rawls and Brakensiek (1985) to the digital soil map information leads to an underestimation of soil porosity for forest sites like Wüstebach, since the data base for the pedotransfer function derivation originated mainly from arable soils with typically lower porosities compared to forest sites.

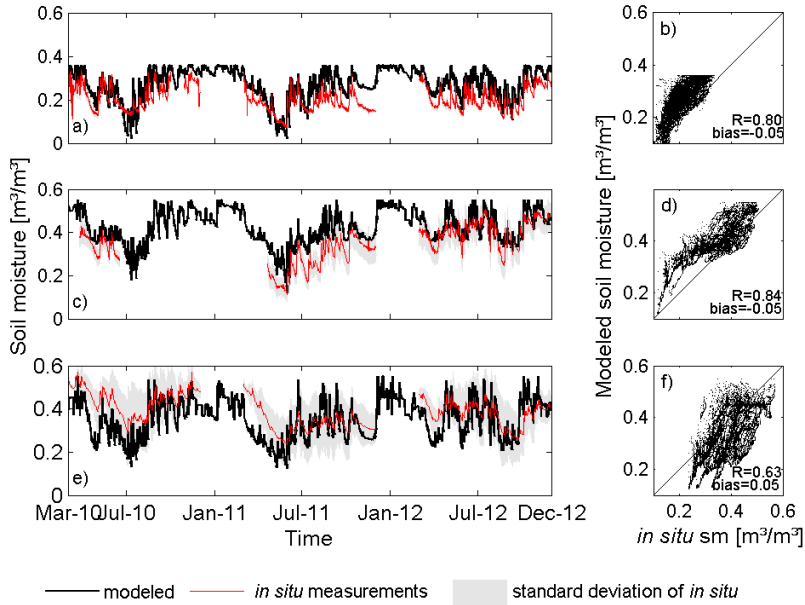


Fig. 2.2: Time series and scatterplots of in situ measurements and model results of soil moisture for a) and b) Selhausen, c) and d) Rollesbroich, e) and f) Wüstebach.

The overall correlation coefficient for all test sites is 0.72 with a corresponding bias of $-0.01 \text{ m}^3/\text{m}^3$. Therefore, it is assumed that the modeled reference soil moisture adequately represents the soil moisture pattern of the study area and can be used for the validation of the satellite soil moisture products.

2.3.2 Time series

Fig. 2.3 shows soil moisture time series from SMOS for three different pixels covering the TERENO test sites Selhausen, Rollesbroich and Wüstebach. In situ soil moisture data from these test sites were used to validate the model, since they are representative for the whole study area in terms of land use, soil, and topography. The modeled soil moisture in Fig. 2.3 is averaged over the respective SMOS pixel and the grey shading shows the standard deviation of the spatial averaging. The presented values correspond to the dates of the available observations of the remotely sensed products. The time series of ASCAT soil moisture, converted into absolute values, in Fig. 2.4 consist of the pixels including the same test sites and the respective averages modeled by WaSiM-ETH. Fig. 2.5

shows the same ASCAT pixels in the original relative values and the modeled averages scaled between 0 and 1 by using its minimum and maximum values.

In general, the SMOS soil moisture catches the trend of the model very well, but for the pixels in the southern part, it exhibits a substantial bias. ASCAT soil moisture shows no temporal constant bias, both for relative and absolute soil moisture values. In addition, ASCAT soil moisture shows high fluctuations, which the reference does not reproduce. On the one hand, this impression may partly arise, as the time series of ASCAT contain much more data points, thus enhancing the appearance of noise. On the other hand, C-band senses a thin layer of about 0.5 - 2 cm, whereas L-band observations, as well as the modeled reference, are valid for up to 5 cm. Therefore, ASCAT data is bound to vary more quickly.

The pixels of SMOS and ASCAT, which contain the Selhausen test site have a low topographic relief, the ASCAT advisory flags indicate a small topographic complexity of 2 %. According to the land use map derived from multispectral satellite data of Landsat ETM+ (Montzka *et al.*, 2008a; Montzka *et al.*, 2008b), they consist of a high fraction of agriculturally used land (49 % of the SMOS pixel, 55 % of the ASCAT pixel), but also contain some forests (19 % of the SMOS pixel, 15 % of the ASCAT pixel) and a small fraction of settlements. Both soil moisture products show the highest correlation with modeled data for this pixel, with a correlation coefficient of 0.62 for the SMOS product, 0.59 for the absolute ASCAT soil moisture and 0.56 for relative ASCAT soil moisture. SMOS shows a dry bias of $0.06 \text{ m}^3/\text{m}^3$, while ASCAT exhibits a bias of $0.04 \text{ m}^3/\text{m}^3$ in terms of absolute and 0.09 in terms of relative soil moisture.

Although the intersection of the pixels that include the Rollesbroich test site is rather small, they contain similar amounts of grassland (23 % of the SMOS pixel, 26 % of the ASCAT pixel), and forests (67 % of the SMOS pixel, 59 % of the ASCAT pixel). The ASCAT pixel comprises a water fraction of 5 %. The relief is higher than for the Selhausen pixel; the ASCAT advisory flags show a topographic complexity of 7 %. Thus, correlation coefficients are lower with a value of 0.51 for the SMOS product and 0.48 both for absolute and relative ASCAT soil moisture. The bias of SMOS is higher with $0.13 \text{ m}^3/\text{m}^3$, while ASCAT shows biases of $0.09 \text{ m}^3/\text{m}^3$ and 0.07 for absolute and relative soil moisture, respectively.

The pixels containing the Wüstebach test site consist of a high amount of forest (57 % of the SMOS pixel, 70 % of the ASCAT pixel), the grassland fraction (26 % of the SMOS pixel, 18 % of the ASCAT pixel) is also high. The ASCAT advisory flags show a topographic complexity of 5 %.

SMOS shows a lower correlation coefficient than for the other pixels with 0.37 and a higher bias with $0.19 \text{ m}^3/\text{m}^3$. The ASCAT pixel also shows the lowest correlation coefficient with 0.40 both for absolute and relative values, and a bias of $0.08 \text{ m}^3/\text{m}^3$ for absolute and -0.01 of relative soil moisture. Although the detailed land use map, derived from Landsat ETM+, sometimes shows a high amount of forests, the SMOS retrieval cases for all values included in this study are nominal. This discrepancy most probably results from the, compared to the Landsat map, coarse spatial resolution of the ECOCLIMAP land use map used in the SMOS processor. A nominal retrieval case means that the retrieved soil moisture value is valid for the land use types of low vegetation. As the modeled soil moisture gives the value for the whole pixel, a possible explanation for the higher correlation, as well as for the smaller bias of SMOS and modeled soil moisture for the pixel that covers Selhausen is, that it contains less forest than the other pixels described here.

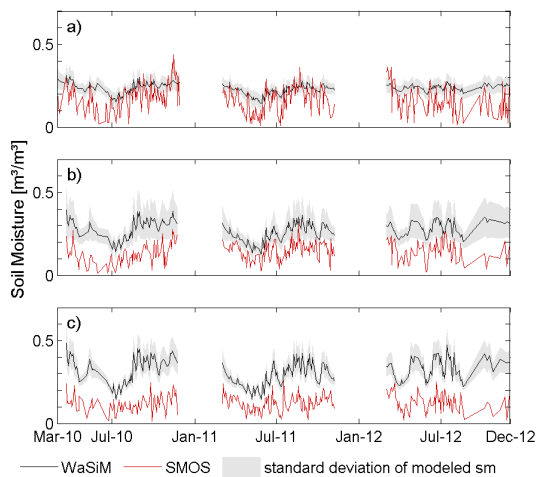


Fig. 2.3: Time series of SMOS (red) and modeled (black) soil moisture for the pixel that includes a) Selhausen, b) Rollesbroich, c) Wüstebach. Modeled soil moisture is only plotted for time steps with SMOS observations. The grey background indicates \pm one standard deviation of the spatial averaging of modeled soil moisture.

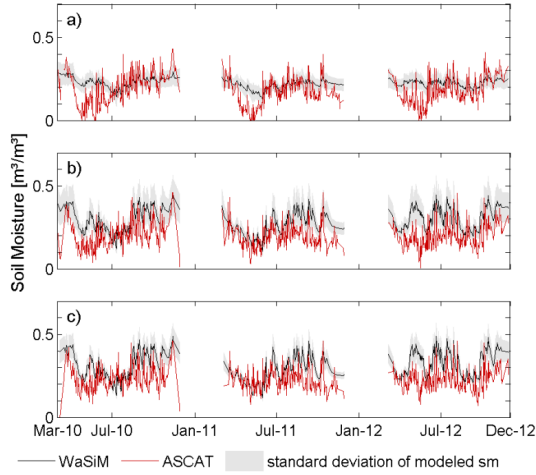


Fig. 2.4: Time series of absolute ASCAT (red) and modeled (black) soil moisture for the pixel that includes a) Selhausen, b) Rollesbroich, c) Wüstebach. Modeled soil moisture is only plotted for time steps with ASCAT observations. The grey background indicates \pm one standard deviation of the spatial averaging of modeled soil moisture.

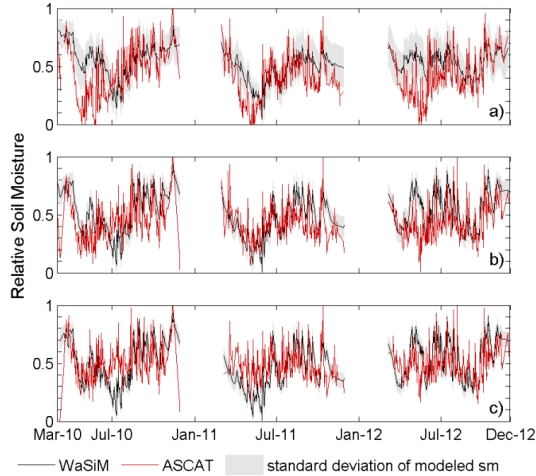


Fig. 2.5: Time series of relative ASCAT (red) and modeled (black) soil moisture for the pixel that includes a) Selhausen, b) Rollesbroich, c) Wüstebach. Modeled soil moisture is only plotted for time steps with ASCAT observations. The grey background indicates \pm one standard deviation of the spatial averaging of modeled soil moisture.

2.3.3 Correlation coefficients and biases for the whole study area

The spatial distribution of correlation coefficients in the Rur and Erft catchments (Fig. 2.6) shows similar to higher correlation coefficients for the ASCAT soil moisture product than for the SMOS product. While the SMOS product shows the highest values in the middle of the study area and very low values in the northwestern part, in the ASCAT product there is a decline of correlation from about 0.4 in the north to nearly 0.7 in the south, both for absolute and relative soil moisture values. This indicates that the quality of retrieval of ASCAT soil moisture is dependent on topography and the vegetation height, which both influences volume scattering and thus effects the soil moisture retrieval.

Looking at a map of RFI probability (Fig. 2.7 a)), derived from the values given in the SMOS soil moisture product, and averaged over the three years for every pixel, exhibits a pattern, that is very similar to that of the SMOS correlation coefficients. The correlation of RFI probability and correlation coefficient of the single pixels is shown in Fig. 2.7 b), the resulting correlation coefficient is -0.82 . That leads to the conclusion, that the SMOS product is highly influenced by RFI in the north-western part of the study area, although the RFI flags are not raised. It is possible that the thresholds used for setting these flags are not adequate for this study area.

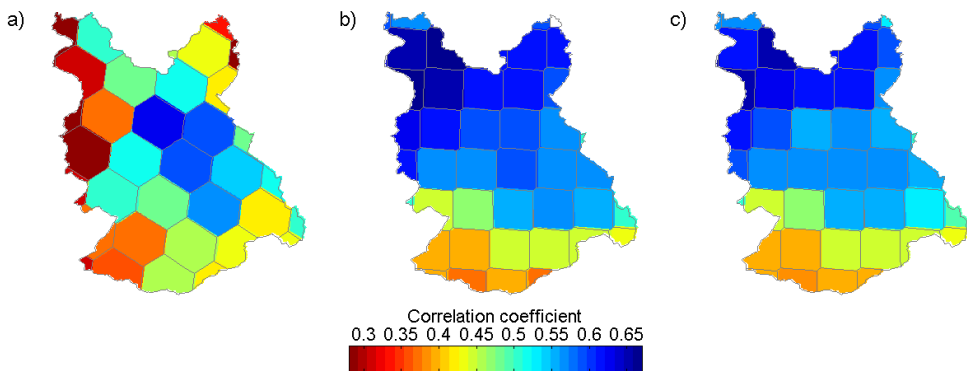


Fig. 2.6: Correlation coefficients of modeled soil moisture with a) SMOS soil moisture, b) ASCAT absolute soil moisture, and c) ASCAT relative soil moisture for each pixel.

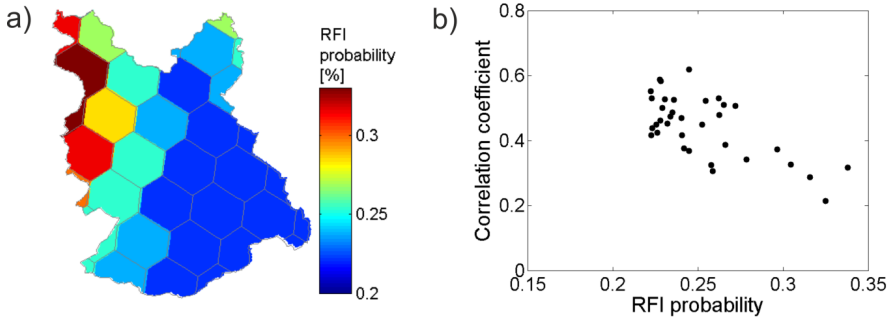


Fig. 2.7: Influence of RFI on SMOS correlation coefficients: a) Averaged probability of RFI (values taken from the SMOS product) and b) Correlation of three year averaged RFI probability with correlation coefficient between soil moisture reference and SMOS product of single pixels.

Table 2.1 shows correlations and biases for all pixels completely located in the study area. The ASCAT soil moisture product has an overall correlation coefficient of 0.50, for absolute values as well as for relative soil moisture. Correlation does not change much over the years and is always similar for absolute and relative soil moisture. The small deviations are probably caused by the averaging of the relative modeled soil moisture over the ASCAT pixels.

Table 2.1: Correlation coefficients and biases of modeled soil moisture to SMOS and absolute and relative ASCAT soil moisture for the years 2010-2012 and all pixels completely located in the study area. n is the number of observations, R is the correlation coefficient. bias is in $[m^3/m^3]$ for SMOS and ASCAT (abs) and in terms of relative soil moisture for ASCAT(rel).

	SMOS			ASCAT (abs)			ASCAT (rel)		
	n	R	bias	n	R	bias	n	R	bias
2010	1145	0.28	0.12	3735	0.49	0.07	3735	0.48	0.10
2011	1328	0.41	0.10	3745	0.56	0.09	3745	0.54	0.05
2012	945	0.14	0.13	3859	0.46	0.10	3859	0.49	0.10
overall	3438	0.28	0.12	11339	0.50	0.07	11339	0.50	0.09

The SMOS product shows an overall correlation coefficient of 0.28, mainly due to the very low correlation in 2012. The correlation increases from 2010 to 2011, probably due to the end of the commissioning phase of SMOS, which continued until June 2010, and for this time the soil moisture product may not be consistent. Additionally, many RFI sources were switched off in 2011 (Oliva *et al.*, 2012) resulting in a higher correlation. However, the correlation again decreases considerably for 2012. This is most likely due to a strong new source of RFI, that appeared in Poland in summer 2012, resulting in a reduced number of observations, and probably also the remaining retrievals are affected.

The development of correlation coefficient over the seasons (Fig. 2.8) also shows higher values for 2011 than for 2010 for the SMOS product, but it is still lower than for ASCAT, except for spring 2011. The ASCAT product shows a decrease of correlation from spring to summer and an increase from summer to autumn for 2011, following the increase and decrease of wet biomass. For 2010, the relative soil moisture values show the same behavior, but the absolute soil moisture declines from summer to autumn. This decline is caused by the distribution of absolute values in the soil moisture reference, which is not visible in the relative soil moisture, as the distribution is smoothed by the scaling.

It is remarkable, that SMOS has very low to no correlations in autumn, although the influence of the vegetation canopy is lower during this time of the year. This could indicate problems with the parameterization of litter or in the flagging of snow and frost, as to some occasions local weather stations show temperatures $< 0^{\circ}\text{C}$, while the retrievals are not frost-flagged. These frost occurrences may be local phenomena, so they may not be visible in the SMOS auxiliary data, which is taken from ECMWF, but still influence the retrieval. The low correlations of the SMOS product for 2012 can again be observed. While for summer and autumn this may be explained by the new RFI source from Poland, which was detected in July 2012, it cannot explain the low correlation in spring. As the correlation of the ASCAT product also decreases severely in spring 2012, but again rises to the values of the previous years in summer, a likely explanation are inaccuracies in the soil moisture reference for this period. In general, the ASCAT soil moisture product shows similar to slightly larger correlations than the SMOS product, which is in accordance with Albergel *et al.* (2012), who found slightly higher correlations of ASCAT soil moisture with in situ data than of SMOS Level 2 product in Europe.

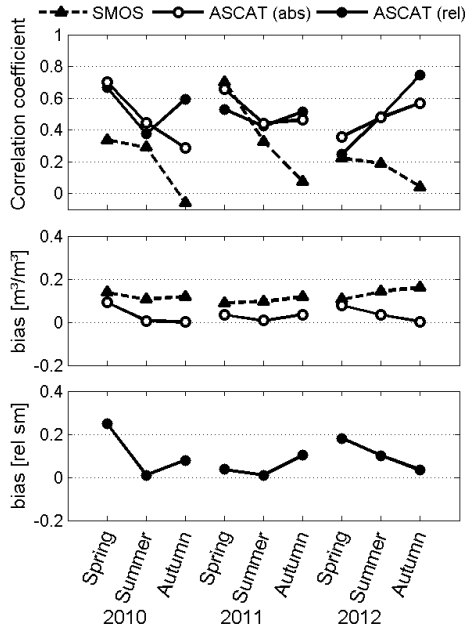


Fig. 2.8: Seasonal correlation coefficients (top) and biases of modeled soil moisture to SMOS and absolute ASCAT (middle) and relative ASCAT (bottom) soil moisture products for all pixels completely located in the study area.

The bias of SMOS in relation to modeled soil moisture shows a clear distinction between the northern and southern part of the study area (Fig. 2.9). The southern part of the study area shows values up to $0.20 m^3/m^3$ and higher, in the northern region they are constantly lower than that. With these values the bias of SMOS and modeled soil moisture is substantially higher than the one of modeled and in situ soil moisture and also exceeds the values of standard deviation of the averaging of modeled soil moisture (see Fig. 2.2). Montzka *et al.* (2013) already found the same distribution of bias in the study area for the time of May and June 2010, which was still in the commissioning phase of SMOS, but this study makes apparent that the dry bias is a temporal stable phenomenon.

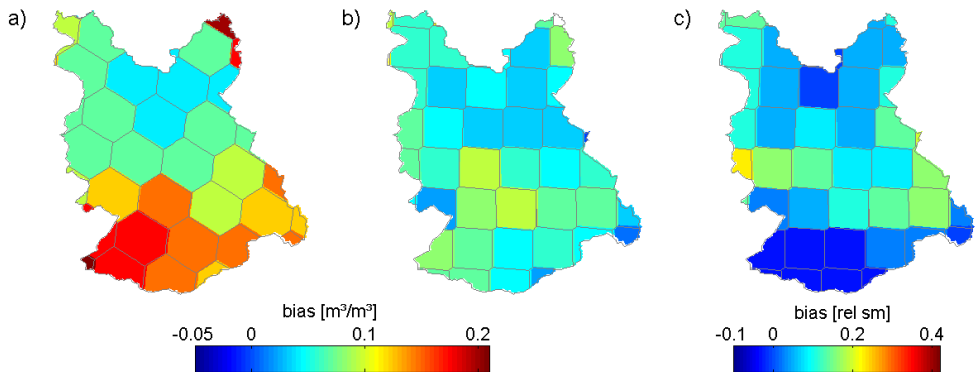


Fig. 2.9: Bias of modeled soil moisture to a) SMOS soil moisture, b) ASCAT absolute soil moisture, and c) ASCAT relative soil moisture for each pixel.

This can also be observed in Table 2.1 and in Fig. 2.8, where the development of the bias over time is displayed. The SMOS bias is nearly constant over the seasons during the three years with values varying between $0.15 \text{ m}^3/\text{m}^3$ and $0.20 \text{ m}^3/\text{m}^3$. This shows that the bias is not dependent on accuracy levels of the vegetation opacity retrieval over the year or the variations of RFI in the region, which also show temporal variations due to the RFI probability given in the SMOS product, but is more a matter of different kinds of land use or other input parameters to the retrieval model.

Similar magnitudes of bias are reported by dall'Amico *et al.* (2012), who found biases of $0.11 \text{ m}^3/\text{m}^3$ and $0.3 \text{ m}^3/\text{m}^3$ for the Upper Danube Catchment in Southern Germany. Dry biases, even though smaller, are also reported by Lacava *et al.* (2012) for Italy and Luxembourg, Sánchez *et al.* (2012) for Spain and Bircher *et al.* (2013) for Western Denmark.

The implementation of Mironov dielectric mixing model in processor version 5.51 shows an absolute improvement of $0.04 \text{ m}^3/\text{m}^3$ respectively for the years 2010 and 2011, as well as for the single seasons in these years in comparison to soil moisture retrieved in the processor version 5.00 (not shown), which used the Dobson model, but the remaining bias is still considerable.

The bias of ASCAT soil moisture to modeled soil moisture is more variable with an overall value of $0.07 \text{ m}^3/\text{m}^3$ for absolute and 0.09 in terms of relative soil moisture for the three years (Table 2.1). Consistent seasonal variations cannot be observed, the trends are similar for absolute and relative values (Fig. 2.8), and spatial patterns (Fig. 2.9) also do not get obvious, only the negative values in the mountainous part of the study area for relative soil moisture are remarkable. The bias of absolute

values is similar to lower compared to the SMOS product, but the interpretation of the biases is difficult, as they are highly influenced by the porosity data used for conversion.

The overall performance of the ASCAT soil moisture product, which is the more mature product, is slightly better, in correlation as well as in bias. The SMOS product is a rather new product and still has some inaccuracies, which have to be overcome. They result mainly from local or low energy RFI, which were not detected by the retrieval approach. The reasons for the bias have to be further analyzed.

Nevertheless, a correlation analysis like the one presented here has some limitations, for example it could be statistically influenced by different sampling sizes. Thus, correlation coefficients and biases were calculated again for SMOS and ASCAT soil moisture products with the same sampling size, randomly chosen on a weekly basis. With a number of 3399 observations an overall correlation of 0.29 for the SMOS product, 0.49 for the absolute ASCAT soil moisture and 0.53 for relative ASCAT soil moisture was found. These values are similar to the overall correlation coefficients in Table 2.1, so the sampling size does not seem to have a high influence on the results presented in this study.

Other problems of a correlation analysis are that it does not catch the temporal development of time series very well, and it also does not take into account the spatial distribution in an area.

Therefore, this study continues with the analysis of the temporal stability of the soil moisture products, which is less influenced by sampling size and not so much dependent on the absolute values of soil moisture, but rather accounts for the distribution of soil moisture.

2.3.4 Temporal stability analysis

The temporal stability analysis with MRDs and their standard deviations and rankings for SMOS and the respective averages of modeled soil moisture is shown in Fig. 2.10. SMOS has MRDs between -0.21 and 0.24 and for the WaSiM-ETH soil moisture the range of MRDs is somehow smaller with -0.12 to 0.21.

Compared to modeled soil moisture time series, standard deviations of the SMOS MRDs are quite high, their mean over all pixels is 0.20, while for modeled data it is 0.05.

Catchment scale validation of SMOS and ASCAT soil moisture products
using hydrological modeling and temporal stability analysis

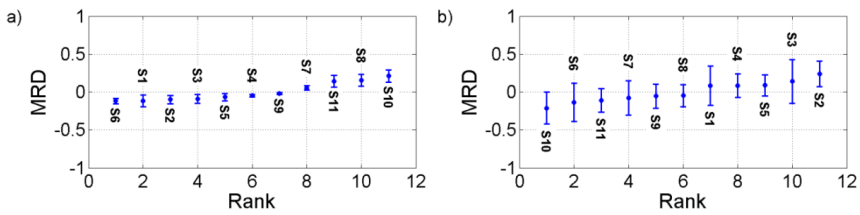


Fig. 2.10: Mean relative differences and their standard deviations for a) WaSiM-ETH soil moisture averaged over the extent of SMOS pixels and b) SMOS soil moisture product. The numbers indicate the respective grid point IDs.

The same analysis for ASCAT absolute soil moisture and the respective averaged modeled soil moisture values (Fig. 2.11) shows MRDs of -0.24 to 0.52 and -0.11 to 0.23, respectively. Standard deviations are again very low for the modeled data, with a mean over all pixels of 0.07, while they are higher for ASCAT, with a mean of 0.26.

Fig. 2.12 shows the results for relative ASCAT soil moisture, which has MRDs between -0.22 and 0.45 and relative modeled soil moisture, which has MRDs of -0.06 to 0.1. Standard deviations are 0.09 for modeled and 0.26 for ASCAT soil moisture.

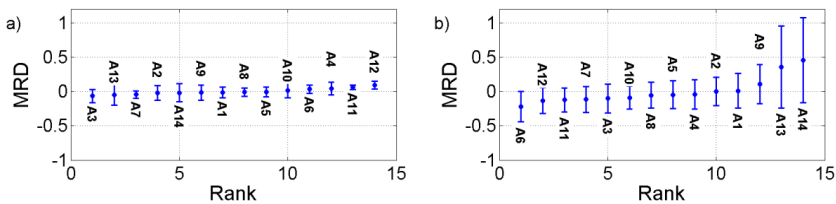


Fig. 2.11: Mean relative differences and their standard deviations for a) WaSiM-ETH soil moisture averaged over the extent of ASCAT pixels and b) absolute ASCAT soil moisture. The numbers indicate the respective grid point IDs.

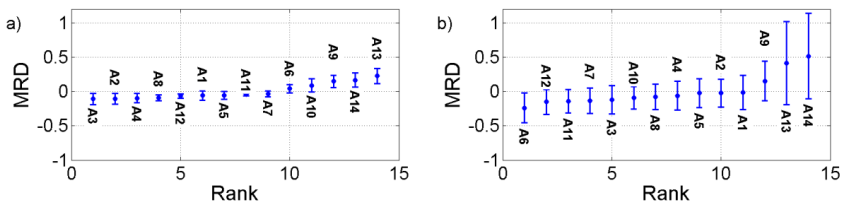


Fig. 2.12: Mean relative differences and their standard deviations for a) WaSiM-ETH relative soil moisture averaged over the extent of ASCAT pixels and b) relative ASCAT soil moisture. The numbers indicate the respective grid point IDs.

The higher ranges of MRDs and higher standard deviations of the soil moisture products compared to modeled soil moisture imply more dynamics in the spatio-temporal distribution in the remotely sensed products. An explanation for this discrepancy is that the model calculates soil moisture of the first 5 cm of the soil, while the remotely sensed soil moisture generally is only valid for a smaller depth. Higher standard deviations of the remotely sensed soil moisture products may also partly be due to external effects. However, the higher standard deviations of ASCAT may indicate a discrepancy in penetration depth, a problem that was already noticed in chapter 2.2.3.2. The standard deviations of MRDs indicate that the modeled soil moisture shows higher temporal persistency compared to ASCAT and SMOS soil moisture products.

It is assumed that in heterogeneous regions, like our study area, soil moisture shows distinct structured spatial patterns. These patterns should be reflected in both modeled and remote sensing based soil moisture. Therefore, the MRD ranks of the individual pixels in the different data sets should be alike, i.e., a relatively dryer (wetter) region should have lower (higher) ranks for all soil moisture products. To investigate this, MRDs of every pixel were ranked and the ranks of the averaged soil moisture were compared to the ranks of the respective soil moisture products in Fig. 2.13 a) - c). Additionally, the MRD ranks of SMOS and ASCAT pixels were compared, which contribute to the study area and overlap to at least 50 % (Fig. 2.13d)).

As the study area consists of only few pixels, correlation coefficients calculated from the rankings of these pixels have merely low significance. Therefore, it was only tested how many pixels are within a range of two ranks from modeled to remotely sensed soil moisture. For SMOS and relative ASCAT soil moisture in comparison with modeled soil moisture, three pixels are within this range, while for absolute ASCAT values 4 pixels are within the range. Nevertheless, the scatterplots show a rather negative relationship for SMOS and relative ASCAT soil moisture, while the absolute ASCAT soil moisture shows the best results. This relationship of the SMOS product to modeled soil moisture probably reflects the distribution of the dry bias, which is higher in the generally wetter southern part and therefore counteracts the soil moisture pattern in the study area.

Catchment scale validation of SMOS and ASCAT soil moisture products
using hydrological modeling and temporal stability analysis

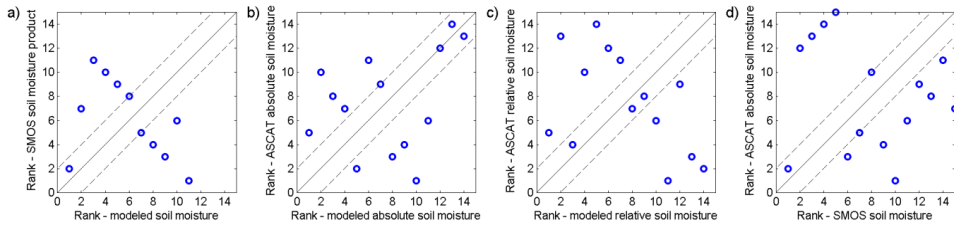


Fig. 2.13: Comparison of ranks of the MRDs of WaSiM-ETH pixel averages to ranks of MRDs of a) SMOS pixels b) absolute ASCAT pixels c) of ranks of MRDs of WaSiM-ETH pixel averages in relative soil moisture values and relative ASCAT pixels and d) of ranks of MRDs of ASCAT and SMOS pixels. The dashed line indicates pixels that are two ranks away from the 1:1 line.

Generally, the soil moisture distribution of the different products is highly influenced by the auxiliary information (e.g. soil maps) used for the soil moisture estimation. This gets obvious, for example, in the comparison of rankings of relative soil moisture, as the scaling of modeled soil moisture between highest and lowest values of the time series for every WaSiM-ETH grid cell changes the distribution of soil moisture, which is highly influenced by the lower and upper limits (wilting point and saturation point) of the respective soil types and these differences are reduced through the conversion into relative soil moisture.

The comparison of SMOS product to ASCAT product also exhibits three pixels within this range of two ranks. The differences may arise from the different characteristics of the two products, but also the different extents of the area for which they are valid may play a role here.

In general, the results of this analysis seem to confirm the prior results. Both remote sensing products perform similar in the Rur and Erft catchments, with higher fluctuations and a more similar distribution of values of ASCAT compared to modeled soil moisture. However, the latter is only valid, when the absolute values of the model are considered in comparison with the ASCAT product, the relative values compared to rescaled modeled soil moisture, as well as SMOS soil moisture, show less correspondence in their spatial patterns.

When interpreting the results of this study, it has to be taken into account, that the spatial distribution of soil moisture in the model and the different products is influenced by different factors. As this study analyses only a relative small area compared to the pixel size of the SMOS and ASCAT soil moisture products, there were not enough pixels to calculate meaningful statistics, for example correlation coefficients of ranks. Further studies are needed to verify this analysis in larger areas and for different environments (e.g. semi-arid areas).

Nevertheless, it could be shown that temporal stability analysis can be used as an additional tool for the validation of soil moisture products. The advantage of this method is that it accounts both for the temporal and for the spatial behavior of the products and does not only investigate the performance of single pixels. Furthermore, a temporal and spatial stable bias in a soil moisture product would not influence the results, and with adequate bias mitigation strategies, the information content of the product may still be valuable for a further utilization of the data.

2.4 Conclusions

The SMOS Level 2 soil moisture product and the ASCAT soil moisture product for the Rur and Erft catchments were compared to a soil moisture reference generated by the hydrological model WaSiM-ETH for the years 2010 to 2012. Additionally, as a new validation method, a temporal stability analysis of the two soil moisture products was performed to investigate the quality of the soil moisture products.

The SMOS soil moisture product showed similar trends compared to modeled soil moisture. However, the correlation was highly dependent on RFI. Regions with high RFI probability show lower correlations and overall correlations are higher in times with less RFI. Especially in the southern part of the study area, a temporally stable dry bias was observed, which was probably influenced by land use or other input parameters of the retrieval model.

ASCAT soil moisture showed generally higher temporal variability, but still good correlation with reference data both for the whole study area and for single pixels. The correlation was better for the relatively flat northern part of the study area compared to the southern part within the Eifel Mountains. The bias did not exhibit specific temporal or spatial patterns. The relative soil moisture values and the ones converted into absolute soil moisture showed similar results.

Further analysis of the products in the study area may include a cdf-matching to investigate them with a reduced systematic bias.

The temporal stability analysis showed a similar spatial distribution for modeled soil moisture and the absolute ASCAT values. However, SMOS soil moisture and relative ASCAT soil moisture did not exhibit the same spatial patterns as the reference. The temporal stability analysis is recommended as a useful tool for a more detailed validation of soil moisture products.

3 Spatio-temporal variability of global soil moisture products²

3.1 Introduction

Impacting surface and subsurface runoff as well as evaporation and transpiration, soil moisture is an essential variable in energy and water balance (Seneviratne *et al.*, 2010). Thus, information about soil moisture and its spatial and temporal dynamics is crucial for improvements in climate and hydrological modeling and in numerical weather prediction. These applications require representative soil moisture time series for large regions or even global coverage.

Remote sensing techniques showed to be able to provide soil moisture with high coverage and in reasonable temporal and spatial resolution (Kerr, 2006). Several sensors differing in sensing technique (active/passive), frequency, and retrieval methods are currently used for monitoring soil moisture, resulting in soil moisture products with different characteristics and spatial resolution. Sensors used for retrieving soil moisture at present are the ASCAT onboard the meteorological satellite MetOp-A (Bartalis *et al.*, 2007), the AMSR-2 on the Global Change Observation Mission – Water (Su *et al.*, 2013), the SMOS satellite (Kerr *et al.*, 2010), and the combined active and passive instruments Aquarius (Luo *et al.*, 2013) and SMAP (Entekhabi *et al.*, 2010).

Another way to provide soil moisture with high spatial coverage is modeling. Products from different models are available, for example from the Global Land Data Assimilation System (Rodell *et al.*, 2004) or from the Integrated Forecast Model of the ECMWF. They provide operational analyses for which the model is constantly improved, but also reanalyses, that use only one model and thus give consistent data (Albergl *et al.*, 2012), for example the ERA Interim (Dee *et al.*, 2011).

Modeled, but also remotely sensed products show a large range of spatial resolutions. While for models the spatial resolution is chosen mainly on consideration about computational and storage costs, remotely sensed products are dependent on the technical possibilities of antennas. Currently, active microwave systems provide higher spatial resolutions than passive microwave systems operating at lower frequencies, such as L-band (Wang and Qu, 2009). Nevertheless, theory says that L-band radiometry has several advantages for the estimation of soil moisture compared to higher frequencies (Kerr *et al.*, 2012; Vitucci *et al.*, 2013), especially the higher vegetation penetration depth

² Adapted from: Rötzer, K., Montzka, C., Vereecken, H. (2015): Spatio-temporal variability of global soil moisture products. *J. Hydrol.* 522, 187–202.

(Njoku and Entekhabi, 1996) and the higher soil penetration depth, compared to higher frequency systems which is between 0.5 and 2 cm for C-band systems like ASCAT and AMSR-2 and about 3-5 cm for L-band systems (Escorihuela *et al.*, 2010), like SMOS, Aquarius, and SMAP.

These differences, as well as diverse modeling and retrieval approaches are the main sources of deviations between different modeled and remotely sensed soil moisture products. The validation of these products is challenging due to their rather coarse resolution compared to in situ data and the lack of extensive in situ measurements. Additionally, the products and in situ data have different scaling characteristics. According to Western and Blöschl (1999) “scale” can be defined as a triplet consisting of spacing, extent and support. Spacing refers to the distance between samplings or neighboring pixels, support to the integrated volume or area of one measurement, and extent to the covered area (Vereecken *et al.*, 2014). However, in situ data differs from the global products in these three components. Therefore, to estimate the spatial and temporal validity of validation studies, it is important to know the spatio-temporal characteristics of the soil moisture products.

In this study these characteristics are evaluated to exhibit statistical and structural differences and similarities between the products, and also between different regions. The influence of sensor and retrieval methods on the statistical patterns is analyzed. This knowledge is also important in case that several products should be used in one application. The ESA Climate Change Initiative soil moisture product (Dorigo *et al.*, 2012; Liu *et al.*, 2011; Liu *et al.*, 2012), for example, combines products from different sensors. But also if only one product is used in a designated region, it is important to be aware of these characteristics. Applications for soil moisture products are for example usage in runoff forecasting (Brocca *et al.*, 2012), vegetation monitoring (Gouveia *et al.*, 2009), and natural risk assessment, especially drought (Bolten *et al.*, 2010) and flood monitoring (Wanders *et al.*, 2014). Furthermore, the knowledge of systematic differences between soil moisture products is essential for usage in hydrological data assimilation (Yilmaz and Crow, 2013). As global soil moisture products may not always meet the spatial requirements of the respective applications due to their rather coarse resolution, up- and downscaling of soil moisture is of importance. For this task, information about spatial variability of soil moisture is crucial (Manfreda *et al.*, 2007).

On larger extent scales, precipitation patterns and climatic influences are the dominant factors on spatial soil moisture distribution (Famiglietti *et al.*, 2008). Nevertheless, its impact is controlled by evaporation, soil type, irradiation, vegetation and topography (Dorigo *et al.*, 2012).

The influence of these factors should be reflected in the soil moisture products. If their spatial and temporal patterns are different, these differences will be introduced by the respective estimation method.

To examine spatial and temporal patterns in the different soil moisture products, we apply several frequently used methods on three different soil moisture products in this study: First, a rank stability analysis is performed. This is traditionally used for the minimization of sampling locations for soil moisture measurements on field scale through the determination of locations that are representative for the whole area (Vachaud *et al.*, 1985; Cosh *et al.*, 2004; Brocca *et al.*, 2009b; Zhao *et al.*, 2013). In Rötzer *et al.* (2014) it was introduced as a method for the validation of soil moisture products through the correlation of their ranks. Vanderlinden *et al.* (2012) give an overview on methodologies and applications of temporal stability.

Then the relationship of spatial mean and spatial variance of soil moisture was analyzed. This relationship was often investigated on small extent scale and it was found to be quite variable: Bell *et al.* (1980) and Famiglietti *et al.* (1998) found decreasing variance with decreasing mean, while for example Famiglietti *et al.* (1999), Hupet and Vanclooster (2002) and Brocca *et al.* (2007) found increasing variance with decreasing mean. Others, like Famiglietti *et al.* (2008) and Rosenbaum *et al.* (2012) observed a convex upward relationship. The different shapes of relationships are caused by a variety of factors like topography, radiation, soil characteristics, vegetation and land use, with different strength of influence in the respective study areas. Li and Rodell (2013) analyzed the same relationship on the continental extent scale for in situ measurements, modeled and remotely sensed soil moisture from AMSR-E and found a convex relationship for in situ measurements over different climate zones. For modeled and remotely sensed soil moisture this relationship was less pronounced. The third analysis is the examination of influencing factors on the spatial variance of soil moisture through its decomposition into temporal variant and temporal invariant parts (Mittelbach and Seneviratne, 2012). The analysis considers not only absolute values, but the temporal mean of a site and its anomalies and provides information on whether differences between sites are due to temporal mean or anomaly (Brocca *et al.*, 2014). The comparison of the single contributors to the different products can give added value for improved downscaling algorithms (e.g. Das *et al.*, 2014; Merlin *et al.*, 2006; Merlin *et al.*, 2013) and for matching different soil moisture products to generate long-term time series (Dorigo *et al.*, 2012; Liu *et al.*, 2011; Liu *et al.*, 2012). For the latter, it is important that all products have a similar temporal mean on one study site. Through these analyses, the statistical and structural relative differences of the soil moisture products will be assessed.

The soil moisture products were also analyzed on their behavior on different scales following the definition of Western and Blöschl (1999). Changes of one of the three components spacing, support, and extent impact the spatial variance of soil moisture. Rodriguez-Iturbe *et al.* (1995) found a power law decay of spatial variance of soil moisture with increasing support for areas up to 1 km², while Ryu

and Famiglietti (2006) did not find this behavior for larger support areas of 1 to 140 km². The increase of extent was found to increase spatial variance according to a power law function for scales of 16 m to 1.6 km (Famiglietti *et al.*, 2008). Scaling functions like this are important information for the up- and downscaling of soil moisture. It will be examined if similar relationships can be found on varying support and extent scales of modeled and remotely sensed soil moisture and if the scaling behavior of the different products is similar.

In the following, the characteristics of three soil moisture products, the SMOS Level 2 product, the ASCAT relative surface soil moisture product, and the soil moisture of the ERA Interim reanalysis from ECMWF will be examined for the years 2010-2012. After the description of the used soil moisture products and the methods in the following section, first the global patterns of the products will be analyzed and then their statistics for specific regions will be compared. In the last chapter the behavior of the soil moisture products on different scales will be examined.

3.2 Material and Methods

3.2.1 The Soil Moisture Products

3.2.1.1 SMOS Soil Moisture Product

Launched in 2009, SMOS is a sun-synchronous orbiting satellite at an altitude of 755 km. On three day basis, the SMOS radiometer records two-dimensional brightness temperatures in the L-Band at 1.4 GHz. Its measuring performance is 0.8 to 3.0 K for the radiometric sensitivity with a spatial resolution of 30 to 50 km (Kerr *et al.*, 2001).

Volumetric soil water content is retrieved in the SMOS Level 2 Processor for Soil Moisture, which is working with a physically based algorithm (Kerr *et al.*, 2012) from the Level 1C brightness temperature product. Resampled on the ISEA-4H9 grid, it is distributed with approximately 15 km distance between grid points.

The SMOS soil moisture product (hereafter referred to as SMOS) used in this study was retrieved with the Level 2 Processor version 5.51. Soil moisture data was filtered through the data quality index SM_DQX, which is the standard deviation of the retrieved soil moisture and reflects radiometric uncertainty, and the Chi² parameter, which is a measure for the goodness of retrieval fit. Values with SM_DQX > 0.1 m³/m³ and Chi² < 0.5 and Chi² > 2.5 were excluded from all analyses.

3.2.1.2 ASCAT Soil Moisture Product

The ASCAT is a real aperture radar onboard the MetOp-A satellite, a meteorological mission with a sun-synchronous orbit at an altitude of 837 km. Operating in C-band at 5.255 GHz, within every measurement a triplet of backscattering coefficients at three incidence angles is produced. Its global coverage is one to two days with a spatial resolution of 25 to 50 km (Bartalis *et al.*, 2007; Naeimi *et al.*, 2009).

The operational ASCAT soil moisture product (hereafter referred to as ASCAT) is a relative measure with values between 0 and 100%, stating the degree of saturation of the soil. The retrieval of relative soil moisture from the ASCAT backscattering coefficients is based on the change detection method of Wagner *et al.* (1999a).

This study uses the operational product produced by Eumetsat and retrieved in the Soil Moisture Product Processing Facility (SOMO PPF) version 2.0 until August 2011, since then version 3.1 was used for retrieval (Eumetsat, 2011). The product is filtered with the soil moisture error (*sm_error*), which is derived by error propagation of the backscatter noise, the frozen soil probability and the snow cover probability, both based on long-term climate information. Values with *sm_error* $\geq 20\%$, frozen soil probability $\geq 50\%$ and snow cover probability $\geq 50\%$ were excluded.

For a quantitative comparison with the other products, the relative soil moisture values are converted to absolute soil moisture by multiplying them with soil porosity values. These were calculated at the Vienna University of Technology with the equations of Saxton and Rawls (2006) from data from the Harmonized World Soil Database.

3.2.1.3 ERA Interim Soil Moisture

ERA Interim is a reanalysis of the global atmosphere covering the period from 1979 and continuing in real time (Dee *et al.*, 2011). Basing on the Integrated Forecasting System, the numerical weather prediction model of the ECMWF, the reanalysis is produced with a single version of forecast model, the Integrated Forecast Model release Cy31r2. The data assimilation system, the optimal interpolation scheme, is also fixed. Using the Tiled ECMWF Scheme of Surface Exchanges over Land for land surface scheme, a large range of gridded data products is provided, including volumetric soil water content discretized in 4 layers (Berrisford *et al.*, 2009). In this land surface scheme, the surface water balance is computed as the difference of precipitation and evaporation, surface and subsurface runoff (Albergel *et al.*, 2012).

To account for the sensing depths of the remotely sensed products introduced in the previous sections, this study uses the soil moisture of the surface layer of 0 - 0.07m. The ERA Interim soil moisture product (hereafter referred to as ERA) is available on grids with different resolutions. For this study, the product with a resolution of 0.75° was used.

3.2.2 Study areas

Assuming that precipitation and climate are the dominant factors on spatial soil moisture distribution at global extent scale (Famiglietti *et al.*, 2008), the analyses of spatio-temporal soil moisture behavior are based on the Köppen-Geiger climate zones (Fig. 3.1), determined by Peel *et al.* (2007). The classification is based on temperature and precipitation thresholds: There are five main classes, four of which are determined by temperature thresholds. These are A (Tropical), C (Temperate), D (cold) and E (Polar). The fifth main class B (Arid) is defined by a precipitation threshold. The subclasses (second order) are specified by precipitation only. While A and B climate subclasses provide information about the absolute precipitation, the C and D climates also describe the temporal distribution of precipitation, i.e. mainly summer or winter precipitation or no dry season. The third order classes, which are again based on temperature thresholds, were not considered for the selection of study regions, as then the choice of homogenous regions in a sufficient size is not possible any more for many climate classes.

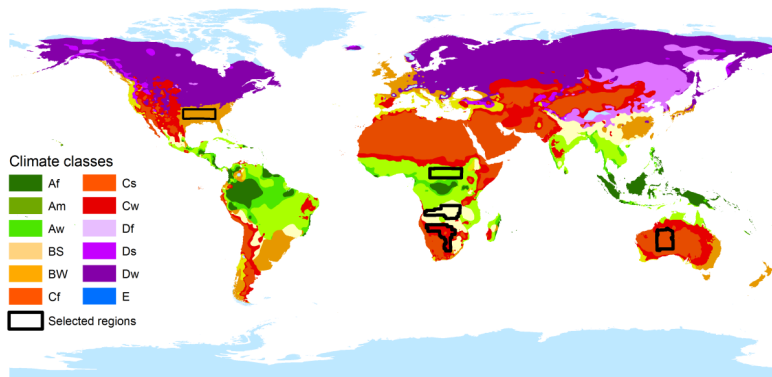


Fig. 3.1: Köppen-Geiger climate classes and for analysis selected regions. Adapted from Peel *et al.* (2007).

The regions selected for more particular studies are visible in Fig. 3.1 and are distributed in all classes, except classes D and E, which have a high amount of frozen soil during the year and thus long time periods of erroneous or missing data. In the Af (Tropical rainforest) climate no study area was designated either, due to retrieval problems from remotely sensed data under dense vegetation (Leroux *et al.*, 2013). For the locations of the study areas America, Africa and Australia were chosen, as these continents are known to be less affected by RFI than Europe and Asia (Daganzo-Eusebio *et al.*, 2013). This is important for the quality of passive microwave remote sensing products, such as those obtained by SMOS.

Every study region is a coherent area of $\sim 650,000$ km² within one homogenous climate class of the second order containing 120 grid points. Due to the shapes of the classes, some study regions have an irregular form. No study area was designated in the Am and Cs climates, as the sizes of these climate classes did not meet the requirements. This resulted in the selection of five regions, one in America, one in Australia, and three in Africa. An overview over the regions is given in Tab. 3.1, their locations can be observed in Fig. 3.1. The climate charts in Fig. 3.2 give a more detailed impression on the general temporal distribution of temperature and precipitation. The data for these charts is from the German Weather Service (DWD) and accounts for the reference period of 1961-1990. The respective stations are located within the study areas.

The first African study area is located in the Aw (Tropical Savannah) climate. The study area is situated in the northern hemisphere and covers large parts of the countries of the Central African Republic and South Sudan. Small parts from the Democratic Republic of the Congo and Chad are also included. Elevation is varying from 339 m to 1421m a.s.l. The topographic complexity, delivered with the ASCAT product and showing the standard deviation of elevation in percent calculated from GTOPO30, is between 0 % and 10 %. The respective climate chart (Fig. 3.2 a)) shows high amounts of precipitation from March to November and lower precipitation during the winter months.

The second study region in Africa is in the BS (Arid Steppe) climate with a distinct precipitation season from November to March (Fig. 3.2 b)), and covers a large part of the country of Botswana and smaller parts of Namibia and South Africa, i.e. it is located on the southern hemisphere. Elevation varies between 615 m and 1976 m a.s.l., and topographic complexity is between 0 % and 10 %, similar to the first location.

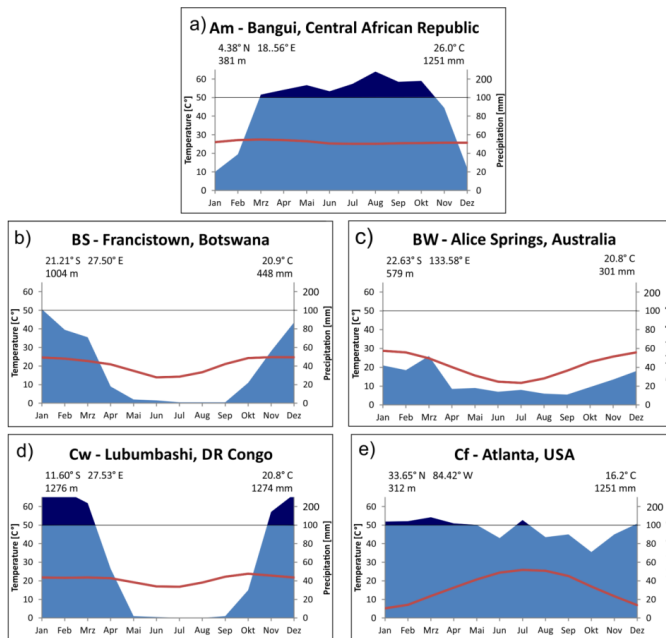


Fig. 3.2: Climate charts for stations in the selected study regions, referring to the reference period 1961-1990. Data provided by the German Weather Service (Deutscher Wetterdienst, 2007), Offenbach/Main.

The third study area in Africa is situated on the southern hemisphere in the Cw (Temperate with dry winter) class in the border region of Angola, the Democratic Republic of the Congo, and Zambia. According to the climate chart (Fig. 3.2 d)), the dry season lasts from May to September. Topographic complexity is higher here with values between 0 % and 20 %, while elevation varies between 564 m and 2498 m a.s.l.

A study area in the BW (Arid desert) class with low precipitation values throughout the year (Fig. 3.2 c)) is located in Australia. Please note that the climate chart of the BW region is not located directly in the study area, but within a distance of about 300 km. However, it is still representative for its climate class. Elevation of this study region is between 184 and 1203 m a.s.l., consequently topographic complexity flag shows low values between 0 % and 8 %. The Cf (Temperate without dry season) study region (Fig. 3.2 d)) is situated in North America in the United States of America. Elevation varies from 12 m to 1625 m a.s.l. and therefore topographic complexity is high with values between 0 % and 20 %.

Table 3.1: Description of study areas. Abbreviations for criteria: T_{cold} , T_{hot} : Temperature of coldest and hottest month, respectively. MAP: mean annual precipitation. P_{dry} : Precipitation of driest month. P_{wdry} and P_{swet} : Precipitation of driest winter month and wettest summer month (October–March or April–September, depending on temperature), respectively. $P_{threshold}$: Variable precipitation threshold. For further information see Peel et al. (2007).

Region	Definition criteria for climate class 1 st order	Definition criteria for climate class 2 nd order	Min/Max lat	Min/Max lon
Aw Africa	$T_{cold} \geq 18$	Not Af & $P_{dry} < 100 \cdot MAP / 25$	4.3°N / 8.7°N	17.0°E / 31.9°E
BS Africa	$MAP < 10 \cdot P_{threshold}$	$MAP \geq 5 \cdot P_{threshold}$	17.6°S / 29.8°S	15.3°E / 28.9°E
BW Australia	$MAP < 10 \cdot P_{threshold}$	$MAP < 5 \cdot P_{threshold}$	19.2°S / 29.5°S	123.4°E / 139.9°E
Cw Africa	$T_{hot} < 10$ & $0 < T_{cold} < 18$	$P_{wdry} < P_{swet} / 10$	8.7°S / 14.7°S	14.6°E / 31.1°E
Cf America	$T_{hot} < 10$ & $0 < T_{cold} < 18$	Not (Cs) or (Cw)	31.8°N / 36.2°N	83.5°W / 98.6°W

For the definition criteria of the different climate classes see Tab. 3.1 and Peel et al. (2007).

For the analysis of scaling differences, three larger regions with an area of 9,000,000 km² each were designated on three continents: America, Africa and Asia. An Asian study area was included in spite of the aforementioned RFI exposure, because of the difficulty to find an area big enough on the RFI free continents like South America or Australia. The selection of these regions was based on the size of the respective areas. Their locations and fractions of climate zones are visible in Fig. 3.3.

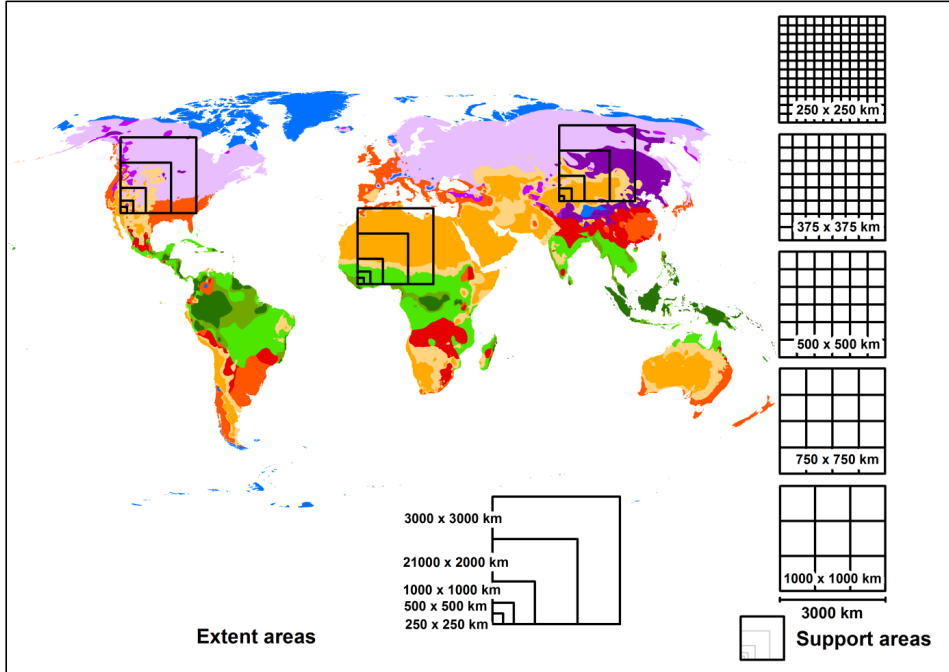


Fig. 3.3: Location and sizes of areas for support and extent scale studies with climate regions. For the legend of climate regions please see Fig. 3.1.

3.2.3 Methods

To avoid the influence of different support scales on the results, SMOS, as well as ASCAT are upscaled to the ERA Interim grid by allocating the closest ERA grid point for every SMOS and ASCAT grid point and taking the average over all points assigned to one ERA grid point.

3.2.3.1 Temporal Stability Analysis

The temporal stability of the three soil moisture products was examined following the method of Vachaud *et al.* (1985). Using the spatial mean soil moisture $\bar{\theta}(t)$ over the number of Pixels n for one time step t

$$\bar{\theta}(t) = \frac{1}{N} \sum_{n=1}^N \theta_{n,t} \quad (3.1)$$

the relative difference $\delta_{n,t}$ is calculated from the respective soil moisture value $\theta_{n,t}$ for every pixel n and time step t

$$\delta_{n,t} = \frac{\theta_{n,t} - \bar{\theta}(t)}{\bar{\theta}(t)} \quad (3.2)$$

Then mean relative difference $\bar{\delta}(n)$ is determined over all time steps t for every location:

$$\bar{\delta}(n) = \frac{1}{T} \sum_{t=1}^T \delta_{n,t} \quad (3.3)$$

In general, while dry areas get a low MRD, wet areas will exhibit high MRDs. For comparison of the products, the MRDs are ranked from lowest to highest for every soil moisture product and the correlation of these ranks is analyzed for different climate classes. The power of correlation shows the similarity of the spatial distribution of the respective soil moisture products.

3.2.3.2 Spatial variability and its time-variant and time-invariant contributors

The relationship between spatial mean and spatial variance of soil moisture is a commonly used tool for the investigation of spatial variability (Brocca *et al.*, 2007; Famiglietti *et al.*, 2008). In this study, this relationship is examined separately for the different soil moisture products and for the five study areas in different climate classes. The spatial mean soil moisture $\bar{\theta}(t)$ was determined following equation (3.1). The corresponding spatial variance $\sigma^2(t)$ is

$$\sigma^2(t) = \frac{1}{N} \sum_{n=1}^N (\theta_{n,t} - \bar{\theta}(t))^2 \quad (3.4)$$

The investigation of factors influencing the spatial distribution of soil moisture follows the approach of Mittelbach and Seneviratne (2012) and decomposes $\sigma^2(t)$ into its time-varying and time-invariant contributors, thereby determining the quantities of contributions from factors linked to soil moisture dynamics and temporally stable features. To achieve that, every observation $\theta_{n,t}$ is split into its temporal mean $\bar{\theta}(n)$ that is given by

$$\bar{\theta}(n) = \frac{1}{T} \sum_{t=1}^T \theta_{n,t} \quad (3.5)$$

and its temporal anomaly $A_{n,t}$, so $\theta_{n,t}$ can be described as

$$\theta_{n,t} = \bar{\theta}(n) + A_{n,t} \quad (3.6)$$

Accordingly, $\bar{\theta}(t)$ can be expressed as

$$\bar{\theta}(t) = \frac{1}{N} \sum_{n=1}^N \bar{\theta}(n) + \frac{1}{N} \sum_{n=1}^N A_{n,t} = \bar{\theta} + \bar{A}(t) \quad (3.7)$$

Using equations (3.6) and (3.7) for the decomposition of $\sigma^2(t)$ results in

$$\sigma^2(t) = \frac{1}{N} \sum_{n=1}^N [(\bar{\theta}(n) + A_{n,t}) - (\bar{\theta} + \bar{A}(t))]^2 \quad (3.8)$$

This can be rebuilt to

$$\sigma^2(t) = \frac{1}{N} \sum_{n=1}^N [(\bar{\theta}(n) - \bar{\theta})^2 + 2(\bar{\theta}(n) - \bar{\theta})(A_{n,t} - \bar{A}(t)) + (A_{n,t} - \bar{A}(t))^2] \quad (3.9)$$

leading to the following equation

$$\sigma^2(t) = \sigma^2(\bar{\theta}(n)) + 2 \text{cov}(\bar{\theta}(n) A_{n,t}) + \sigma^2(A_{n,t}) \quad (3.10)$$

where the variance of the temporal mean $\sigma^2(\bar{\theta}(n))$ is the temporal invariant part of the equation, and the sum of the covariance between temporal mean and anomalies $\text{cov}(\bar{\theta}(n) A_{n,t})$ and the variance of anomalies $\sigma^2(A_{n,t})$ is the temporal variant part. This allows us to consider the

percentage contributions of temporal variant and invariant components to $\sigma^2(t)$ and their temporal evolution in the five study areas in different climate classes.

3.2.3.3 Spatial scales of soil moisture

For the soil moisture products used in this study, spacing refers to the distance between the grid points (i.e. 0.75°). Spacing corresponds with support, as the products are assumed to be representative for the area around the grid point. Nevertheless it has to be kept in mind, that the remotely sensed products already were resampled and averaged on to the ERA Interim grid.

For analyzing the impact of support size on the $\sigma^2(t)$ on different scales the values of grid points were aggregated over areas with increasing sizes of 250 x 250 km to 1000 x 1000 km by taking their arithmetic mean. Using an extent area of 3000 x 3000 km, the variance over the newly created pixels was calculated for each aggregation level. The support sizes of the pixels and the location of the three study areas can be found in Fig. 3.3.

For investigating the influence of extent scale, $\sigma^2(t)$ was calculated on five different scales from grid points in an area of 250 x 250 km to 3000 x 3000 km. This is done on three test sites, whereby the 3000 km areas correspond to the areas of the support size analysis. The extents of the areas and their locations are shown in Fig. 3.3. The areas include 9 to 12 grid points on the smallest scale, while on the largest scale they consist of 1547 to 1952 grid points.

Famiglietti *et al.* (2008) found that the spatial standard deviation of soil moisture changes as a power of the extent scale. They express the spatial variance as

$$\sigma^2(t) = c * a^\mu \quad (3.11)$$

where a is the area of the respective extent scale, μ is a fractal power and c is a parameter. Assuming this, the relationship of logarithmic area vs. logarithmic variance will be linear, and then the fractal power k corresponds to the slope of a line fitted to that relationship, while the parameter c is equal to 10 to the power of intercept of this line.

Slope and intercept of this relationship were calculated, both for the changes in support and extent scale (μ_s / c_s and μ_e / c_e , respectively) for all products. As a measure, how close the relationship of log area vs. log variance is to a perfect linear relationship, the coefficient of determination (R^2) was calculated. The results presented show a mean of $\sigma^2(t)$ over all time steps. Additionally, the change of μ_e with time and the relationship of extent area vs. $\bar{\theta}(t)$ are investigated.

3.3 Results and Discussion

3.3.1 Global

3.3.1.1 Temporal means

Fig. 3.4 shows the temporal mean of soil moisture for the three products over the whole study period. It gives a general overview on their global soil moisture distribution. At first glance, the patterns look similar for all of them: They show their lowest values in the big desert regions and higher values in temperate and cold climates.

Though, the range of values is quite different: SMOS (Fig. 3.4 a)) shows relatively low values compared to the other products, which is reflected in an overall mean of soil moisture of $0.16 \text{ m}^3/\text{m}^3$. The overall mean of ASCAT is considerably higher with $0.21 \text{ m}^3/\text{m}^3$, and the range of values is larger. However, the range is obviously influenced by the porosity data used for the conversion of relative into absolute soil moisture values. As demonstrated in previous studies (Balsamo *et al.*, 2009; Dorigo *et al.*, 2010), ERA shows a very narrow range of values mainly between 0.2 and $0.4 \text{ m}^3/\text{m}^3$, and very few small scale variations. High soil moisture can only be observed in the coastal part of Greenland, very low values can be found in northern Africa. The overall soil moisture mean is $0.26 \text{ m}^3/\text{m}^3$.

Discrepancies in the soil moisture patterns can be found in areas with problems affecting soil moisture modeling or retrieval. Major drawbacks in soil moisture retrieval from microwave remote sensing are for example dense vegetation and frozen or snow covered soil (de Jeu *et al.*, 2008). The latter gets obvious when looking at the cold and polar climates, where large differences can be observed among the different products despite filtering: While SMOS shows low and ERA moderate soil moisture values, ASCAT values are quite high. The problem with high vegetation can be observed in the Tropical rainforest region for SMOS, which shows very low soil moisture there, while both ASCAT and ERA show moderate values. These sensing and retrieval problems occur, as in the brightness temperatures, which are recorded by the SMOS satellite, but also the backscattering coefficients recorded by ASCAT contain a lot of information about vegetation and only very few about the soil. In tropical rainforest regions there is nearly no soil signal any more. This potentially leads to difficulties in the parameterization of retrieval algorithms.

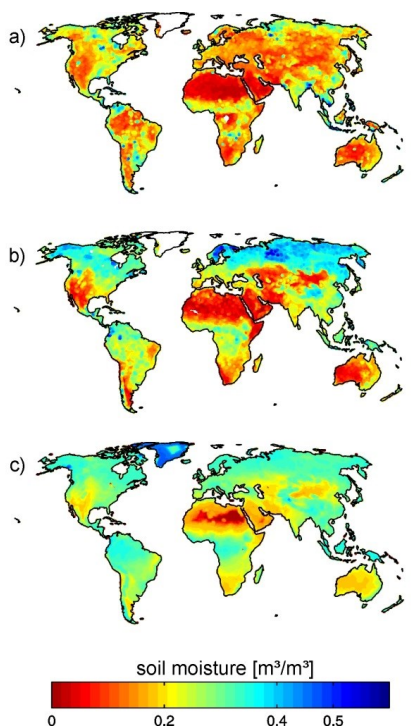


Fig. 3.4: Temporal means over the whole study period (2010-2012) of a) SMOS, b) ASCAT, c) ERA Interim.

3.3.1.2 Temporal stability

From the prior section it is obvious, that the correspondence of soil moisture patterns among the three products is quite variable between different regions. To get quantified information about the similarity of soil moisture distribution, the correlation of MRD rankings was analyzed globally for different climate classes (Fig. 3.5).

Over the entire world, the products show reasonable correlation coefficients of 0.34 (ERA / SMOS), 0.44 (SMOS / ASCAT), and 0.79 (ERA / ASCAT), which supports our finding of the previous section, that the overall soil moisture patterns are similar. However, for the different climate zones, there is large variation in correlation coefficients, and the correlation coefficients can be very different for the different products within one climate zone.

High correlations of ranks for all products occur in regions with generally low vegetation, especially in the arid regions (BS / BW). In areas, where no high vegetation infers the retrieval of soil moisture, all products show similar patterns of soil moisture.

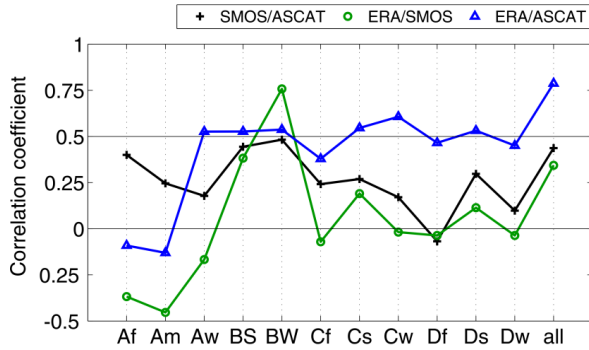


Fig. 3.5: Global correlation of ranks of MRDs of the three soil moisture products for different climate zones. The lines are just for increasing readability and do not imply any functional relationship.

As in the overall correlation, ERA and ASCAT show the highest correlation of ranks, and with that the most similarities in soil moisture distribution, for most climate classes. Except for the B class, the correlation is significantly higher than for correlation of both products with SMOS. This indicates that in most regions, ERA and ASCAT show similar patterns, while SMOS is quite different from both of them. An exception are the Af and Am classes, where the two remotely sensed products show the only high correlation, possibly they are both similarly influenced by the vegetation cover. The BW class is the only one showing the highest correlation for ERA and SMOS. This is not surprising, as ASCAT is known to be less accurate in very dry areas, which is generally assigned to volume scattering in dry, loose sand and the systematic orientation of sand ripples and dunes (Bartalis *et al.*, 2006b; Dorigo *et al.*, 2010).

3.3.2 Selected regions

3.3.2.1 Time series of spatial mean

Fig. 3.6 shows time series of $\bar{\theta}(t)$ of the three different products for the five 120-grid-point-study regions presented in sec. 3.2.2. In general, all of them show similar trends in all regions. Seasonality of precipitation is visible in the Aw, BS and Cw climates (Fig. 3.2), this trend is reproduced in all soil moisture products. But also in the BW climate, all of them show comparable peaks. In the Cf climate, having less pronounced peaks and no yearly cycle, they show less similarity.

The absolute values, however, are different. As was already reported in previous studies (Albergel *et al.*, 2012), ERA tends to be wetter than the remotely sensed products. Especially in the Australian desert (BW) soil moisture is overestimated with values around $0.2 \text{ m}^3/\text{m}^3$.

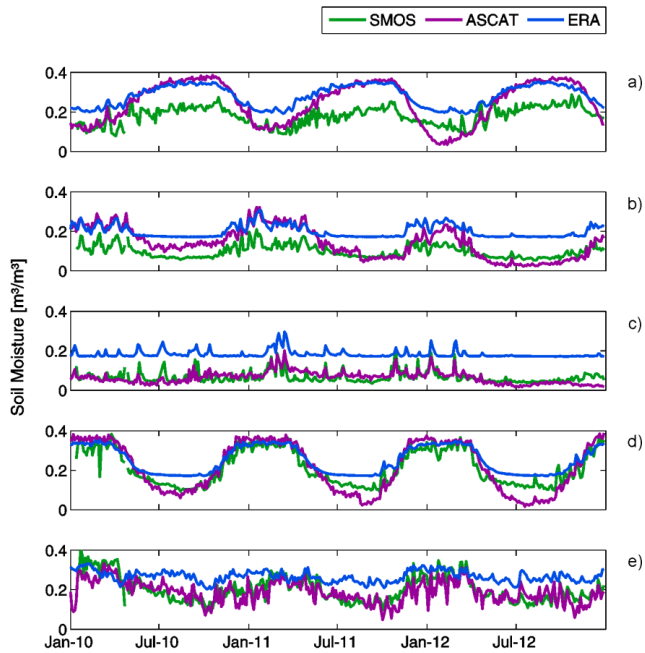


Fig. 3.6: Time series of spatial mean of the three soil moisture products for the selected regions a) Aw Africa, b) BS Africa, c) BW Australia, d) Cw Africa, and e) Cf America.

Showing less variability, it gets obvious that ERA holds not only low spatial variability as was already observed in sec. 3.3.1.1, but also lower temporal variability than the other products. SMOS and ASCAT show similar absolute values, except for the Aw climate and the BS region until June 2011. In both regions ASCAT tends to show higher values than SMOS. For the BS region, ASCAT approaches the SMOS values with the introduction of the new SOMO PPF version. In general, ASCAT shows higher fluctuations than the other two products, which can be related to lower sensing depth of C-Band, but is also influenced by the porosity data, used for the conversion of relative into absolute soil moisture values.

Similar peaks in all study regions show that in general temporal patterns are reproduced well in all soil moisture products, while the absolute values are highly influenced by the retrieval approach.

3.3.2.2 Spatial mean and variance

Fig. 3.7 shows the relationship of $\bar{\theta}(t)$ and $\sigma^2(t)$ for the six example regions and the three soil moisture products. Li and Rodell (2013) state that at large extent scales this relationship is mainly

controlled by physical processes such as precipitation and evapotranspiration. From the differences within the different products in one climate zone, it gets obvious, that it is not only these natural factors influencing the relationship, but it is also depending on characteristics inherent to the product.

For most of the example regions, ASCAT and ERA show a similar convex relationship, although less pronounced in ERA. This relationship was already found in studies at smaller extent scales. Famiglietti *et al.* (2008) describe the factors influencing this relationship to be quite variable. In the cases of Aw, BS, and Cw, the relationship is the result of the strong seasonality of precipitation, and with that of soil moisture, that can also be observed in Fig. 3.6 b) and c). During the precipitation season (March-November for Aw, November/December-March for BS and Cw, see Fig. 3.2), the whole region is wet and thus shows high $\bar{\theta}(t)$ and low $\sigma^2(t)$, during the dry season in winter, $\bar{\theta}(t)$ and $\sigma^2(t)$ are low. During the wetting period, $\bar{\theta}(t)$ and $\sigma^2(t)$ rise, when rainfalls start to occur, while the drying lowers $\bar{\theta}(t)$ and again raises $\sigma^2(t)$. In the Aw and especially in the Cw region, the wetting period (around February-April and September-November, respectively) shows higher $\sigma^2(t)$ than the drying period (around March-May and October-November, respectively), indicating that the drying occurs more homogenous than the wetting.

The convex relationship is less pronounced in the BS region; especially in ERA the decreasing trend with high mean soil moisture is only weak. As the precipitation season lasts from around January until May (Fig. 3.2 b)), the whole period shows high $\bar{\theta}(t)$ and similar $\sigma^2(t)$.

In the BW region, SMOS and ASCAT show similar low average $\bar{\theta}(t)$ and average $\sigma^2(t)$, while ERA shows rather high $\bar{\theta}(t)$, corresponding to the finding in sec. 3.3.2.1, that the soil moisture is quite high for a desert region. The relationships are more or less positive linear for all three products, with many values around the average $\bar{\theta}(t)$ and few higher soil moisture values. This results from the generally dry soil with rare small scale precipitation events causing higher mean soil moisture and higher variance at the time of these events.

The Cf region shows a less prominent convex shape for ASCAT and ERA. However, for both products, $\bar{\theta}(t)$ tends to be smaller from June to August than from January to May, but $\sigma^2(t)$ does not show a seasonal dependence. Fig. 3.8 shows the same relationship for in situ data from 42 stations of the Soil Climate Analysis Network (SCAN) (Schaefer *et al.*, 2007) within the study area, downloaded from the International Soil Moisture Network (Dorigo *et al.*, 2011). It was measured with Hydra Probes at a depth of 0.05 cm, and therefore consists of point measurements, which are valid for a small soil volume only, while the other products give an average value over a much larger area. This explains

the higher $\sigma^2(t)$ of the SCAN data. Nevertheless, its relationship of $\bar{\theta}(t)$ and $\sigma^2(t)$ shows the same convex form as ASCAT and ERA and a similar seasonal distribution.

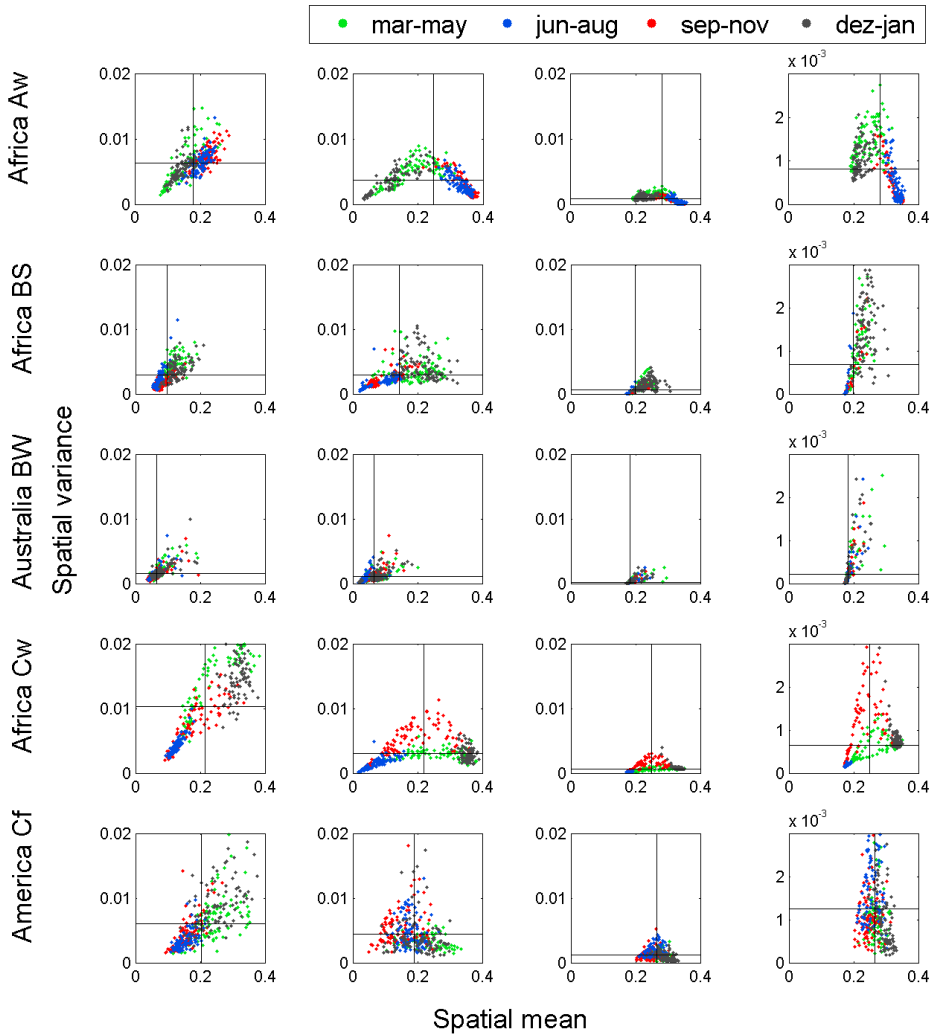


Fig. 3.7: Relationship of $\bar{\theta}(t)$ and $\sigma^2(t)$ of soil moisture for the selected regions. Left side shows SMOS, middle left ASCAT, middle right ERA Interim and right is zoomed into the ERA Interim plots. The red lines indicate the means of $\bar{\theta}(t)$ and $\sigma^2(t)$.

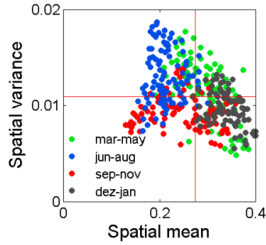


Fig. 3.8: Relationship of $\bar{\theta}(t)$ and $\sigma^2(t)$ for in situ measurements of SCAN in the Cf region in America.

SMOS shows a more or less pronounced positive linear relationship of $\bar{\theta}(t)$ and $\sigma^2(t)$ for all regions. This indicates that especially during the wetter periods the relationship is more influenced by the retrieval method than by natural factors for this product. A similar behavior was found for an AMSR-E soil moisture product in the United States by Li and Rodell (2013), who link it to the fact that the median mean of the retrievals is always near or below the mid-range soil moisture. The lack of high soil moisture values is probably the cause for the different form of the relationships compared to the other products. This is further suggested by the fact that average $\bar{\theta}(t)$ is lower for SMOS, while the average variance is similar for SMOS and ASCAT. The seasonal distribution of data points is similar in relation to $\bar{\theta}(t)$, so the general temporal patterns are covered by all products.

Overall, the relationship of $\bar{\theta}(t)$ and $\sigma^2(t)$ can be explained by natural factors, particularly the precipitation regimes of the respective study areas, for ERA and ASCAT, while for SMOS the retrieval method shows more influence, in particular during wet periods.

3.3.2.3 Contributions to the spatial variance

Splitting $\sigma^2(t)$ into a temporal invariant part, $\sigma^2(\bar{\theta}(n))$, and a temporal variant part, consisting of the sum of $cov(\bar{\theta}(n) A_{n,t})$ and $\sigma^2(A_{n,t})$, we gain information about the type of influencing factors on $\sigma^2(t)$ and their proportions.

The temporal development of the two components is shown in Fig. 3.9 in percentage of $\sigma^2(t)$ for the three soil moisture products and the five example regions.

For the Aw study area in Africa, a kind of annual cycle can be observed, but it is not the same among the different products, and especially in ERA the proportions of contributions of variant and invariant parts change quite often. These proportions get up to 1087 % for the temporal invariant part, while at the same time the temporal variant parts gets negative with values as low as -1087 %. This is

induced by the covariance part of the temporal variant component. Negative values of the latter indicate a change of relation between temporal mean and anomaly (Mittelbach and Seneviratne, 2012). This is the only study area, where ERA and ASCAT show a more similar behavior than SMOS and ERA.

For the BS study region SMOS and ERA show a similar seasonality: While the variant contribution dominates in the precipitation season from November to March (see Fig. 3.2 b)), during the dry season this part decreases. The maximum value of ERA's invariant part increases up to 5113 %. For ASCAT, the variant component is higher all the time until August 2011 and from this time on it shows a similar behavior as the other products.

Similar patterns with low temporal invariant part in the precipitation season and high temporal invariant part in the dry season can be found for the African Cw region. ASCAT again shows this periodic behavior only from 2011 on, indicating that the change of the SOMO PPF version favored the seasonal patterns.

In both regions it gets obvious, that dynamic variables, especially climate variables like precipitation and evaporation, control $\sigma^2(t)$ in wet seasons, while in dry seasons invariant factors, for example soil characteristics and topography, dominate.

This partly agrees with the findings of Grayson *et al.* (1997), who analyzed the control factors of soil moisture patterns on the extent scale of catchments. They distinguished between local controls, i.e. soil properties and local terrain, dominating spatial patterns in wet seasons and nonlocal controls, i.e. catchment terrain, controlling the patterns in dry seasons. However, on the larger extent scale of our study, the catchment terrain can be considered as a local control, and precipitation and evaporation are less uniform over the larger area. Considering the fact, that the aforementioned study analyzes influencing factors distinguished by different scales, while this study differentiates between dynamic and constant factors, and that both studies work on different extent scales, the results are quite similar.

The Australian BW study area shows a dominating variant part for ASCAT nearly all the time, while for SMOS and ERA there are a lot of fluctuations between the different parts, probably induced by local precipitation events. The invariant part of ERA rises up to values of 1514 %.

In the America Cf region SMOS shows a dominance of the temporal invariant part in summer (June-August) and of the variant part in winter, while ASCAT is always dominated by the variant part in this region. ERA shows a less pronounced seasonality and higher fluctuations, with mostly the invariant contribution being the dominant part.

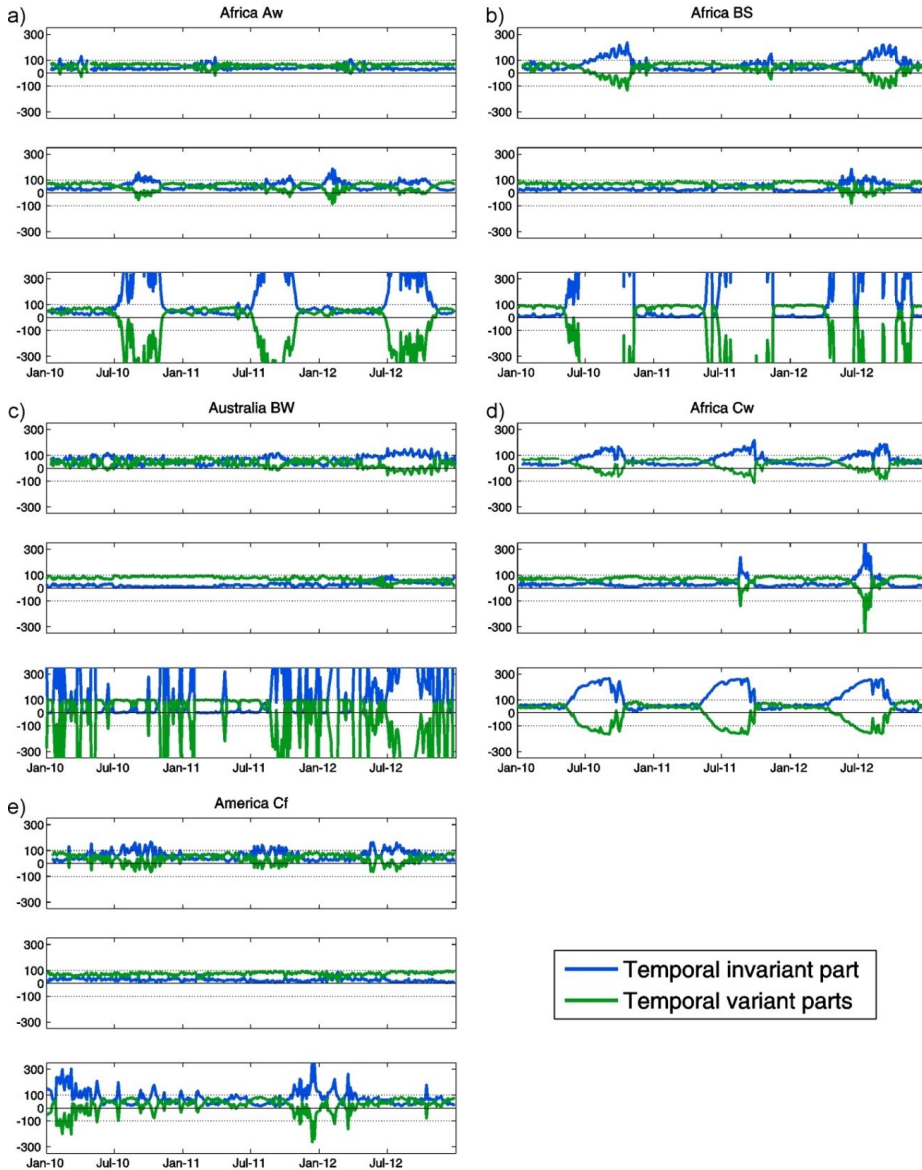


Fig. 3.9: Time series of percentages of the single contributors to $\sigma^2(t)$ for the selected regions a) Africa Aw, b) Africa BS, c) Australia BW, d) Africa Cw, and e) America Cf. The top shows SMOS, the middle ASCAT and the lower plot ERA. The ERA plots do not always show the maximum values of the temporal invariant part and minimum values of the temporal variant parts. These plots are: a) where maximum of the temporal invariant part is 1087 %, b) where maximum is 5115 %, and d) where maximum is 1514 %. The respective minima of the temporal variant parts are the negative counterparts of the maxima.

For SMOS, the average contribution of the temporal invariant component to $\sigma^2(t)$ is higher than the variant part with values between 62 % and 68 %. An exception is the Aw region, where the invariant part only contributes 41 %. The opposite can be observed in ASCAT: With values between 26 % and 38 % the contribution of the invariant part is always lower than the contribution of the variant part, with exception of the Aw region, where the invariant part contributes 53 % to $\sigma^2(t)$. For ERA, $cov(\bar{\theta}(n) A_{n,t})$ is often largely negative, and so the whole variable component gets negative, while the invariant part balances that with values of more than 100 %, with the exception of the Cf region in America, where the contribution of the variable component is 21 %.

While in previous studies on areas up to 50,000 km² with in situ measurements from networks, a dominant influence of the temporal invariant component was found (Mittelbach and Seneviratne, 2012; Brocca *et al.*, 2014), on large extent scales it could be expected, that the temporal variant part controls $\sigma^2(t)$, as precipitation and other climatic influences are generally considered to be the prevailing factors on soil moisture distribution (Famiglietti *et al.*, 2008). However, this study shows that this may be only seasonally effective.

It gets obvious, that the contributions to $\sigma^2(t)$ are quite different for the three products. This cannot completely reflect natural conditions in the respective regions, but is highly influenced by the method of soil moisture estimation. The time series of SMOS and ERA show similar behavior in most study areas, and for both the temporal invariant component plays an important role, while ASCAT is stronger controlled by the temporal variant part. Calculation of both SMOS and ERA includes information about spatial invariant factors, while the change detection method of ASCAT assumes invariant factors like topography and surface roughness to be constant (Naeimi *et al.*, 2009), therefore does not account for them and essentially measures the temporal variant factors.

3.3.3 Scaling

Fig. 3.10 shows the effects of scaling for the three soil moisture products and the three study areas. The left shows the results for changing support scales, the right for changing extent areas.

Slopes and intercepts of the line fitted to the $\log \text{area vs. } \log \sigma^2(t)$ relationship (corresponding to the fractal power μ_s and the logarithm of the parameter c_s , respectively) and the corresponding R² values for the support study can be found in Table 3.2.

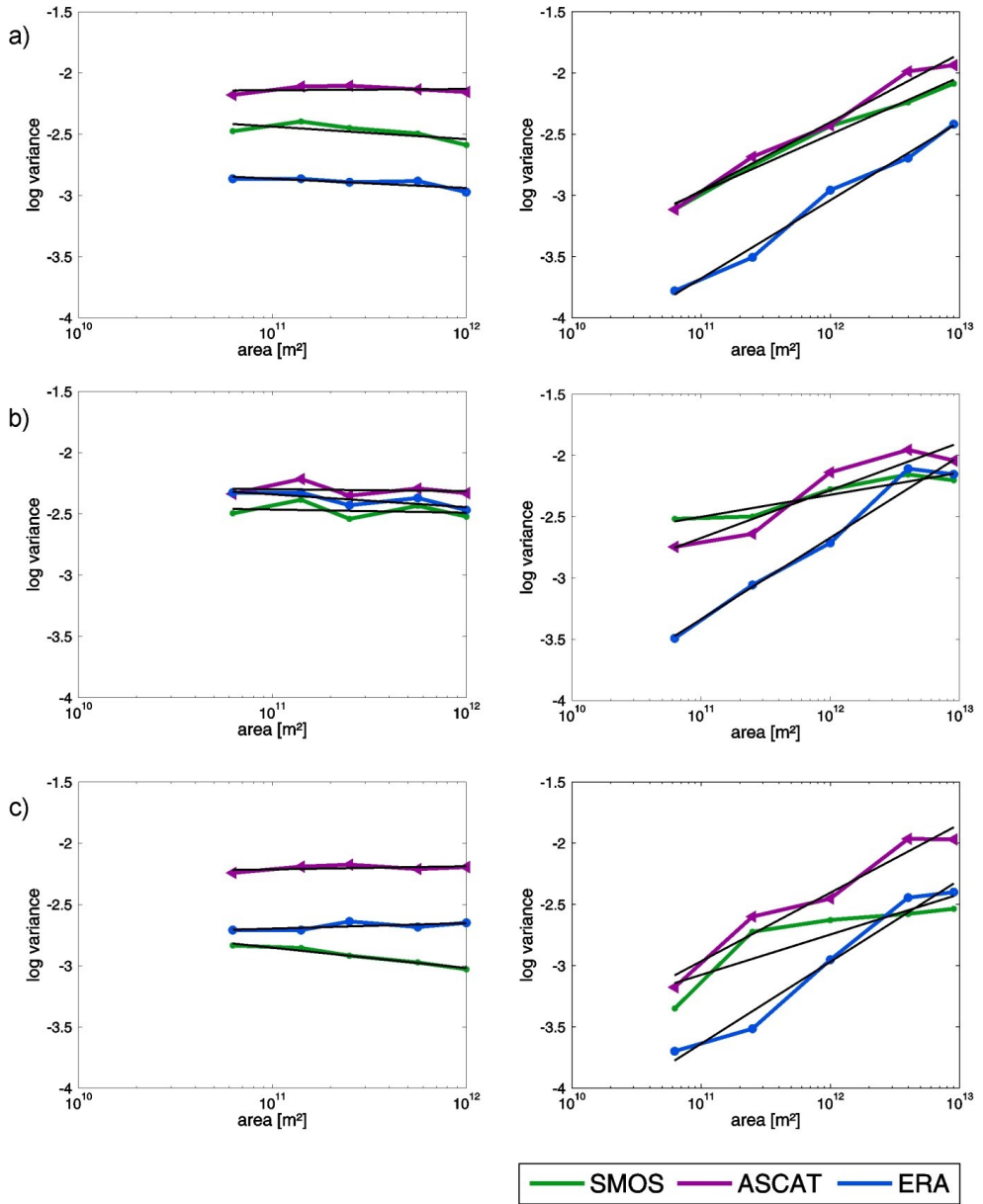


Fig. 3.10: Relationship of support scale (left) and extent scale (right) area vs. $\sigma^2(t)$ for a) North America, b) Africa, and c) Asia. The black lines show the fitted linear relationship.

Table 3.2: Slope (fractal power μ_s), intercept ($\log c_s$), and coefficient of determination (R^2) for support scale changes from 250 km to 1000 km for the three soil moisture products and the three study areas.

	SMOS			ASCAT			ERA		
	slope	intercept	R^2	slope	intercept	R^2	slope	intercept	R^2
America	-0.10	-1.31	0.48	0.01	-2.25	0.02	-0.08	-2.03	0.64
Africa	-0.03	-2.18	0.04	-0.02	-2.13	0.02	-0.10	-1.19	0.62
Asia	-0.17	-1.02	0.97	0.02	-2.49	0.22	0.05	-3.20	0.44

Fig. 3.10 (left), as well as Table 3.2, show that there is negligible change in $\sigma^2(t)$ with support area. For SMOS, the trend is always negative, which indicates a general decrease of $\sigma^2(t)$ with support area, although not pronounced. ASCAT shows very low slope values without distinct trend, just like ERA, which shows only slightly higher slope values and also no distinct trend. In general, the slopes found in this study are distinctly lower than the ones found by Rodriguez-Iturbe *et al.* (1995) and Manfreda *et al.* (2007), who found slopes between -0.32 and -0.12 for the surface soil layer. The intercepts are similar for all of the products and all study areas. For ASCAT, they show the smallest range of values, while for ERA they are most variable. The R^2 values, indicating how good the linear fit is, are very low for ASCAT and higher for ERA. For SMOS they are quite variable, with a very low value in Africa and a high value in Asia.

Generally, the pronounced power law decay of $\sigma^2(t)$ with increasing support scale that was found by Rodriguez-Iturbe *et al.* (1995) on scales up to 1 km² could not be detected on the large scale of the global soil moisture products. Only SMOS showed a similar behavior in the Asian study area.

Although neither slopes nor R^2 values are very similar for the different products, in Fig. 3.10 the change of trend in $\sigma^2(t)$ is quite similar for all of them, especially for the study area in Africa, where there is a sharp decrease of variance for the 500 km scale and then an increase for the 750 km scale. This can be explained by values getting more similar with averaging soil moisture values, because small scale characteristics, outliers and noise will average out.

The relationship of \log extent area vs. $\log \sigma^2(t)$, on the contrary, shows a distinct slope (fractal power μ_e), with a positive trend for all soil moisture products in all study areas (Table 3.3 and Fig. 3.10 (right)). The slope values are always lowest and most variable for SMOS and highest and in a narrow range for ERA. The R^2 values are also higher than for the support study. So, apart from some deviances, the linear increase of the \log area vs. \log variance relationship, and with that the power law increase of $\sigma^2(t)$ with extent area, can be observed in the global soil moisture products. Especially for ERA, this is true for all study areas. ASCAT shows a lower goodness of the linear fit for

Africa, and looking closer on Fig. 3.10, shows, that the linear relationship is stronger for the 500 to 2000 km scales. For SMOS, the linear relationship is less strong in all study areas except America.

The linearly increasing variance with extent scale is in accordance with the results of Famiglietti *et al.* (2008), who found a similar behavior for scales of 2.5 m to 50 km. While in the study of Famiglietti *et al.* (2008) the land cover and climatic characteristics did not change much between the different scales, the extents worked with here require the inclusion of very different conditions. Deviances of the linear fit may be due to these differences: The increase of $\sigma^2(t)$ with extent is mainly driven by the increasing number of climate regions included in the study area. A new climate class in the study area will lead to a steeper slope, whereas, if the region is only extended into an already included climate class - and especially if the fractions stay similar - the slope is flat. The climate classes included in the respective study areas can be observed in Fig. 3.3. The higher variability of climate and land use may also be the reason for the higher slopes compared to Famiglietti *et al.* (2008): While a slope of 0.09 was reported for the relationship of log area vs. log standard deviation, which corresponds to a slope of 0.18 for the relationship of log area vs. log variance, the slopes found in this study are mostly higher than that (see Table 3.3).

In the African study area, the plots show relatively low slopes and R^2 values, especially for SMOS and ASCAT. All products exhibit a flattened slope between 2000 and 3000 km. The reason can be found in quite similar fractions of climate zones in the 2000 km and 3000 km scales (Fig. 3.3). This is also the case for the study area in Asia, where for the 1000 km and 2000 km scales the linear relationship is more pronounced, because new climate regions are included, and flatten out for the 3000 km scale, because the fractions of different climate zones stay similar compared to the smaller scales. As for the African area, SMOS is an exception here and does not show a linear relationship at all. The American study area, on the contrary, shows very good fits for all products, which can be related to the very heterogeneous area already in the smallest extent but also in higher extents (Fig. 3.3). Both, slope and R^2 are quite similar for the three products.

The intercept ($\log c_e$) of the relationship is equal to the logarithm of the parameter c of the scaling law and thus corresponds to the theoretical $\sigma^2(t)$ of an area equal to 1 m^2 . Consequently, a smaller intercept results in less small scale variability according to the power law. Tab. 3.3 shows that values of intercept are always highest for SMOS and lowest for ERA. SMOS also shows the highest deviances between the different study areas, while for ERA the intercepts are very close to each other. In general, ERA showed, in contrast to the remotely sensed products, similar slopes and intercepts in all study areas, and also a high fit to the linear relationship, and thus reveals a universal scaling across the different regions at the investigated length scales for a temporal average.

Table 3.3: Slope (fractal power μ_e), intercept ($\log c_e$), and coefficient of determination (R^2) for extent scale changes from 250 km to 3000 km for the three soil moisture products and the three study areas.

	SMOS			ASCAT			ERA		
	slope	intercept	R^2	slope	intercept	R^2	slope	intercept	R^2
America	0.47	-18.71	0.99	0.56	-20.96	0.98	0.64	-24.65	0.99
Africa	0.18	-10.32	0.88	0.39	-16.02	0.88	0.67	-24.56	0.97
Asia	0.33	-15.42	0.74	0.56	-21.00	0.95	0.67	-25.34	0.97

This scaling law is useful for the downscaling of low resolution soil moisture. It has to be considered, that this law might not be valid for much smaller scales. This gets obvious from the theoretical $\sigma^2(t)$ of 1 m², which corresponds to 10 to the power of intercepts and therefore are extremely small (see Tab. 3.3). This results from the large support area of the soil moisture data used in this study, which gives a mean value over an area of 0.75° x 0.75° and, in contrast to point-scale in situ data with sampling points over a large area, averages out the small scale variance.

Fig. 3.11 shows the temporal evolution of slopes of the linear relationship $\log \text{area}$ vs. $\log \sigma^2(t)$ for the three study areas and the three products over the study period. In all areas a seasonal cycle of slopes gets visible for all products. This cycle is most pronounced for ERA, but the other products show a similar behavior and similar peaks. This cycle is introduced by seasonal variations in the climate classes within the regions. Especially, if the different climate classes within the respective study area show different precipitation cycles resulting in different soil moisture conditions in the different climate classes at one time and more similar conditions in another season, the change of $\sigma^2(t)$ with extent scale and with that of the slopes of the scaling function will vary during the year. The African region, for example, consists mainly of the Aw climate class on small extent scale, and mainly of Aw and BW climate on larger extent scale. While in the BW climate class, the soils are rather dry during the whole year, the Aw class shows distinct seasonal variations of soil moisture (see Fig. 3.2), resulting in higher variances, and thus steeper slope during the precipitation season in the Aw class.

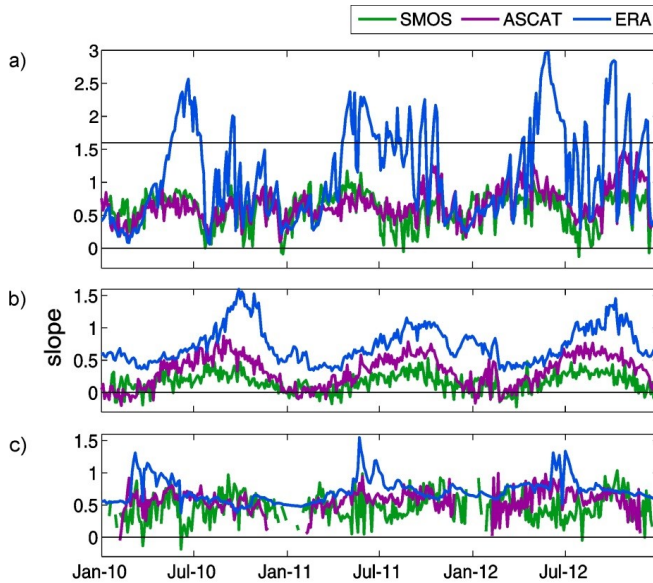


Fig. 3.11: Temporal evolution of slope (fractal power μ_e) of the relationship \log extent area vs. $\log \sigma^2(t)$ for the study area in a) America, b) Africa, and c) Asia.

The relationship of extent area and $\bar{\theta}(t)$ is illustrated in Fig. 3.12. The trend is similar for all of the products, but quite different between the different study areas: While in the American and in the Asian study areas, the two study areas with similar climate classes, the mean value increases with extent scale, in the African area the mean value shows a pronounced decrease with scale due to the large fraction of the BW (desert) climate class at higher extent scales. This shows that the behavior of mean value with changing extent is highly dependent on the selection of the study area, as the different climate classes have a high influence on the relationship.

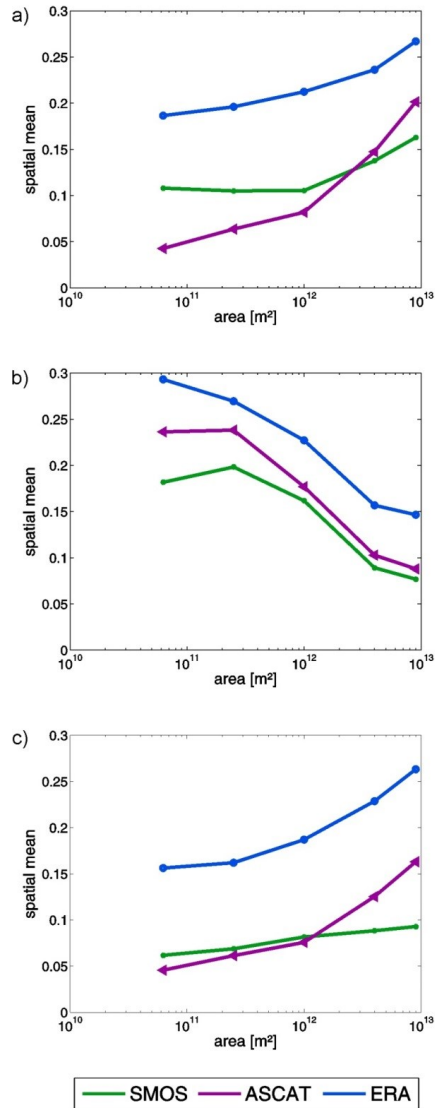


Fig. 3.12: Relationship of extent scale area vs. $\sigma^2(t)$ for a) America, b) Africa, and c) Asia.

The relationships presented here are useful for up- or downscaling of soil moisture. Especially ERA showed a universal scaling across the different study areas. This study shows that it is important to account not only for the characteristics of the different products, but also for the climatic conditions, land cover and seasonal variations in the region of interest.

3.4 Conclusions

One modeled and two remotely sensed soil moisture products of the years 2010 to 2012 were analyzed on their global spatial and temporal variability on basis of the Köppen-Geiger climate classification. The products show overall similar patterns of spatial soil moisture distribution, although not in absolute values. Deviances in several regions show individual retrieval characteristics for the respective products. Based on rankings of MRDs, ASCAT and ERA are most similar, while ERA and SMOS show least similarities. Best consistence is found for arid climates, as they normally contain low vegetation.

The analysis of selected regions in different climate classes exhibited, that ASCAT generally shows higher variability of soil moisture than SMOS, and especially than ERA. The relationship of $\bar{\theta}(t)$ and $\sigma^2(t)$ shows a similar positive linear relationship for SMOS in all regions, indicating that this relationship is influenced by sensor and retrieval characteristics. ASCAT and ERA show similar convex relationships for most regions. The decomposition of $\sigma^2(t)$ into temporal variant and invariant components indicates higher influence of the variant part on ASCAT and of the invariant part on SMOS and ERA, which also show similar annual patterns. This is due to ASCAT's change detection method for soil moisture estimation.

In general, it was found that the temporal patterns are reproduced well in all products, while the absolute values are highly affected by acquisition and processing methods. The spatial patterns, however, are influenced differently by retrieval approach in different study areas and among the different products. The relationship of spatial mean and spatial variance is generally introduced by precipitation patterns in the respective regions, while SMOS is affected by its retrieval approach especially in wet periods. The factors controlling $\sigma^2(t)$ are also heavily dependent on acquisition method. Nevertheless, the analysis of temporal stability shows that the general spatial patterns can still be similar.

The change of $\sigma^2(t)$ with increasing support and extent scale was investigated in three different areas. Results indicate that $\sigma^2(t)$ stays similar in all areas and for all products on support scales of 250 km to 1000 km. With increasing extent areas from 250 to 3000 km, $\sigma^2(t)$ increases for all products and all study areas, most of them according to a power law. The products show a similar, but seasonal variable behavior in the extent scale study, with the exception of SMOS, that was less close to the power law increase with extent scale in two areas. These relationships of area and variance have to be considered in the processes of up- and downscaling of the soil moisture products. For the observed range in extent and an average over time, ERA showed a universal scaling

across the different regions. Such a consistent scaling behavior was not observed for ASCAT and SMOS. For these products, slope and intercept of the scaling laws were found to be dependent on the region of interest. It would be of great interest to know whether the ERA scaling behavior is also valid for the smaller lengths and under which conditions and at which length scales this scaling eventually breaks down.

This study exhibits that the statistical patterns of soil moisture products are influenced by modeling or retrieval method. This influence, as well as spatial and temporal characteristics of the products can vary from region to region. Therefore, the results from validation with in situ data cannot be transferred to other regions and a global evaluation needs a cross-comparison of soil moisture products. For further usage of the products in a specific region, for up- and downscaling and for data assimilation, their different spatio-temporal characteristics have to be considered.

4 Relationship of Vegetation Optical Depth and Radar Vegetation Index for the Aquarius mission

4.1 Introduction

Microwave remote sensing of soil moisture, both active and passive, have to account for the vegetation covering the soil. Vegetation cover affects the emitted passive microwave signal from the soil, which contains the information about soil moisture, in several ways: It attenuates or absorbs and scatters the soil emission and emits radiation itself (Njoku and Entekhabi, 1996). In active microwave remote sensing, vegetation disturbs the signal sent back from the soil to the sensor through surface scattering by attenuation and volume scattering effects in the canopy layer (Ulaby *et al.*, 1979). Therefore, the influence of vegetation on the microwave signal has to be quantified in any algorithm for soil moisture retrieval.

The most common algorithms for passive microwave sensors are based on the radiative transfer equation of the τ - ω model (Mo *et al.*, 1982), where the vegetation is quantified by VOD (τ) and the single scattering albedo ω . While the single scattering albedo describes the scattering effects in a canopy, VOD describes the attenuation of the soil radiation through the canopy layer. It is primarily determined by VWC (Van de Griend and Owe, 1993), and other influencing factors are the geometrical structure of the vegetation and microwave frequency (Njoku and Entekhabi, 1996). Several studies found a linear relationship of VOD with VWC and an empirically derived b-parameter according to frequency and vegetation type (Jackson and Schmugge, 1991; Van de Griend and Wigneron, 2004), which also accounts for the vegetation geometry.

There are several ways to obtain VOD, most of them using vegetation indices of different sources. The MPDI, a vegetation index of radiometer brightness temperatures, is used for an analytical derivation of VOD together with soil moisture in the LPRM (Owe *et al.*, 2008). This model is used for example for the retrieval of soil moisture from passive microwave sensors for the ESA Climate Change Initiative product (Dorigo *et al.*, 2015).

The SMOS satellite is the first mission specifically designed for remote sensing carrying a radiometer measuring at L-band (Kerr *et al.*, 2010). In the SMOS Level 2 processor for soil moisture, VOD is derived through a 2-parameter retrieval method using multiangular and bi-polarization observation. However, for initialization values and if there are not sufficient angular measurements, it is relying on

the linear relationship of VWC and VOD. VWC is estimated from Leaf Area Index (LAI) taken from ECOCLIMAP (Kerr *et al.*, 2012).

The Aquarius satellite is equipped with L-band radiometer and radar, both instruments have a resolution of about 100 km (Le Vine *et al.*, 2007). It is primarily dedicated to the measurement of ocean salinity, but also a soil moisture product is derived from radiometer measurements in a single channel algorithm (Bindlish *et al.*, 2015). There, VOD is estimated from VWC, which is derived from MODIS Normalized Difference Vegetation Index (NDVI).

A new instrument for soil moisture monitoring, the SMAP Satellite (Entekhabi *et al.*, 2010) was launched recently. Like Aquarius, it consists of a radiometer and radar, the radiometer measuring at 1.4 GHz in a resolution of 36 km, and a radar instrument at 1.26 GHz with a resolution of 3 km. Three soil moisture products will be available from this mission, one retrieved from the radar instrument (Das *et al.*, 2011; Das *et al.*, 2014), one from the radiometer, and a combined product in an intermediate resolution of 9 km. In the current SMAP baseline algorithm for passive soil moisture retrieval the retrieval of VOD from VWC approached by NDVI climatology from MODIS is used (O'Neill *et al.*, 2014).

Although they are widely used, current visible and infrared vegetation indices from optical remote sensing have several limitations, as they are only available in daytime and cloud free conditions. Furthermore, they get saturated over high vegetation, a problem especially known from NDVI (Jackson *et al.*, 2004).

However, vegetation indices can also be derived from active microwave remote sensing. A common index is the RVI (Kim and van Zyl, 2009), derived from backscattering coefficients of different polarizations. Because of higher penetration depth of the vegetation, especially at L-band, and the independence of daytime and weather conditions, the use of RVI for the estimation of VOD would be an advantage for soil moisture retrieval algorithms. Especially for SMAP and Aquarius soil moisture products using RVI will be useful, as radar measurements are available from the same platform and therefore without time lag to brightness temperature measurements. Therefore, the purpose of this study is to develop and analyze a method to derive VOD from RVI.

Until recently, few studies have tried to link RVI to biophysical vegetation parameters. Kim, Y. *et al.* (2012) found a strong correlation for L-band RVI and VWC, LAI and NDVI for soybean and rice crops and could establish linear retrieval equations for estimating VWC from RVI, especially by combining both crops. Then again, Colliander (2012) found, that RVI and VWC were not well correlated over a variety of croplands (bare soil, soybean, wheat, corn and grass). Rowlandson and Berg (2015) investigated soybean, winter wheat and spring wheat fields for a smaller range of VWC than Kim, Y.

et al. (2012) and found good correlation for soybean RVI and VWC and a moderate correlation of RVI and LAI for soybean and spring wheat and a combination of soybean and wheat.

However, even if VWC can be derived from RVI, for the estimation of VOD it is still necessary to choose the right scale relationship expressed as b-parameter additionally to the estimated parameters of the relationship of VWC and RVI. This b-parameter is empirically derived mainly on small scale in local studies. If VOD could be derived directly from RVI, this b-parameter could be avoided and the parameters of this relationship can be derived on the basis of global statistics. Furthermore, the previous studies have focused on croplands, while the estimation of VOD in highly vegetated areas like forests would be of high interest due to the problem of saturation of optical vegetation indices.

This study will investigate the direct relationship of RVI and VOD on a global scale for a variety of land use classes by using radiometer and radar measurements from the Aquarius satellite. Moreover, it will test the influence of VOD derived from RVI on soil moisture retrieval. The following section will give an overview on the data and radiative transfer models used in this study. Then VOD, retrieved from Aquarius brightness temperatures with LPRM will be verified and in the subsequent section the relationship between VOD and RVI will be described and validated. In the last section, the newly derived relationship will be tested on its influence on soil moisture inversion in a sample area.

4.2 Data and Methods

4.2.1 Data

4.2.1.1 Aquarius

Aquarius is a joint mission of NASA and the Argentine Space Agency primarily for measuring sea surface salinity with active and passive L-band sensors, but a soil moisture product is also available (Bindlish *et al.*, 2015). The satellite is in a polar orbit with an altitude of 657 km and has a repeat orbit of 7 days. It carries two instruments, a radiometer measuring at 1.413 GHz and a scatterometer at 1.26 GHz, arranged in a pushbroom configuration at three incidence angles: the inner beam at 28.7°, the middle beam at 37.8° and the outer beam at 45.6°. This results in an overall swath width of 390 km with footprints consisting of ellipses with principal axis dimensions of 76x94 km, 84x120 km and 96x156 km for the inner, middle and outer beam of the scatterometer, respectively, while the radiometer footprints are slightly smaller (Le Vine *et al.*, 2007).

This study uses three years of Aquarius Level 2 brightness temperatures and backscattering coefficients, version 2.0, from September 2011 to August 2014. Only observations from the middle beam (37.8°) are used, as it is closest to the 40° angle of SMAP and the results will be easier to adopt for that mission. Brightness temperatures and backscattering coefficients, as well as land surface temperature from the Global Data Assimilation System of the National Centers for Environmental Prediction, which is delivered with the product, were gridded in footprint scale with a modified sampling approach. The first seven days of data were used to define a grid and all subsequent observations with centers less than 0.05° away from a grid point are assigned to this grid point. In some cases this leads to the inclusion of some observations in multiple grid cells, while observations that are not within this distance to a grid point are excluded from the study. More detailed information on the gridding scheme can be found in McColl *et al.* (2014) and Piles *et al.* (2015).

4.2.1.2 IGBP

The dominant class of landcover of an Aquarius footprint was determined through the 2005 MODIS MCD12Q1 International Geosphere-Biosphere Programme (IGBP) product (Friedl *et al.*, 2002). The product distinguishes between 17 land cover classes on a resolution of 500 m. For this study, the IGBP data was resampled using the predominant land cover class (Piles *et al.*, 2015; Konings *et al.*, submitted).

4.2.1.3 SMOS product

The SMOS Level 2 product, version 5.51, is compared to VOD and soil moisture retrieved with LPRM from the Aquarius brightness temperatures. The SMOS product contains soil moisture and VOD, which are retrieved by the Level 2 processor from the Level 1 product brightness temperatures (Kerr *et al.*, 2012). The SMOS Level 2 processor is mainly based on the L-MEB model (Wigneron *et al.*, 2007). SMOS VOD is currently the only publicly available dataset of L-band VOD.

In the forward model brightness temperatures are simulated and a cost function is minimized between simulated values and multi-angle measured brightness temperatures. A higher number of different angles allows for a more accurate solution of the cost function. Soil moisture and VOD can be retrieved in a 2-parameter retrieval, if enough brightness temperature observations in different angles are available, otherwise a 1-parameter retrieval is attempted and only soil moisture is retrieved, while VOD is fixed by its initialization value. This starting value of VOD is retrieved from

observations of one of the last three days or calculated from VWC, derived from the ECOCLIMAP LAI and b-parameter according to vegetation type.

For this study, SMOS VOD and soil moisture product were filtered by their respective data quality indices, which are the retrieved standard deviation reflecting radiometric uncertainty and the Chi^2 values, showing the goodness of retrieval fit (between measured and simulated brightness temperature). Both are delivered with the product.

The Level 2 product is delivered on the ISEA grid, which has a grid spacing of approximately 15 km. For proper comparison with the LPRM results, a circle with a radius of 0.5° was defined around each Aquarius grid point, which approximately corresponds to the size of the Aquarius footprint. SMOS VOD and soil moisture (hereafter referred to as VOD_{SMOS} and SM_{SMOS} , respectively) within these circles were averaged taking into account their distances from the center grid point.

4.2.1.4 MODIS NDVI

The MODIS/TERRA NDVI product MOD13C1 was used for an additional comparison of LPRM VOD. Its spatial resolution is 0.05° , the temporal resolution 16 days. It was downloaded from NASA's Earth Observing System data gateway (<http://reverb.echo.nasa.gov/>). The NDVI was aggregated to the size of Aquarius footprints using the same method as for SMOS data.

4.2.2 Methods

Fig. 4.1 gives an overview of the study concept. The single components are presented in the previous and following sections. From Aquarius brightness temperatures VOD_{LPRM} and soil moisture SM_{LPRM} are retrieved in the LPRM, while RVI is derived from Aquarius backscattering coefficients. The relationship of VOD_{LPRM} and RVI is then analyzed on a global basis. Through the established relationship, VOD_{RVI} can be derived from RVI. Global VOD_{LPRM} and VOD_{RVI} patterns are analyzed in comparison to VOD_{SMOS} and MODIS NDVI, the same is done for SM_{LPRM} and SM_{SMOS} .

A closer examination of the different VODs is performed in a selected target area. The influence of VOD_{RVI} in comparison to VOD_{LPRM} on soil moisture inversion is tested in the L-MEB model, as each of the two is used as input parameter in different model runs. The results with the two different input datasets VOD_{LPRM} and VOD_{RVI} , $\text{SM}_{\text{LMEB/LPRM}}$ and $\text{SM}_{\text{LMEB/RVI}}$, respectively, are analyzed on their differences; their patterns and temporal development are compared to SM_{LPRM} and SM_{SMOS} .

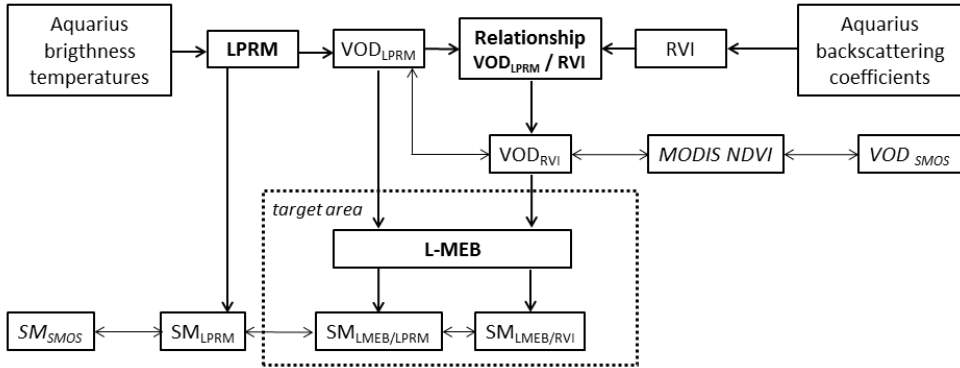


Fig. 4.1: Overview of the study concept, and the data and models used in the study. Single arrows represent the derivation of new information, while double arrows denote the comparison of datasets.

4.2.2.1 RVI

The RVI (Kim and van Zyl, 2009) uses radar backscattering coefficients of different polarizations for characterizing vegetation. It is given by

$$RVI = \frac{8\sigma_{HV}}{\sigma_{HH} + \sigma_{VV} + 2\sigma_{HV}} \quad (4.1)$$

where σ_{HV} is the cross-polarization backscattering and σ_{HH} and σ_{VV} are the co-polarized backscattering coefficients in h and v polarization, respectively, all of them in linear units. Being a measure of the randomness of the scattering, the RVI generally varies between 0 and 1, with 0 being a smooth bare surface, while an increase of vegetation cover will lead to higher roughness and therefore to increasing RVI (Kim, Y. *et al.*, 2012).

RVI is well suited for describing vegetation conditions as it has been shown to have a low sensitivity to environmental conditions, i.e. soil moisture. McColl *et al.* (2014) found, that RVI is able to reproduce vegetation patterns and seasonal cycles, but significantly overestimates biomass in dry regions. RVI depends on incidence angle, which can be neglected in this study, as only a single incidence angle is used.

4.2.2.2 LPRM

VOD_{LPRM} was calculated from Aquarius brightness temperatures with the LPRM (Owe *et al.*, 2001; Owe *et al.*, 2008). LPRM retrieves soil moisture and VOD by simulating h-polarized brightness temperature and minimizing the error to observed brightness temperature.

The forward simulation of brightness temperature is based on the radiative transfer equation of Mo *et al.* (1982). The dielectric constant k is estimated using the dielectric mixing model of Wang and Schmugge (1980). It requires information about soil parameters (sand and clay content and bulk density), which were taken from the Harmonized World Soil Database.

After calculating the surface emissivity in both polarizations from the dielectric constant through the Fresnel equations, rough surface emissivity is modeled following the method of Wang and Choudhury (1981). Input parameters for this are the polarization mixing factor Q and the roughness height h . While Q is set to 0, h is taken from the lookup table of the SMAP Algorithm Theoretical Basis Document (O'Neill *et al.*, 2014) according to IGBP land cover classes assigned to the respective grid point.

VOD is derived by an analytical approach, based on the MPDI. It is built on the assumption, that VOD is not dependent on polarization. MPDI is defined as

$$MPDI = \frac{TB_H - TB_V}{TB_H + TB_V} \quad (4.2)$$

According to Meesters *et al.* (2005), VOD τ can be described as a function of incidence angle u through MPDI and rough surface emissivities e_{rv} and e_{rh} as

$$\tau = \cos u \ln \left(ad + \sqrt{(ad)^2 + a + 1} \right) \quad (4.3)$$

where

$$a = \frac{1}{2} \left[\frac{e_{rv}(k, u) - e_{rh}(k, u)}{MPDI} - e_{rv}(k, u) - e_{rh}(k, u) \right] \quad (4.4)$$

and

$$d = \frac{1}{2} \frac{\omega}{(1 - \omega)} \quad (4.5)$$

Therefore, single scattering albedo ω is the only vegetation parameter required for the retrieval of VOD. In this study it was taken from the lookup table of the SMAP Algorithm Theoretical Basis Document (O'Neill *et al.*, 2014) according to the IGBP land cover class.

As both, VOD and soil moisture, are functions of the dielectric constant of the soil, both values are retrieved simultaneously by simulating brightness temperature and minimizing its error to observed brightness temperature.

The resulting VOD_{LPRM} and SM_{LPRM} values were smoothed spatially and temporally to eliminate noise in the retrievals. A spatial averaging within circles of 0.5° around grid points was used, corresponding to the footprint size of the Aquarius radiometer. Thereby the grid was reduced to a tenth of the grid points, which is sufficient for our study and the same observations are not repeatedly included in the analysis. A temporal smoothing was performed with a moving window of 6 weeks.

4.2.2.3 L-MEB

To test the suitability of VOD derived from RVI for soil moisture retrieval, soil moisture retrievals with VOD from RVI and with VOD_{LPRM} were performed for a test area with the L-MEB model (Wigneron *et al.*, 2007). L-MEB, which is also used in the SMOS Level 2 processor for soil moisture, is based on the $\tau - \omega$ radiative transfer equation (Mo *et al.*, 1982), just like the LPRM. However, VOD is not retrieved in the model but is required as input data, which makes it a useful tool to test the influence of different VOD values.

L-MEB aims to minimize a cost function computed of simulated and measured brightness temperatures. In the forward model, dielectric constants are simulated by the Wang dielectric model, as the same was used in the LPRM. The same input parameters as for the LPRM were used: h and ω were taken from SMAP Algorithm Theoretical Basis Document according to IGBP classes, soil data was taken from the Harmonized World Soil Database. h is corrected for polarization in the model, while ω as well as VOD were assumed to be independent of polarization and incidence angle. These simplifications may influence the results in comparison to SM_{LPRM} and SM_{SMOS} . However, the main goal is to investigate the influence of VOD_{RVI} on the retrieved soil moisture in comparison to VOD_{LPRM} , which will not be influenced by the parameterization of the model, as the same was used for both model runs.

Additionally, L-MEB needs the soil temperature in a depth of 50 cm to properly define the effective soil temperature, which was taken from the US Climate Reference Network (USCRN) provided by the International Soil Moisture Network (Dorigo *et al.*, 2013).

4.2.2.4 Sample area

One sample area was chosen to test the newly derived VOD_{RVI} in soil moisture retrieval. It is located in the United States Midwest (Fig. 4.2) and is a core test site for the SMAP calibration/validation. It shows a medium heterogeneity, as gets visible in Fig. 4.2, land use according to IGBP is mainly agriculture, grassland, and mixed forests. The area has a size of about 1,300,000 km² and consists of 960 grid points. It is part of the USCRN soil moisture network (Bell *et al.*, 2013; Diamond *et al.*, 2013). The USCRN network consists of 114 stations all over the US and measures soil moisture and soil temperature, precipitation, air temperature and surface temperature. The locations of measurement sites in and around the sample area are visible in Fig. 4.2. Soil temperature of the USCRN was used for simulating soil moisture of the sample area with L-MEB, through finding the closest station for every grid point.

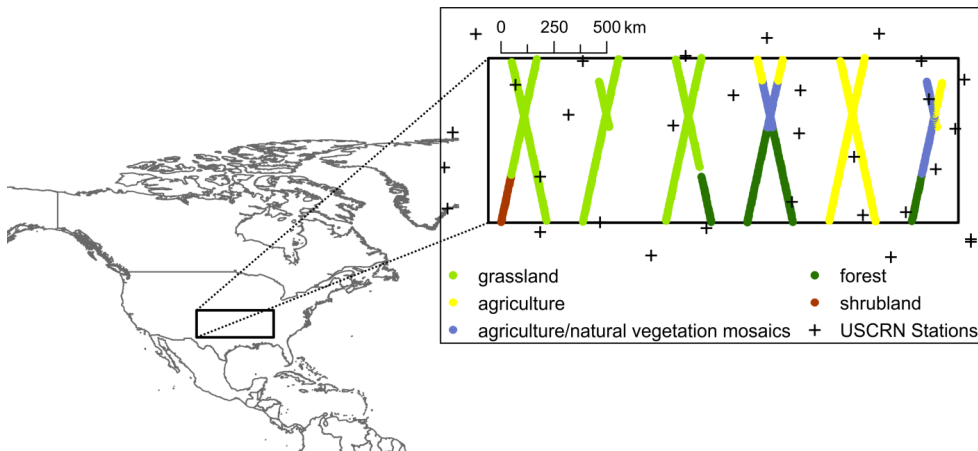


Fig. 4.2: Location and land use of the sample area and locations of USCRN stations.

4.3 Results and discussions

4.3.1 LPRM results

4.3.1.1 Vegetation optical depth

Optical depth of vegetation was derived from Aquarius brightness temperatures in the LPRM. Fig. 4.3 a) shows the distribution of the mean of VOD_{LPRM} for the whole study period. Fig. 4.3 b) and c) show the mean for VOD_{SMOS} and MODIS NDVI, respectively. All of them show a similar overall distribution of high and low values, which follows the vegetation zones of the earth. Highest deviations amongst the three can be found in the tropical region, where NDVI shows a distinctly larger region of high values than the other two. Moreover, in the tropical area, as well as in the northern polar region, VOD_{LPRM} is clearly higher than VOD_{SMOS} .

This becomes obvious in Fig 4.3 d), which shows the bias between VOD_{LPRM} and VOD_{SMOS} for all grid points. A positive bias indicates higher values of VOD_{LPRM} , a negative bias indicates higher values of VOD_{SMOS} . While in most of the world the bias is smaller than 0.1, in the northern regions values rise above 0.2. In regions with tropical rainforests and in areas with high topographic complexity, especially the Himalaya, the bias reaches even higher values, with maximum values of 0.6 for single grid points. Negative biases are mostly very small, which shows, that VOD_{LPRM} tends to have higher values than VOD_{SMOS} .

Fig. 4.3 e) provides the correlation of VOD_{LPRM} and VOD_{SMOS} for every grid point with at least 30 observation pairs in the study period. The observation pairs for the calculation of correlation coefficients, as well as for the calculation of biases, were found by assigning the VOD_{SMOS} observation with the closest date within a time interval of 2 days to every VOD_{LPRM} . The spatial patterns of correlation coefficients are not as clear as for bias. While correlation is generally high at the Sahel zone and in India, most regions contain grid points with both high and low correlation. Low correlation of VOD_{LPRM} and VOD_{SMOS} may partly result from high noise levels of VOD_{SMOS} , which were found in previous studies (Patton and Hornbuckle, 2013). They probably arise, as VOD_{SMOS} is obtained as a soil moisture inversion residual, and is therefore prone to contamination by residuals from model error. In polar regions and most of Europe no correlation could be calculated, as too few observations were available. This is due to the frequent occurrence of snow and frost and the problem with Radiofrequency Interferences.

For the correlation of VOD_{LPRM} and NDVI (Fig. 4.3 f)) values were calculated from observation pairs which were coupled by finding the closest date within one week. The time span of one week was chosen, as a sufficient number of observations pairs is needed for the analysis and both datasets

have a relatively low temporal resolution (1 week and 2 weeks for VOD_{LPRM} and NDVI, respectively), while the change within this time span is negligible. Again, correlation was only calculated for the respective grid point if at least 15 observation pairs were available for the study period. As a result, in Europe, most of Asia and a big part of North America, no correlation was calculated.

Again, the correlation coefficients do not exhibit clear spatial patterns. Still, high correlation gets obvious in the desert regions, e.g. the Sahara, while it is quite low and even gets negative in other parts. This is in particular valid for the regions of tropical rainforests and the regions where NDVI shows extreme values, while VOD_{LPRM} does not. This is probably because NDVI is already saturated in areas with moderate vegetation cover und thus cannot distinguish within this area anymore, while the L-band VOD is able to detect differences in this area.

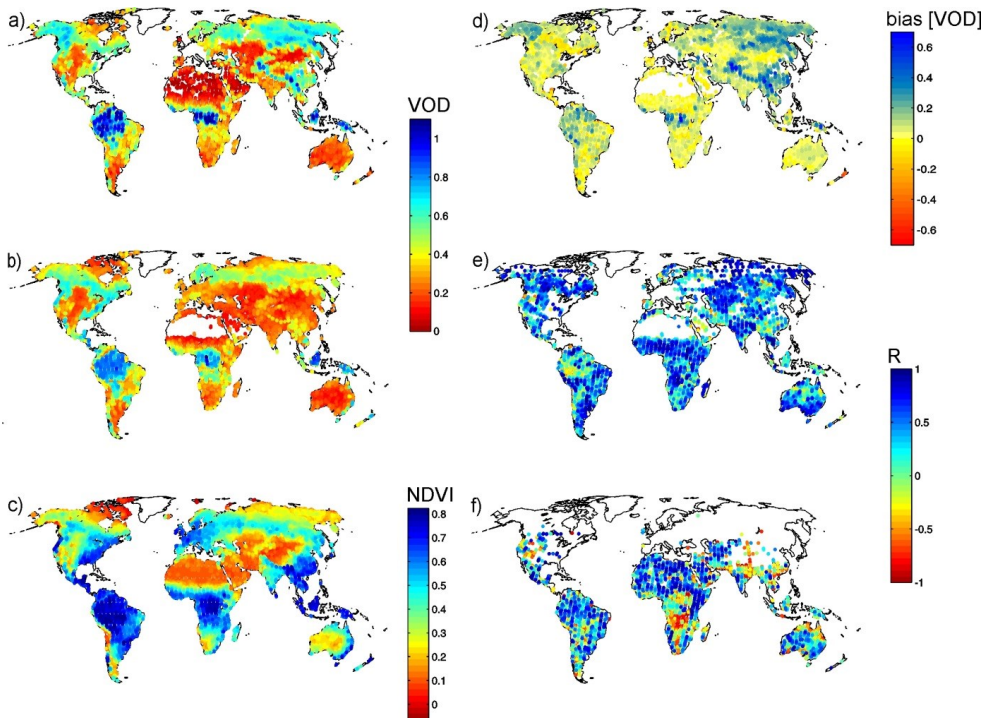


Fig. 4.3: Maps of a) VOD_{LPRM} , b) VOD_{SMOS} , c) NDVI, d) bias of VOD_{LPRM} to VOD_{SMOS} , e) correlation of VOD_{LPRM} and VOD_{SMOS} and f) correlation of VOD_{LPRM} and NDVI.

4.3.1.2 Soil moisture

In the LPRM, soil moisture is retrieved together with VOD. This is necessary, as the brightness temperature contains information about both, soil properties and vegetation and therefore both parameters have to be determined for a proper retrieval. Thus, SM_{LPRM} can be analyzed additionally to VOD_{LPRM} against SM_{SMOS} (Fig. 4.4). The overall distribution of soil moisture around the world is similar for SM_{LPRM} and SM_{SMOS} (Fig. 4.4 a) and b)). Nevertheless, SM_{SMOS} tends to be lower than SM_{LPRM} , in particular in the polar area of the northern hemisphere. Both soil moisture products are rather dry with an overall mean of soil moisture of 0.14 for SM_{SMOS} , while SM_{LPRM} exhibits overall mean soil moisture of 0.17.

Observation pairs for the calculation of bias and correlation coefficients were determined in the same way as for VOD. Biases (Fig. 4.4 c)) are generally low within $0.1 \text{ m}^3/\text{m}^3$, with an overall absolute value of $0.07 \text{ m}^3/\text{m}^3$. They tend to be highly positive in the northern parts of Asia and the American continent, where SM_{SMOS} shows distinctly lower values than SM_{LPRM} . In these regions, the retrieval of soil moisture might be more difficult because of snow and frozen soil. Although SM_{SMOS} and SM_{LPRM} are checked for snow and frost conditions, for some occasions the occurrence of snow and frost might be undetected, leading to overall higher bias in this area. Highest bias values can be found in the alpine Himalayan region, as in the maps of VOD. Again, snow and frost conditions may lead to unsuccessful retrievals in this area, together with high topographic complexity. An area with negative bias, and therefore lower soil moisture values of SM_{LPRM} than of SM_{SMOS} can be found in the African Sahel region, with values of around $-0.2 \text{ m}^3/\text{m}^3$.

Correlation coefficients of SM_{SMOS} and SM_{LPRM} (Fig. 4.4 d)) are mostly high with values over 0.8. Low values are found in desert areas, especially in the Sahara, and in the tropical rainforest areas, where also correlation coefficients of VOD_{LPRM} with VOD_{SMOS} and NDVI were low.

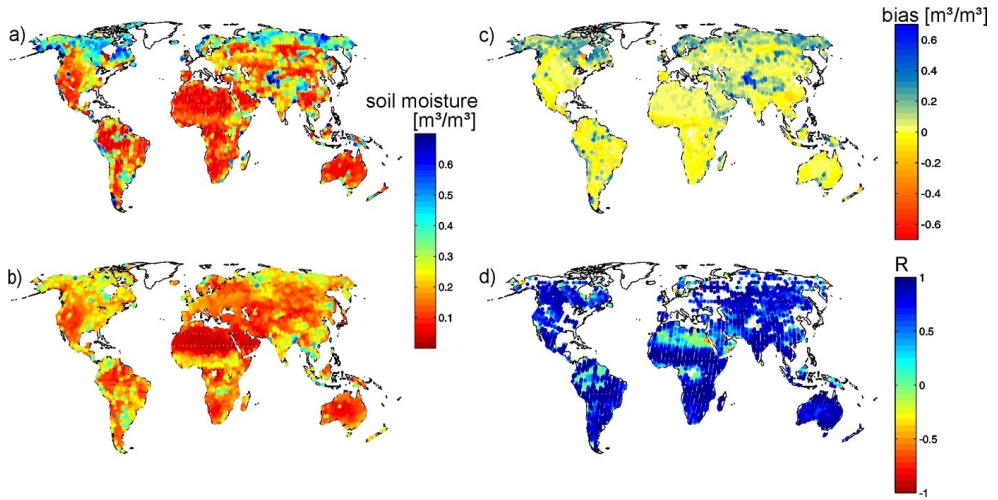


Fig. 4.4: Maps of a) SM_{LPRM} , b) SM_{SMOS} , c) bias of SM_{LPRM} to SM_{SMOS} , and d) correlation of SM_{LPRM} and SM_{SMOS} .

4.3.2 Global Relationship for RVI and VOD

The global relationship of RVI and VOD_{LPRM} , visible in Fig. 4.5, was derived from all grid points of the reduced grid and all time steps available. It is stable over time, Fig. 4.5 additionally shows the relationships for the single years of the study period, and no deviations are visible. The same result is also obtained for smaller periods, for example single months. The relationship is a 3rd order polynomial equation and is given by

$$VOD_{RVI} = \widehat{VOD}_{LPRM} = 3.8466 * RVI^3 - 5.4551 * RVI^2 + 2.6948 * RVI - 0.2230 \quad (4.6)$$

with VOD_{RVI} being the VOD retrieved from RVI and therefore corresponding to the estimator \widehat{VOD}_{LPRM} of the regression function. The coefficient of determination (R^2) is 0.65 for all grid points and all IGBP land use classes. It is higher than for a linear regression (0.50) and a 2nd order polynomial (0.57). The 4th and 5th order polynomials show only insignificantly higher R^2 values of 0.66 each.

The relationship was derived from per-pixel temporally smoothed VOD_{LPRM} and RVI values, yet the smoothing does not have an influence on the resulting equation. Tests with the unsmoothed grid points showed the same relationship; only the value of R^2 was lower.

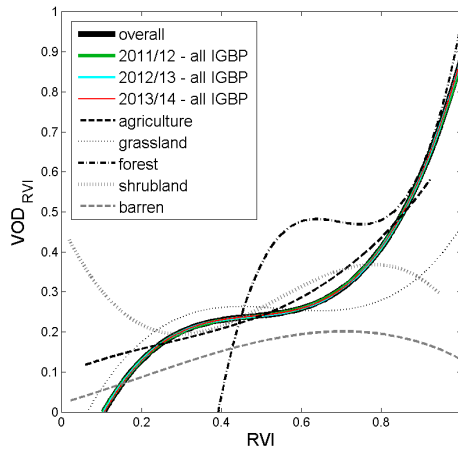


Fig. 4.5: Relationship of RVI and VOD_{LPRM} for the whole study period and all IGBP classes, for single years, and for single IGBP classes.

The relationships calculated from observations of single IGBP land use classes only were also analyzed on a global basis. The polynomials for agriculture, grassland, forest, shrubland, and barren land are also displayed in Fig. 4.5, the coefficients of the respective polynomials can be found in Table 4.1. All IGBP forest categories, evergreen needleleaf and broadleaf, deciduous needleleaf and broadleaf, and mixed forests, have been aggregated into a single category for the retrieval of the polynomial and all following analyses. The same applies to open and closed shrublands.

Most polynomials of single IGBP classes are similar to the overall relationship. In particular the agriculture polynomial shows a comparable relationship to the overall one. Deviations from the overall relationship often result from the lack of data in the respective range of RVI values for the IGBP class, the part where most RVI and VOD_{LPRM} observations are available is close to the overall relationship for most IGBP classes. The grassland polynomial is similar to the overall relationship mainly for low values of RVI, while the forest polynomial is close to the overall relationship for high RVI values > 0.8 . Higher deviations can be found for low RVI values, which is due to the lack of RVI values < 0.4 in this land use class. The polynomials of shrubland and barren land show least similarity to the overall relationship. For barren land, this might partially arise from the fact, that there are no high RVI values in the barren land class, but the polynomial deviates from the overall relationship for the whole range of RVI. The polynomial for shrubland shows highest deviations from the overall relationship for low RVI values.

Table 4.1: Coefficients of the IGBP specific polynomials starting with the leading coefficient ($p1$), i.e. $VOD_{RVI} = p1 * RVI^3 + p2 * RVI^2 + p3 * RVI + p4$.

IGBP class	p1	p2	p3	p4
Agriculture	0.87	-0.69	0.42	0.09
Grass	2.62	-4.31	2.28	-0.13
Forest	20.52	-42.91	29.69	-6.31
Shrubland	-3.03	4.90	-2.11	0.47
Barren	-1.32	1.11	0.05	0.04

It gets obvious, that the highest deviations of land use specific polynomials to the overall relationship can be found for the sparsely vegetated IGBP classes of barren land and shrubland, which is dominated by open shrubland, containing not more than 60 % vegetation cover (Friedl *et al.*, 2002). The RVI is generally a measure for the randomness of scatter (Kim, Y. *et al.*, 2012), implying that it is not exclusively influenced by vegetation, but also by soil roughness, which increases the scatter randomness as well. In IGBP classes with sparse vegetation, RVI may be highly influenced by surface roughness, and therefore the derivation of VOD from RVI may not be applicable there.

An issue with the overall relationship is the retrieval of extreme values: For RVI values between 0 and 0.1, a negative value would be obtained for VOD, which, per definition, has to be > 0 . Also, VOD values > 0.9 cannot be achieved, as long as the RVI gives values between 0 and 1.

4.3.3 VOD derived from RVI

To examine the relationship described in the previous section, VOD_{RVI} was calculated from RVI using equation (4.6). VOD_{RVI} was calculated for all grid points of the original grid.

The overall distribution of VOD_{RVI} , visible in Fig. 4.6 a), is consistent with the distribution of VOD_{LPRM} and VOD_{SMOS} (Fig. 4.3 a) and b)). Fig. 4.6 b) shows the bias of VOD_{RVI} to VOD_{LPRM} . By using VOD_{LPRM} for establishing equation (4.6), it is assumed, that VOD_{LPRM} reflects the truth. Therefore, the bias of VOD_{RVI} to VOD_{LPRM} can be seen as a relative error expressing the deviance of VOD_{RVI} from the true value.

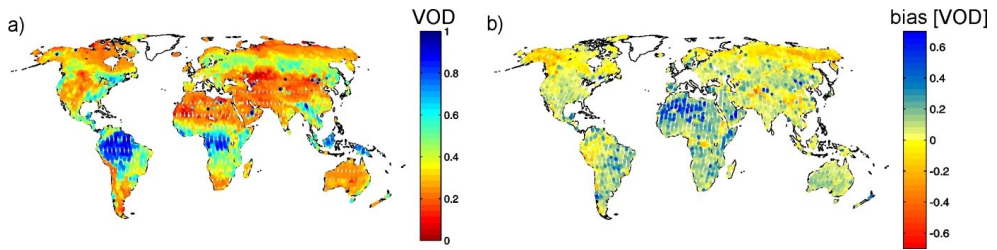


Fig. 4.6: Maps of a) VOD_{RVI} and b) bias of VOD_{RVI} to VOD_{LPRM} .

In general, the bias is within a range of ± 0.2 , with an overall absolute mean of bias of 0.13. While in the northern polar region the bias is mostly within a range of 0 to 0.1, there are also negative biases of up to 0.2, indicating lower VOD_{RVI} than VOD_{LPRM} . In contrast, most of the world shows positive bias values. On the African continent, the bias is positive, mostly around 0.2, but reaching extremely high values in the Sahara desert. This could be expected, as in the previous section it was already noticed that there is a pronounced deviation between the overall relationship and the relationship for barren land. This is induced by the influence of soil surface roughness on RVI in low vegetated areas, leading to high RVI values despite the vegetation being low, thus resulting in an overestimation of VOD_{RVI} in the respective area. In most tropical regions, especially in South America, the bias is very low with values around 0.

Mean absolute biases of VOD_{RVI} and VOD_{LPRM} for the world's most widespread IGBP land use classes can be found in Table 4.2. The lowest bias can be observed for agriculture, corresponding to the finding of Fig. 4.5, illustrating that the relationship for agriculture is very close to the overall one. Highest biases are found in the classes of shrubland and barren land.

Table 4.2 also displays the overall biases for VOD calculated from RVI with the relationships of the single IGBP classes. Highest reduction of bias can be found for forests. This is probably due to the problem that extreme values cannot be achieved with the overall relationship, as was already addressed in the previous section. The bias for grassland and agriculture did not improve, as their respective relationships are very close to the overall one. The high bias that was found for shrubland only improved by 0.1 and thus is still quite high. The global distribution of VOD_{RVI} derived from the IGBP specific polynomials, as well as the distribution of biases to VOD_{LPRM} remained quite similar (not shown).

Table 4.2: Biases between VOD_{RVI} and VOD_{LPRM} for different IGBP land use classes derived with the global relationship and with IGBP-specific relationships.

IGBP class	n	overall	IGBP
Agriculture	4568	0.06	0.06
Grass	7940	0.10	0.10
Forest	16378	0.12	0.09
Shrubland	15284	0.17	0.16
Barren	7940	0.14	0.12

Furthermore, as the relationships used in this study were all derived from VOD and RVI of the reduced grid only, it was tested, if the results of VOD_{RVI} are improving when only the reduced grid is considered. Yet, the spatial patterns of VOD_{RVI} and the respective bias to VOD_{LPRM} stayed the same, which further proofs the stability of the derived relationship of equation (4.6).

4.3.4 Performance of the optical depth retrieved from RVI in the sample area

The sample area in the US Midwest was chosen to enable a closer examination of the newly derived VOD_{RVI} . Fig. 4.7 shows the spatial patterns of mean VOD_{RVI} , VOD_{LPRM} , and VOD_{SMOS} over the entire study period in the sample area. In general, the patterns are similar for the three VODs, and they are consistent with the distribution of land use (Fig. 4.2). While the western part of the area, which mainly contains grassland, shows rather low values of VOD, the eastern part of the study area with a high part of agriculturally used land, shows medium values, with VOD_{RVI} showing slightly lower values than VOD_{LPRM} . The forest area is easily discernable with highest values of VOD, especially for VOD_{RVI} and VOD_{SMOS} . In VOD_{LPRM} , the distinction of forest from agricultural land is not that clear. Despite the aforementioned problem of the polynomial to produce high values of VOD, the values of VOD_{RVI} are partially higher than the ones of VOD_{LPRM} and come close to VOD_{SMOS} . However, highest values of VOD are around 0.7, while problems should only occur for VOD values higher than 0.85 and therefore in dense forests like tropical rainforests. Overall, the distribution of values of VOD_{RVI} tends to be closer to VOD_{SMOS} than to VOD_{LPRM} .

Kim, Y. *et al.* (2012) recommend the use of RVI for time series. Therefore, in Fig. 4.8 it is examined, whether VOD_{RVI} is able to capture the development of vegetation over time in the three most common IGBP classes of the sample area, which are agriculture, grassland, and forest. The plots show a weekly mean over all grid points of the respective IGBP class for the three VODs. Overall, the

absolute values are similar. All of them show a certain level of noise, the highest level gets visible in VOD_{LPRM} . Differences in noise levels are due to the different sources of the noise and are caused by different factors: While the noise in VOD_{LPRM} is induced by the noise of brightness temperatures and LPRM retrieval, VOD_{RVI} directly reflects the noise of RVI. Fig. 4.8 a) shows the time series of agriculture VOD, where VOD_{SMOS} is slightly lower than VOD_{LPRM} and VOD_{RVI} . Seasonal variations are only faintly visible; the overall ranges of VOD_{SMOS} and VOD_{RVI} are quite low for agricultural land use with 0.17 and 0.20, respectively. The range of VOD_{LPRM} is larger, but the seasonal cycle is superimposed by noise. Nevertheless, the accordance between VOD_{LPRM} and VOD_{RVI} is high; the overall correlation in the agriculture IGBP class is 0.77, the mean absolute bias is 0.06 and therefore the same as on global average. Fig. 4.7 d) also illustrates the correlation of VOD_{LPRM} and VOD_{RVI} for the different IGBP land use classes. The strong correlation of VODs in forests and agriculture gets obvious, while the grassland shows higher scattering and no visible relationship.

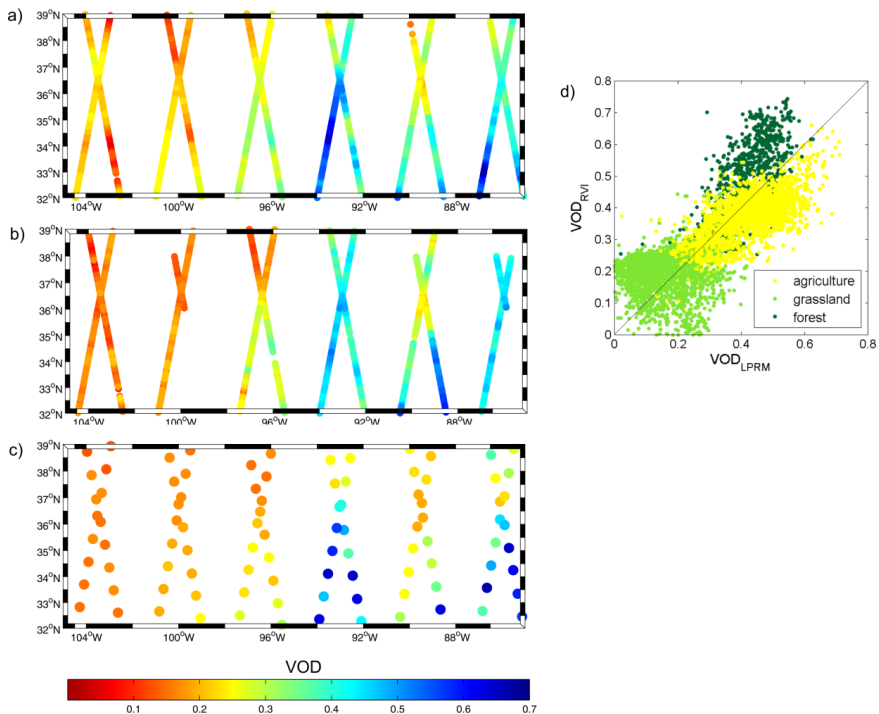


Fig. 4.7: Maps of the sample area showing a) VOD_{RVI} , b) VOD_{LPRM} , and c) VOD_{SMOS} and d) scatterplot of VOD_{LPRM} and VOD_{RVI} .

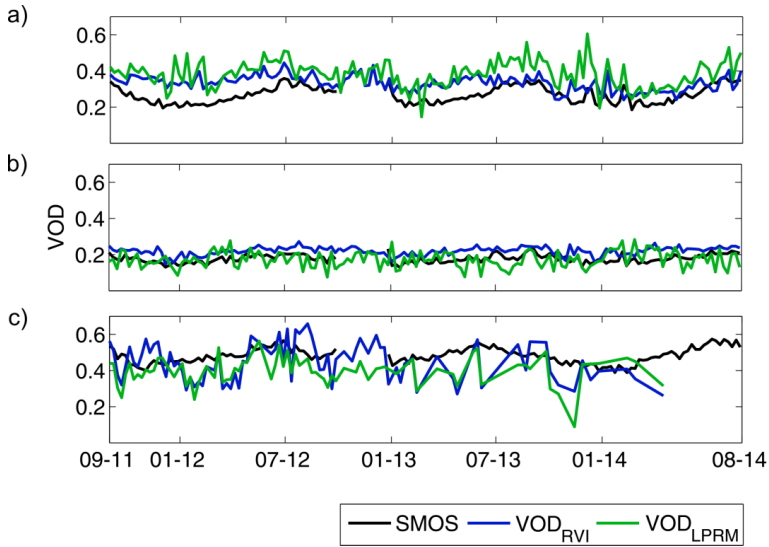


Fig. 4.8: Time series of IGBP mean of optical depth for a) agriculture, b) grassland, and c) forest.

The grassland in Fig. 4.8 b) does not show any seasonal variations, which also cannot be expected to be high in this land use class. With no visible seasonal cycle and no similarities in peaks, the development of the time series is mainly determined by the noise of the data. The overall correlation between VOD_{LPRM} and VOD_{RVI} for grassland is low with a correlation coefficient of 0.13, still, the mean absolute bias of 0.08 is lower than the global average for grassland. For forest (Fig. 4.8 c)), both, VOD_{RVI} and VOD_{LPRM} show a similarly high level of noise, while VOD_{SMOS} shows a smoother development. However, the development of VOD_{RVI} and VOD_{LPRM} is quite similar, which leads to a high correlation coefficient of 0.71. Mean absolute bias is again lower than the global average with 0.09.

The influence of VOD_{LPRM} and VOD_{RVI} on soil moisture retrieval from Aquarius brightness temperatures was tested with the L-MEB model to show the independence to the model. L-MEB requires VOD as input and as all other input parameters were kept constant, the differences in results are only due to VOD and the model selection. The means of the resulting soil moisture $SM_{LMEB/RVI}$ and $SM_{LMEB/LPRM}$ with input of VOD_{RVI} and VOD_{LPRM} , respectively, for the whole study period are visible in Fig. 4.9 a) and b). Fig. 4.9 c) and d) show means of SM_{SMOS} and SM_{LPRM} . Both L-MEB results show similar spatial patterns. Their distribution, as well as the distribution of SM_{SMOS} and SM_{LPRM} , follows the distribution of the IGBP classes and climate. The extremely low values of the western part of the grassland area is due to its location in arid climate, while its more eastern part is

located in humid climate and therefore shows medium values. In this western part of grassland $SM_{LMEB/RVI}$ exceeds the soil moisture values of the other retrievals. Forests also show rather low soil moisture values in all maps, while agriculturally used land exhibits medium to high values, the L-MEB results being higher than the others.

High values in the agricultural area can also be observed in the time series in Fig. 4.10 a), which show the weekly means of soil moisture over the agriculturally used area for SM_{SMOS} , SM_{LPRM} , and L-MEB results $SM_{LMEB/RVI}$ and $SM_{LMEB/LPRM}$. All of them exhibit a similar seasonal cycle with maximum values in December and January. While SM_{SMOS} and SM_{LPRM} show moderate peaks, the L-MEB derived soil moisture shows higher values of up to 0.76. The high values of L-MEB results, which were already observed in the soil moisture maps in Fig. 4.9, are due to the model and do not depend on VOD input, as SM_{LPRM} and $SM_{LMEB/LPRM}$ use the same VOD_{LPRM} .

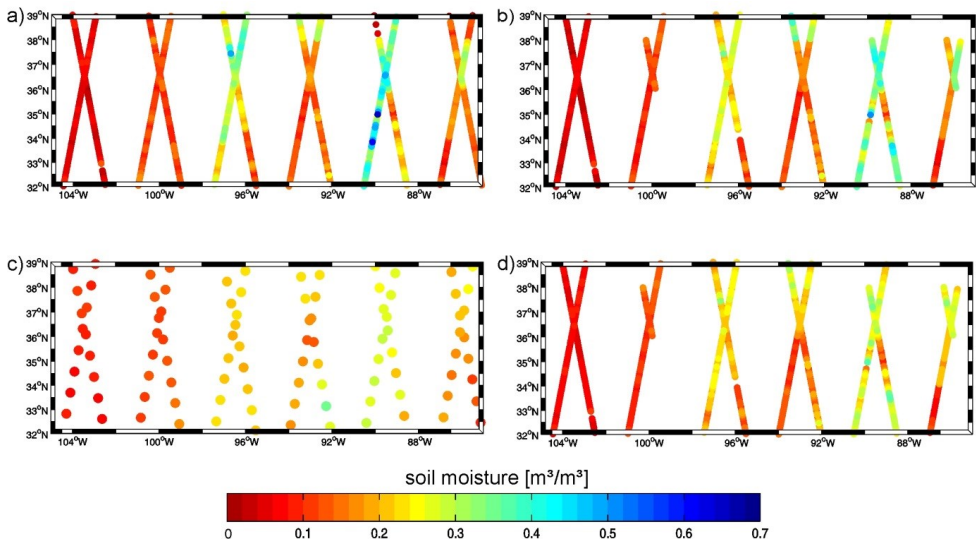


Fig. 4.9: Maps of the sample area showing soil moisture a) $SM_{LMEB/RVI}$, b) $SM_{LMEB/LPRM}$, c) SM_{SMOS} , and d) SM_{LPRM} .

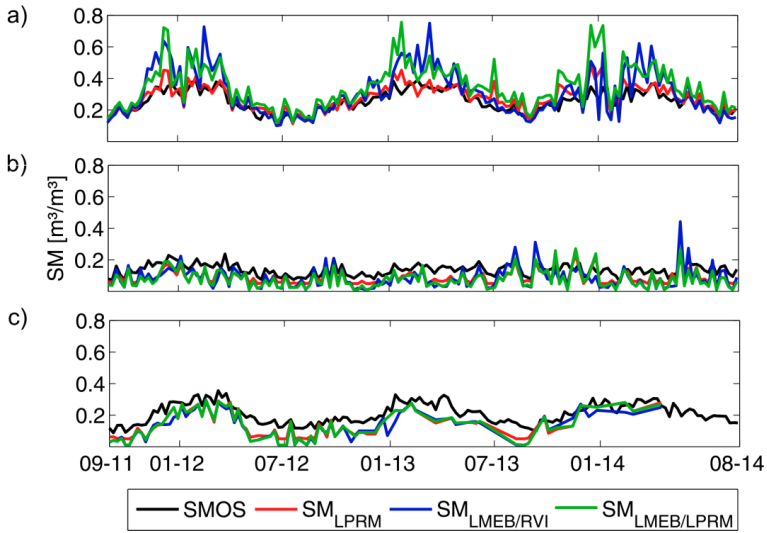


Fig. 4.10: Time series of IGBP mean of soil moisture for a) agriculture, b) grassland, and c) forest.

A similar seasonal cycle of soil moisture, even though less pronounced, is visible for forests (Fig. 4.10 c)). $SM_{LMEB/RVI}$ and $SM_{LMEB/LPRM}$ are nearly identical in this IGBP class, SM_{SMOS} is higher but again shows a lower range of the seasonal cycle, peaks (also smaller peaks) are similar for all soil moisture time series. The use of VOD_{RVI} and VOD_{LPRM} in L-MEB showed very similar results for both land use classes. The mean time series of grassland (Fig. 4.10 b)) show similarly low soil moisture for all retrievals, and similar small peaks, indicating that time series capture the development of soil moisture. Despite the low correspondence of VOD inputs (visible in Fig. 4.7 and 4.8) and their low correlation, the input of VOD_{RVI} did not influence the retrieval negatively.

Correlation coefficients of the single grid points, visible in Fig. 4.11 b), are mostly > 0.8 . This indicates that the development of time series of $SM_{LMEB/RVI}$ and $SM_{LMEB/LPRM}$ is not only similar for IGBP means, but also for single grid points. Apparently, the different VOD inputs have only minor influence on the course of time series, while they primarily affect the absolute height of soil moisture values. Therefore, the analysis of bias as the absolute measure of deviations is important.

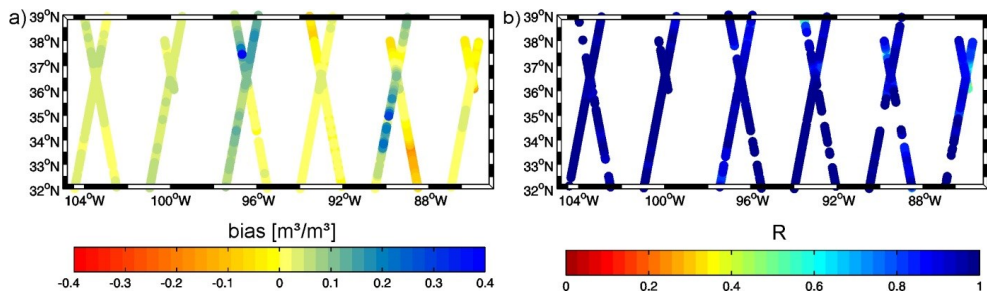


Fig. 4.11: Maps of a) bias and b) correlation coefficients of $SM_{LMEB/LPRM}$ and $SM_{LMEB/RVI}$.

While no seasonal trends are visible in the time series of bias (not shown) for any of the IGBP classes, in Fig. 4.11 a) spatial patterns of the bias between $SM_{LMEB/LPRM}$ and $SM_{LMEB/RVI}$ get visible. Low values close to zero are achieved for the forested region, while in the grassland area the values are mostly higher up to $0.1 \text{ m}^3/\text{m}^3$ and positive, meaning that the input of VOD_{RVI} leads to a slight overestimation of soil moisture compared to the input of VOD_{LPRM} . In the agricultural area, the results do not show a specific pattern. While in some parts, soil moisture retrieved with VOD_{RVI} underestimates soil moisture by up to $0.2 \text{ m}^3/\text{m}^3$, in other parts it is overestimated by values as high as $0.37 \text{ m}^3/\text{m}^3$. Some parts show low values around zero. The different results may be due to different crop types grown within this area. The small part of the study area classified as agricultural/natural vegetation mosaic (see Fig. 4.2) also shows low biases, indicating that VOD_{RVI} is also useful in areas with mixed vegetation.

VOD_{RVI} derived from the global relationship over all IGBP classes showed to be able to be used as input for soil moisture retrieval in the US Midwest area. In dry conditions, it is capable to give results with a bias $< 0.1 \text{ m}^3/\text{m}^3$, which can be observed in comparing Fig. 4.10 to Fig. 4.11. This is also the case under dense forest vegetation. In wet areas, in particular in the agriculturally used area with its different crops, however, the bias to soil moisture retrieval with different VOD input can get high.

4.4 Conclusions

This study investigated the relationship of RVI and VOD from Aquarius measurements of three years. While RVI was calculated from Aquarius backscattering coefficients, VOD was retrieved from Aquarius brightness temperatures in the LPRM through the MPDI with an analytical approach. Results show, that a global relationship over all land use classes gives a temporally stable relationship, which can be used for retrieving VOD from RVI resulting in a VOD dataset with similar spatial patterns as VOD_{LPRM} and VOD_{SMOS} . Large discrepancies were found in the IGBP classes of barren land and shrubland. This is probably resulting from the high influence of soil surface roughness on RVI in areas with sparse vegetation cover. VOD calculated from relationships for single land use classes did not show significant improvements compared to the global relationship in terms of spatial distribution and bias.

A closer examination of the relationship was performed for the Midwest area in the USA. Here, VOD distribution also follows the IGBP land use classes and is similar to VOD_{LPRM} and VOD_{SMOS} . The influence of VOD_{RVI} on soil moisture retrieval compared to VOD_{LPRM} was tested for the study area by retrieving soil moisture with the L-MEB model. Results showed similar spatial patterns and temporal development of soil moisture with both VOD inputs in the study area. High bias between the two soil moisture retrievals was found for some parts of the agriculturally used land and generally in wet areas, lower bias was found in dry areas and areas containing grassland, forest, or vegetation mosaics. While the results for soil moisture retrieval are quite variable, an empirical function independent of land use and vegetation type for the estimation of VOD can be an advantage especially for pixels of mixed land use, as it will give an overall value for the pixel according to RVI. Furthermore, the RVI can be calculated from measurements simultaneously available with brightness temperature measurements in the Aquarius and SMAP missions without the time lag auxiliary information may hold. An additional advantage for the SMAP mission is that the derivation of VOD from radar observations leads to a higher resolution than derivation from passive radiometer measurements.

5 Synthesis

5.1 Final Conclusions

Accurate remotely sensed soil moisture products are necessary for improving climate and hydrological modeling. This thesis validated two soil moisture products, the SMOS Level 2 soil moisture product and the ASCAT surface soil moisture product on catchment scale against a soil moisture reference and characterized their spatio-temporal structure on global scale. Furthermore, it addressed one major problem of the remote sensing of soil moisture, which also got obvious through the analyses in this thesis: The retrieval of soil moisture under dense vegetation showed to be complicated for both analyzed soil moisture products. This indicates that the characterization of the soil covering vegetation in the various retrieval algorithms still needs improvement. Therefore, a new method for vegetation characterization was developed in this thesis.

In chapter 2 SMOS and ASCAT soil moisture products were validated against a modeled soil moisture reference in the Rur and Erft catchments in western Germany. Furthermore, a new validation method was investigated: A temporal stability analysis was used for comparing the spatio-temporal characteristics of the different products to the modeled soil moisture reference. The ASCAT product was investigated in the original relative soil moisture and in absolute values, converted with porosity data derived from Harmonized World Soil Database. The relative soil moisture values and the ones converted into absolute soil moisture showed similar results for most analyses.

SMOS showed similar trends compared to modeled soil moisture but a temporally stable dry bias, while ASCAT showed generally higher temporal variability in the time series. The southern part of the study area, which contains a high amount of forest and a relatively high topographic complexity, exhibited a higher dry bias than the remaining part of the catchment for SMOS, and lower correlations than the remaining part of the catchment for ASCAT. The northern part, with flat terrain and mainly agricultural land use showed better results for the two products. However, the SMOS product exhibited a clear influence of RFI in the northwestern part of the study area. Regions with high RFI probability showed lower correlations and overall correlations are higher in times with less RFI. In terms of spatial patterns, absolute ASCAT values showed the most similar soil moisture distribution compared to reference soil moisture. The temporal stability analysis was found to be a useful tool for comparing spatio-temporal patterns.

In chapter 3 the SMOS and ASCAT soil moisture products were analyzed on their spatio-temporal characteristics along with the modeled ERA Interim soil moisture product on a global basis. While temporal patterns were found to be reproduced similarly well in the three products, absolute values are strongly influenced by acquisition and retrieval methods. Spatial patterns of the three products showed a different degree of impact of retrieval approaches dependent on study areas. In general, ASCAT exhibited higher soil moisture variability than SMOS, and especially than ERA. The relationship of spatial mean and variance is influenced by sensor and retrieval characteristics for the SMOS product, while ASCAT and ERA showed similar convex relationships for most regions, introduced by the precipitation patterns of the respective regions. The factors controlling the spatial variance were found to be strongly dependent on acquisition method. However, a temporal stability analysis showed similar spatial patterns mainly in climate regions with low vegetation, in particular for ASCAT and ERA products. An examination of the scaling properties of the three products showed that different support scales did not have an influence on spatial variance for any of the products. The increase of extent areas led to an increase of spatial variance for all products, most of them according to a power law, which was particularly the case for the ERA interim product.

Chapter 4 investigated the relationship of Radar Vegetation Index and vegetation optical depth, both calculated from Aquarius measurements. A global temporally stable relationship over all land use classes was established, which was then used for retrieving a VOD dataset with the same spatial patterns as the original VOD and SMOS VOD from RVI. While for most land use classes errors in the new dataset were small, high errors were found for land cover classes with sparse vegetation cover, probably due to the high influence of soil surface roughness on RVI in these regions.

In a sample area the influence of the newly derived VOD on soil moisture retrieval was tested by retrieving soil moisture with the L-MEB model. The resulting soil moisture showed similar spatial patterns and temporal development as a soil moisture retrieval with L-MEB and the input of the original VOD. As the empirical function derived in this study is independent of land use and vegetation type, it can be an advantage particularly for the retrieval of VOD for pixels of mixed land use, as it will give an overall value for the pixel. Furthermore, the VOD can be calculated from measurements simultaneously available with brightness temperature measurements in the Aquarius and SMAP missions.

In general, the two remotely sensed soil moisture products, as well as the modeled ERA Interim product, showed to be suitable for application. Nevertheless, both on catchment scale and on global scale, the products have several drawbacks, which one has to be aware of during the application on global scale or in a specific region.

The SMOS product showed to be prone to RFI, especially low-level RFI, which could not be detected by the retrieval algorithm in some regions. Complex topography and dense vegetation, in particular forests, also limit the performance of the product. Furthermore, the product exhibited to be relatively dry compared to reference and to other soil moisture products, both in temporal and spatial patterns.

The ASCAT soil moisture product showed similar difficulties with complex topography and dense vegetation. The product exhibited to be less accurate than other products in regions with dry sand, in particular in deserts, where volume scattering is high. Another problem of the product is that it is only retrieved in terms of relative soil moisture. The conversion to absolute soil moisture needs accurate soil moisture information. However, on catchment scale the relative and the derived absolute soil moisture showed similar results.

The modeled ERA Interim soil moisture product exhibited a very narrow range of soil moisture, leading to inaccuracies in areas with extreme soil moisture values. It was, for example, found to be too wet in deserts.

Both remotely sensed products showed that the retrieval of soil moisture is more prone to errors under dense vegetation, in particular in forested areas. This is an issue for all remotely sensed soil moisture products, as the vegetation influences the signal from the soil measured by active and passive sensors. This study investigated a new way of retrieving VOD from radar measurements. The method showed promising results in terms of VOD and soil moisture retrieved with this VOD. It is applicable by the Aquarius mission and the new satellite mission dedicated to soil moisture retrieval, the SMAP, which carries both a radiometer and a radar. This method is of advantage for pixels with mixed land use, as an overall value can be retrieved for the pixel. VOD can be calculated from measurements simultaneously without time lag, which might be the case with auxiliary information from optical sensors. Moreover, for the SMAP mission radar observations can provide higher resolution VOD than radiometer measurements.

5.2 Outlook

A variety of soil moisture products is operationally available at the moment. The newest products available are obtained from the SMAP mission in three different resolutions. The validation of these products will be of high importance in the near future. A validation would also be useful in the catchments of Rur and Erft, which is a challenging study area for remotely sensed soil moisture products due to its small scale heterogeneity. The validation of the new products, also in relation to the products already validated in this area, will give insight on the factors influencing the individual performance of the active, passive and merged products on different scales.

The validation of soil moisture products on catchment scale makes obvious, that application of these products on a small catchment scale is of limited use. Downscaling therefore is an important task that has to be put further effort on. The scaling behavior of SMOS, ASCAT and ERA Interim soil moisture products, which was analyzed in chapter 3, can help to improve downscaling algorithms. A further investigation on the stability of the discovered power law and the influence of study area choice on the power law would be of interest. Moreover, it would be interesting to investigate, down to which length this behavior is valid.

The temporal stability analysis, used in chapters 2 and 3, demonstrated to be a useful tool for the investigation of spatio-temporal patterns of soil moisture. However, a more detailed analysis of the influencing factors on the metrics and a study on the impact of different scales and sampling sizes on the results would be an advantage for the further use of this tool in validation activities.

First results of retrieving vegetation optical depth from radar measurements showed promising results. The next step would be a thorough analysis of the results for different land use classes and in different regions of the world. Additionally, the relationship derived in this chapter is completely dependent on the accuracy of the VOD retrieved in the LPRM, which was used for establishing its relationship to RVI. Therefore, a comprehensive error analysis of VOD from LPRM would be interesting before transferring the relationship to SMAP observations. Furthermore, the question if RVI is the best radar index for the characterization of vegetation or if the backscattering coefficient in HV polarization or other polarization ratios may contain more information about vegetation is not finally solved. Further investigation on this topic is needed.

Bibliography

- Al Bitar, A., Leroux, D., Kerr, Y.H., Merlin, O., Richaume, P., Sahoo, A., Wood, E.F. (2012): Evaluation of SMOS Soil Moisture Products Over Continental U.S. Using the SCAN/SNOTEL Network. *IEEE Trans. Geosci. and Remote Sens.* 50, 1572-1586.
- Albergel, C., de Rosnay, P., Gruhier, C., Muñoz-Sabater, J., Hasenauer, S., Isaksen, L., Kerr, Y.H., Wagner, W. (2012): Evaluation of remotely sensed and modelled soil moisture products using global ground-based in situ observations. *Remote Sens. Environ.* 118, 215-226.
- Aubert, M., Baghdadi, N., Zribi, M., Douaoui, A., Loumagne, C., Baup, F., El Hajj, M., Garrigues, S. (2011): Analysis of TerraSAR-X data sensitivity to bare soil moisture, roughness, composition and soil crust. *Remote Sens. Environ.* 115, 1801-1810.
- Balsamo, G., Viterbo, P., Beljaars, A., van den Hurk, B., Hirschi, M., Betts, A.K., Scipal, K. (2009): A Revised Hydrology for the ECMWF Model: Verification from Field Site to Terrestrial Water Storage and Impact in the Integrated Forecast System. *J. Hydrometeorol.* 10, 623-643.
- Balsamo, G., Albergel, C., Beljaars, A., Boussetta, S., Brun, E., Cloke, H., Dee, D., Dutra, E., Muñoz-Sabater, J., Pappenberger, F., de Rosnay, P., Stockdale, T., Vitart, F. (2015): ERA-Interim/Land: a global land surface reanalysis data set. *Hydrol. Earth Syst. Sci.* 19, 389-407.
- Bartalis, Z., Kidd, R., Scipal, K. (2006a): Development and Implementation of a Discrete Global Grid System for Soil Moisture Retrieval using the METOP ASCAT Scatterometer, Proceedings of the 1st EPS/MetOp RAO Workshop, Frascati, Italy.
- Bartalis, Z., Scipal, K., Wagner, W. (2006b): Azimuthal anisotropy of scatterometer measurements over land. *IEEE Trans. Geosci. Remote Sens.* 44, 2083-2092.
- Bartalis, Z., Wagner, W., Naeimi, V., Hasenauer, S., Scipal, K., Bonekamp, H., Figa, J., Anderson, C. (2007): Initial soil moisture retrievals from the METOP-A Advanced Scatterometer (ASCAT). *Geophys. Res. Lett.* 34 (20), L20401.
- Bartalis, Z., Naeimi, V., Hasenauer, S., Wagner, W. (2008): ASCAT Soil Moisture Product Handbook. ASCAT Soil Moisture Report Series No 15, Institute of Photogrammetry and Remote Sensing, Vienna University of Technology, Vienna.
- Bell, K., Blanchard, B., Schmutge, T., Witczak, M. (1980): Analysis of Surface Moisture Variations Within Large Field Sites. *Water Resour. Res.* 16, 796-810.
- Bell, J.E., Palecki, M.A., Baker, C.B., Collins, W.G., Lawrimore, J.H., Leeper, R.D., Hall, M.E., Kochendorfer, J., Meyers, T.P., Wilson, T., Diamond, H.J. (2013): U.S. Climate Reference Network Soil Moisture and Temperature Observations. *J. Hydrometeorol.* 14, 977-988.

- Berrisford, P., Dee, D., Fielding, K., Fuentes, M., Kallberg, P., Kobayashi, S., Uppala, S. (2009): The ERA interim archive. ERA Report Series. European Centre for Medium Range Weather Forecasts, Reading, United Kingdom.
- Bindlish, R., Jackson, T., Cosh, M., Zhao, T.J., O'Neill, P. (2015): Global Soil Moisture From the Aquarius/SAC-D Satellite: Description and Initial Assessment. *IEEE Trans. Geosci. Remote Sens.* 12, 923-927.
- Bircher, S., Skou, N., Kerr, Y. H. (2013): Validation of SMOS L1C and L2 Products and Important Parameters of the Retrieval Algorithm in the Skjern River Catchment, Western Denmark. *IEEE Trans. Geosci. and Remote Sens.* 51, 2969-2985.
- Bittelli, M. (2011): Measuring Soil Water Content: A Review. *HortTechnology* 21, 293-300.
- Bogena, H.R., Kunkel, R., Montzka, C., Wendland, F. (2005): Uncertainties in the simulation of groundwater recharge at different scales. *Adv. Geosci.* 5, 25-30.
- Bogena, H.R., Herbst, M., Huisman, J.A., Rosenbaum, U., Weuthen, A., Vereecken, H. (2010): Potential of Wireless Sensor Networks for Measuring Soil Water Content Variability. *Vadose Zone J.* 9 (4), 1002-1013.
- Bolten, J., Crow, W.T., Zhan, X., Jackson, T., Reynolds, C. (2010): Evaluating the Utility of Remotely Sensed Soil Moisture Retrievals for Operational Agricultural Drought Monitoring. *IEEE J. Sel. Top. Appl. Earth Observ.* 3, 57-66.
- Brocca, L., Morbidelli, R., Melone, F., Moramarco, T. (2007): Soil moisture spatial variability in experimental areas of central Italy. *J. Hydrol.* 333, 356-373.
- Brocca, L., Melone, F., Moramarco, T., Morbidelli, R. (2009a) Antecedent wetness conditions based on ERS scatterometer data. *J. Hydrol.* 364, 73-87.
- Brocca, L., Melone, F., Moramarco, T., Morbidelli, R. (2009b): Soil moisture temporal stability over experimental areas in Central Italy. *Geoderma*, 148 (3-4), 364-374.
- Brocca, L., Hasenauer, S., Lacava, T., Melone, F., Moramarco, T., Wagner, W., Dorigo, W., Matgen, P., Martínez-Fernández, J., Llorens, P., Latron, J., Martin, C., Bittelli, M. (2011): Soil moisture estimation through ASCAT and AMSR-E sensors: An intercomparison and validation study across Europe. *Remote Sens. Environ.* 115, 3390-3408.
- Brocca, L., Moramarco, T., Melone, F., Wagner, W., Hasenauer, S., Hahn, S. (2012): Assimilation of Surface- and Root-Zone ASCAT Soil Moisture Products Into Rainfall-Runoff Modeling. *IEEE Trans. Geosci. Remote Sens.* 50, 2542-2555.
- Brocca, L., Zucco, G., Mittelbach, H., Moramarco, T., Seneviratne, S.I., (2014): Absolute versus temporal anomaly and percent of saturation soil moisture spatial variability for six networks worldwide. *Water Resour. Res.* 50, 5560-5576.

- Chakrabarti, S., Bongiovanni, T., Judge, J., Nagarajan, K., Principe, J.C. (2015): Downscaling Satellite-Based Soil Moisture in Heterogeneous Regions Using High-Resolution Remote Sensing Products and Information Theory: A Synthetic Study. *IEEE Trans. Geosci. Remote Sens.* 53, 85-101.
- Chuang, T.W., Henebry, G.M., Kimball, J.S., VanRoekel-Patton, D.L., Hildreth, M.B., Wimberly, M.C. (2012): Satellite microwave remote sensing for environmental modeling of mosquito population dynamics. *Remote Sens. Environ.* 125, 147-156.
- Colliander, A. (2012): Analysis of coincident L-band radiometer and radar measurements with respect to soil moisture and vegetation conditions. *Eur. J. Remote Sens.* 45, 111-120.
- Cosh, M., Jackson, T., Bindlish, R., Prueger, J. (2004): Watershed scale temporal and spatial stability of soil moisture and its role in validating satellite estimates. *Remote Sens. Environ.* 92, 427-435.
- Daganzo-Eusebio, E., Oliva, R., Kerr, Y.H., Nieto, S., Richaume, P., Mecklenburg, S.M. (2013): SMOS Radiometer in the 1400-1427-MHz Passive Band: Impact of the RFI Environment and Approach to Its Mitigation and Cancellation. *IEEE Trans. Geosci. Remote Sens.* 51, 4999-5007.
- dall'Amico, J., Schlenz, F., Loew, A., Mauser, W. (2012): First Results of SMOS Soil Moisture Validation in the Upper Danube Catchment. *IEEE Trans. Geosci. and Remote Sens.* 50, 1507-1516.
- dall'Amico, J., Schlenz, F., Loew, A., Mauser, W., Kainulainen, J., Balling, J., Bouzinac, C. (2013): The SMOS Validation Campaign 2010 in the Upper Danube Catchment: A Data Set for Studies of Soil Moisture, Brightness Temperature, and Their Spatial Variability Over a Heterogeneous Land Surface. *IEEE Trans. Geosci. Remote Sens.* 51, 364-377.
- Das, N.N., Entekhabi, D., Njoku, E.G. (2011): An Algorithm for Merging SMAP Radiometer and Radar Data for High-Resolution Soil-Moisture Retrieval. *IEEE Trans. Geosci. Remote Sens.* 49, 1504-1512.
- Das, N.N., Entekhabi, D., Njoku, E.G., Shi, J.C.J.C., Johnson, J.T., Colliander, A. (2014): Tests of the SMAP Combined Radar and Radiometer Algorithm Using Airborne Field Campaign Observations and Simulated Data. *IEEE Trans. Geosci. Remote Sens.* 52, 2018-2028.
- de Jeu, R.A.M., Wagner, W., Holmes, T.R.H., Dolman, A.J., Giesen, N.C., Friesen, J. (2008): Global Soil Moisture Patterns Observed by Space Borne Microwave Radiometers and Scatterometers. *Surv. Geophys.* 29, 399-420.
- Dee, D.P., Uppala, S.M., Simmons, A.J., Berrisford, P., Poli, P., Kobayashi, S., Andrae, U., Balmaseda, M.A., Balsamo, G., Bauer, P., Bechtold, P., Beljaars, A.C.M., van de Berg, L., Bidlot, J., Bormann, N., Delsol, C., Dragani, R., Fuentes, M., Geer, A.J., Haimberger, L., Healy, S.B., Hersbach, H., Hólm, E.V., Isaksen, I., Kållberg, P., Köhler, M., Matricardi, M., McNally, A.P.,

- Monge-Sanz, B.M., Morcrette, J.J., Park, B.K., Peubey, C., de Rosnay, P., Tavolato, C., Thépaut, J.N., Vitart, F. (2011): The ERA-Interim reanalysis: configuration and performance of the data assimilation system. *Q. J. Roy. Meteor. Soc.* 137, 553-597.
- de Wit, A.M., van Diepen, C.A. (2007): Crop model data assimilation with the Ensemble Kalman filter for improving regional crop yield forecasts. *Agr. Forest Meteorol.* 146, 38-56.
- Diamond, H.J., Karl, T.R., Palecki, M.A., Baker, C.B., Bell, J.E., Leeper, R.D., Easterling, D.R., Lawrimore, J.H., Meyers, T.P., Helfert, M.R., Goodge, G., Thorne, P.W. (2013): U.S. Climate Reference Network after One Decade of Operations Status and Assessment. *B. Am. Meteorol. Soc.* 94, 485-498.
- Diffenbaugh, N.S., Pal, J.S., Giorgi, F., Gao, X.J. (2007): Heat stress intensification in the Mediterranean climate change hotspot. *Geophys. Res. Lett.* 34.
- Dobson, M.C., Ulaby, F.T., Hallikainen, M.T., El-Rayes, M.A. (1985): Microwave Dielectric Behavior of Wet Soil - Part II: Dielectric Mixing Models. *IEEE Trans. Geosci. and Remote Sens.* GE-23(1), 35-46.
- Dobson, M.C., Ulaby, F.T. (1986): Active Microwave Soil Moisture Research. *IEEE Trans. Geosci. Remote Sens.* GE-24, 23-36.
- Dorigo, W.A., Scipal, K., Parinussa, R.M., Liu, Y.Y., Wagner, W., de Jeu, R.A.M., Naeimi, V. (2010): Error characterisation of global active and passive microwave soil moisture datasets. *Hydrol. Earth Syst. Sci.* 14, 2605-2616.
- Dorigo, W.A., Wagner, W., Hohensinn, R., Hahn, S., Paulik, C., Xaver, A., Gruber, A., Drusch, M., Mecklenburg, S., van Oevelen, P., Robock, A., Jackson, T. (2011): The International Soil Moisture Network: a data hosting facility for global in situ soil moisture measurements. *Hydrol. Earth Syst. Sci.* 15, 1675-1698.
- Dorigo, W., de Jeu, R., Chung, D., Parinussa, R., Liu, Y., Wagner, W., Fernandez-Prieto, D. (2012): Evaluating global trends (1988-2010) in harmonized multi-satellite surface soil moisture. *Geophys. Res. Lett.* 39, L18405.
- Dorigo, W.A., Xaver, A., Vreugdenhil, M., Gruber, A., Hegyiova, A., Sanchis-Dufau, A.D., Zamojski, D., Cordes, C., Wagner, W., Drusch, M. (2013): Global Automated Quality Control of In Situ Soil Moisture Data from the International Soil Moisture Network. *Vadose Zone J.* 12 (3).
- Dorigo, W., Gruber, A., de Jeu, R., Wagner, W., Stacke, T., Loew, A., Albergel, C., Brocca, L., Chung, D., Parinussa, R., Kidd, R. (2015): Evaluation of the ESA CCI soil moisture product using ground-based observations. *Remote Sens. Environ.* 162, 380-395.
- Douville, H. (2002): Influence of soil moisture on the Asian and African monsoons. Part II: Interannual variability. *J. Climate* 15, 701-720.

- Entekhabi, D., Njoku, E., O'Neill, P., Kellogg, K., Crow, W.T., Edelstein, W., Entin, J.K., Goodman, S., Jackson, T., Johnson, J., Kimball, J., Piepmeier, J., Koster, R., Martin, N., McDonald, K., Moghaddam, M., Moran, S., Reichle, R., Shi, J., Spencer, M., Thurman, S., Tsang, L., Van Zyl, J. (2010): The Soil Moisture Active Passive (SMAP) Mission Proc. IEEE 98, 704-716.
- Escorihuela, M.J., Kerr, Y.H., de Rosnay, P., Wigneron, J.-P., Calvet, J.-C., Lemaitre, F. (2007): A Simple Model of the Bare Soil Microwave Emission at L-Band. IEEE Trans. Geosci. and Remote Sens. 45, 1978-1987.
- Escorihuela, M.J., Chanzy, A., Wigneron, J.P., Kerr, Y.H. (2010): Effective soil moisture sampling depth of L-band radiometry: A case study. Remote Sens. Environ. 114, 995-1001.
- Eumetsat (2011): SOMO 3.1.0 Product Validation Report. Eumetsat, Darmstadt, Germany.
- Famiglietti, J.S., Rudnicki, J.W., Rodell, M. (1998): Variability in surface moisture content along a hillslope transect: Rattlesnake Hill, Texas. J. Hydrol. 210, 259-281.
- Famiglietti, J.S., Devereaux, J.A., Laymon, C.A., Tsegaye, T., Houser, P.R., Jackson, T.J., Graham, S.T., Rodell, M., van Oevelen, P.J. (1999): Ground-based investigation of soil moisture variability within remote sensing footprints during the Southern Great Plains 1997 (SGP97) Hydrology Experiment. Water Resour. Res. 35, 1839-1851.
- Famiglietti, J.S., Ryu, D., Berg, A.A., Rodell, M., Jackson, T.J. (2008): Field observations of soil moisture variability across scales. Water Resour. Res. 44, W01423.
- Fang, B., Lakshmi, V (2014): Soil moisture at watershed scale: Remote sensing techniques. J. Hydrol. 516, 258-272.
- Friedl, M.A., McIver, D.K., Hodges, J.C.F., Zhang, X.Y., Muchoney, D., Strahler, A.H., Woodcock, C.E., Gopal, S., Schneider, A., Cooper, A., Baccini, A., Gao, F., Schaaf, C. (2002): Global land cover mapping from MODIS: algorithms and early results. Remote Sens. Environ. 83, 287-302.
- Gaiser, P.W., St Germain, K.M., Twarog, E.M., Poe, G.A., Purdy, W., Richardson, D., Grossman, W., Jones, W.L., Spencer, D., Golba, G., Cleveland, J., Choy, L., Bevilacqua, R.M., Chang, P.S. (2004): The WindSat spaceborne polarimetric microwave radiometer: Sensor description and early orbit performance. . IEEE Trans. Geosci. and Remote Sens. 42, 2347-2361.
- Gouveia, C., Trigo, R.M., DaCamara, C.C. (2009): Drought and vegetation stress monitoring in Portugal using satellite data. Nat. Hazards Earth Syst. Sci. 9, 185-195.
- Grayson, R., Western, A., Chiew, H., Blöschl, G. (1997): Preferred states in spatial soil moisture patterns: Local and nonlocal controls. Water Resour. Res. 33, 2897-2908.
- Green, W.H., Ampt, G.A. (1911): Studies on Soil Physics. The Journal of Agricultural Science 4(1): 1-24.
- Guillod, B.P., Orłowsky, B., Miralles, D.G., Teuling, A.J., Seneviratne, S.I. (2015): Reconciling spatial and temporal soil moisture effects on afternoon rainfall. Nat Commun. 6.

- Haarsma, R.J., Selten, F., Hurk, B.V., Hazeleger, W., Wang, X.L. (2009): Drier Mediterranean soils due to greenhouse warming bring easterly winds over summertime central Europe. *Geophys. Res. Lett.* 36.
- Hupet, F., Vanclooster, M. (2002): Intraseasonal dynamics of soil moisture variability within a small agricultural maize cropped field. *J. Hydrol.* 261, 86-101.
- Jackson, T.J., Schmugge, T.J. (1991): Vegetation Effects on the Microwave Emission of Soils. *Remote Sens. Environ.* 36, 203-212.
- Jackson, T.J., Chen, D.Y., Cosh, M., Li, F.Q., Anderson, M., Walthall, C., Doriaswamy, P., Hunt, E.R. (2004): Vegetation water content mapping using Landsat data derived normalized difference water index for corn and soybeans. *Remote Sens. Environ.* 92, 475-482.
- Jackson, T., Bidlish, R., Cosh, m.H., Zhao, T., Starks, P., Bosch, D., Seyfried, M., Moran, M.S., Goodrich, D.C., Kerr, Y.H., Leroux, D. (2012): Validation of Soil Moisture and Ocean Salinity (SMOS) Soil Moisture Over Watershed Networks in the U.S. *IEEE Trans. Geosci. and Remote Sens.* 50, 1530-1543.
- Jakkila, J., Vento, T., Rousi, T., Vehvilainen, B. (2014): SMOS soil moisture data validation in the Aurajoki watershed, Finland. *Hydrol. Res.* 45, 684-702.
- Jasper, K., Calanca, P., Fuhrer, J. (2006): Changes in summertime soil water patterns in complex terrain due to climatic change. *J. Hydrol.* 327(3-4), 550-563.
- Jung, M., Reichstein, M., Ciais, P., Seneviratne, S.I., Sheffield, J., Goulden, M.L., Bonan, G., Cescatti, A., Chen, J.Q., de Jeu, R., Dolman, A.J., Eugster, W., Gerten, D., Gianelle, D., Gobron, N., Heinke, J., Kimball, J., Law, B.E., Montagnani, L., Mu, Q.Z., Mueller, B., Oleson, K., Papale, D., Richardson, A.D., Rouspard, O., Running, S., Tomelleri, E., Viovy, N., Weber, U., Williams, C., Wood, E., Zaehle, S., Zhang, K. (2010): Recent decline in the global land evapotranspiration trend due to limited moisture supply. *Nature* 467, 951-954.
- Kerr, Y. H, Waldteufel, P., Wigneron, J.P., Martinuzzi, J.M., Font, J., Berger, M. (2001): Soil Moisture Retrieval from Space: The Soil Moisture and Ocean Salinity (SMOS) Mission. *IEEE Trans. Geosci. and Remote Sens.* 39, 1729-1735.
- Kerr, Y.H. (2006): Soil moisture from space: Where are we? *Hydrogeol. J.* 15(1), 117-120.
- Kerr, Y. H., Waldteufel, P., Wigneron, J.P., Delwart, S., Cabot, F., Boutin, J., Escorihuela, M.J., Font, J., Reul, N., Gruhier, C., Enache Juglea, S., Drinkwater, M.R., Hahne, A., Martín-Neira, M., Mecklenburg, S. (2010): The SMOS Mission: New Tool for Monitoring Key Elements of the Global Water Cycle. *Proc. IEEE* 58, 666-687.

- Kerr, Y. H., Waldteufel, P., Richaume, P., Davenport, P., Ferrazzoli, P., and Wigneron, J.P. (2011): SMOS level 2 processor soil moisture algorithm theoretical basis document (ATBD) V 3.g. CBSA, UoR, TV and INRA, Toulouse.
- Kerr, Y.H., Waldteufel, P., Richaume, P., Wigneron, J.P., Ferrazzoli, P., Mahmoodi, A., Al Bitar, A., Cabot, F., Gruhier, C., Enache Juglea, S., Leroux, D., Mialon, A., Delwart, S. (2012): The SMOS Soil Moisture Retrieval Algorithm. *IEEE Trans. Geosci. and Remote Sens.* 50(5): 1384-1403.
- Kim, S., Tsang, L., Johnson, J.T., Huang, S., van Zyl, J.J., Njoku, E.G. (2012): Soil Moisture Retrieval Using Time-Series Radar Observations Over Bare Surfaces *IEEE Trans. Geosci. and Remote Sens.* 50, 1853-1863.
- Kim, S., Liu, Y.Y., Johnson, F.M., Parinussa, R.M., Sharma, A. (2015): A global comparison of alternate AMSR2 soil moisture products: Why do they differ? *Remote Sens. Environ.* 161, 43-62.
- Kim, Y., van Zyl, J.J. (2009): A Time-Series Approach to Estimate Soil Moisture Using Polarimetric Radar Data. *IEEE Trans. Geosci. and Remote Sens.* 47, 2519-2527.
- Kim, Y., Jackson, T., Bindlish, R., Lee, H., Hong, S. (2012): Radar Vegetation Index for Estimating the Vegetation Water Content of Rice and Soybean. *IEEE Trans. Geosci. Remote Sens.* 9, 564-568.
- Konings, A., Piles, M., Rötzer, K., McColl, K.A., Chan, S., Entekhabi, D. (submitted): Vegetation Optical Depth and Albedo Retrieval using Time Series of Dual-polarized L-band Radiometer Observations. *Remote Sens. Environ.*
- Koster, R.D., Suarez, M.J., Higgins, R.W., Van den Dool, H.M. (2003): Observational evidence that soil moisture variations affect precipitation. *Geophys. Res. Lett.* 30.
- Krieger, G., Fiedler, H., Zink, N., Hajnsek, I., Younis, M., Huber, S., Bachmann, M., Gonzalez, J.H., Werner, M., Moreira, A. (2007): The TanDEM-X mission: A satellite formation for high-resolution SAR interferometry. *Europ Radar Conf*, 83-86.
- Lacava, T., Matgen, P., Brocca, L., Bittelli, M., Pergola, N., Moramarco, T., Tramutoli, V. (2012): A First Assessment of the SMOS Soil Moisture Product With In Situ and Modeled Data in Italy and Luxembourg. *IEEE Trans. Geosci. and Remote Sens.* 50, 1612-1622.
- Le Vine, D.A., Lagerloef, G.S.E., Colomb, F.R., Yueh, S.H., Pellerano, F.A. (2007): Aquarius: An instrument to monitor sea surface salinity from space. *IEEE Trans. Geosci. and Remote Sens.* 45, 2040-2050.
- Leroux, D.J., Kerr, Y.H., Richaume, P., Fieuzal, R. (2013): Spatial distribution and possible sources of SMOS errors at the global scale. *Remote Sens. Environ.* 133, 240-250.
- Li, B., Rodell, M., (2013): Spatial variability and its scale dependency of observed and modeled soil moisture over different climate regions. *Hydrol. Earth Syst. Sci.* 17, 1177-1188.

- Li, L., Gaiser, P.W., Gao, B.C., Bevilacqua, R.M., Jackson, T.J., Njoku, E.G., Rudiger, C., Calvet, J.C., Bindlish, R. (2010): WindSat Global Soil Moisture Retrieval and Validation IEEE Trans. Geosci. Remote Sens. 48, 2224-2241.
- Liu, Y., Parinussa, R., Dorigo, W., de Jeu, R., Wagner, W., van Dijk, A., McCabe, M., Evans, J. (2011): Developing an improved soil moisture dataset by blending passive and active microwave satellite-based retrievals. Hydrol. Earth Syst. Sci., 15, 425–436.
- Liu, Y., Dorigo, W., Parinussa, R., de Jeu, R., Wagner, W., McCabe, M., Evans, J., van Dijk, A. (2012): Trend-preserving blending of passive and active microwave soil moisture retrievals. Remote Sens. Environ. 123, 280-297.
- Luo, Y., Feng, X., Houser, P., Anantharaj, V., Fan, X., De Lannoy, G., Zhan, X., Dabir, L. (2013): Potential soil moisture products from the aquarius radiometer and scatterometer using an observing system simulation experiment. Geoscientific Instrumentation, Methods and Data Systems 2(1), 113-120.
- Manfreda, S., McCabe, M.F., Fiorentino, M., Rodriguez-Iturbe, I., Wood, E.F. (2007): Scaling characteristics of spatial patterns of soil moisture from distributed modelling. Adv. Water Resour. 30, 2145-2150.
- McCoy, K.A., Entekhabi, D., Piles, M. (2014): Uncertainty Analysis of Soil Moisture and Vegetation Indices Using Aquarius Scatterometer Observations. IEEE Trans. Geosci. Remote Sens. 52, 4259-4272.
- Meesters, A., de Jeu, R., Owe, M. (2005): Analytical Derivation of the Vegetation Optical Depth From the Microwave Polarization Difference Index. IEEE Trans. Geosci. Remote Sens. 2, 121-123.
- Merlin, O., Chehbouni, A., Kerr, Y.H., Goodrich, D.C. (2006): A downscaling method for distributing surface soil moisture within a microwave pixel: Application to the Monsoon '90 data. Remote Sens. Environ. 101, 379-389.
- Merlin, O., Al Bitar, A., Walker, J.P., Kerr, Y.H. (2010): An improved algorithm for disaggregating microwave-derived soil moisture based on red, near-infrared and thermal-infrared data. Remote Sens. Environ. 114, 2305-2316.
- Merlin, O., Escorihuela, M.J., Mayoral, M., Hagolle, O., Al Bitar, A., Kerr, Y.H. (2013): Self-calibrated evaporation-based disaggregation of SMOS soil moisture: An evaluation study at 3 km and 100 m resolution in Catalunya, Spain. Remote Sens. Environ. 130, 25-38.
- Miralles, D.G., Teuling, A.J., van Heerwaarden, C.C., de Arellano, J.V.G. (2014): Mega-heatwave temperatures due to combined soil desiccation and atmospheric heat accumulation. Nat. Geosci. 7, 345-349.

- Mironov, V., Kosolapova, L., Fomin, S. (2009): Physically and Mineralogically Based Spectroscopic Dielectric Model for Moist Soils. *IEEE Trans. Geosci. and Remote Sens.* 47(7): 2059-2070.
- Misra, S., Ruf, C.S. (2008): Detection of Radio-Frequency Interference for the Aquarius Radiometer. *IEEE Trans. Geosci. and Remote Sens.* 46, 3123-3128.
- Misra, T., Rana, S.S., Desai, N.M., Dave, D.B., Rajeevjyoti, Arora, R.K., Rao, C.V.N., Bakori, B.V., Neelakantan, R., Vachchani, J.G. (2013): Synthetic Aperture Radar payload on-board RISAT-1: configuration, technology and performance. *Curr. Sci. India* 104, 446-461.
- Mittelbach, H., Seneviratne, S.I. (2012): A new perspective on the spatio-temporal variability of soil moisture: temporal dynamics versus time invariant contributions. *Hydrol. Earth Syst. Sci.* 16, 2169–2179.
- Mladenova, I.E., Jackson, T.J., Njoku, E., Bindlish, R., Chan, S., Cosh, M.H., Holmes, T.R.H., de Jeu, R.A.M., Jones, L., Kimball, J., Paloscia, S., Santi, E. (2014): Remote monitoring of soil moisture using passive microwave-based techniques - Theoretical basis and overview of selected algorithms for AMSR-E. *Remote Sens. Environ.* 144, 197-213.
- Mo, T., Choudhury, B.J., Schmugge, T.J., Wang, J.R., Jackson, T.J. (1982): A model for microwave emission from vegetation-covered fields. *J. Geophys. Res.* 87(C13), 11229-11237.
- Monteith, J.L., Unsworth, M.H. (1990): *Principles of Environmental Physics*. Edward Arnold, London, UK.
- Montzka, C., Canty, M., Kunkel, R., Menz, G., Vereecken, H., Wendland, F. (2008a): Modelling the water balance of a mesoscale catchment basin using remotely sensed land cover data. *J. Hydrol.* 353, 322-334.
- Montzka, C., Canty, M., Kreins, P., Kunkel, R., Menz, G., Vereecken, H., Wendland, F. (2008b): Multispectral remotely sensed data in modelling the annual variability of nitrate concentrations in the leachate. *Environ. Modell. Softw.* 23(8), 1070-1081.
- Montzka, C., Bogena, H.R., Weihermüller, L., Jonard, F., Bouzinac, C., Kainulainen, J., Balling, J.E., Loew, A., dall' Amico, J., Rouhe, E., Vanderborght, J., Vereecken, H. (2013): Brightness Temperature and Soil Moisture Validation at Different Scales During the SMOS Validation Campaign in the Rur and Erft Catchments, Germany. *IEEE Trans. Geosci. and Remote Sens.* 51, 1728-1743.
- Morena, L.C., James, K.V., Beck, J. (2004): An introduction to the RADARSAT-2 mission. *Can. J. Remote Sens.* 30, 221-234.
- Muñoz-Sabater, J., Fouilloux, A., de Rosnay, P. (2012): Technical Implementation of SMOS Data in the ECMWF Integrated Forecasting System. *IEEE Trans. Geosci. and Remote Sens.* 9, 252-256.

- Musters, P.A.D., Bouten, W. (2000): A method for identifying optimum strategies of measuring soil water contents for calibrating a root water uptake model. *J. Hydrol.* 227, 273-286.
- Naeimi, V., Bartalis, Z., Wagner, W. (2009): ASCAT Soil Moisture: An Assessment of the Data Quality and Consistency with the ERS Scatterometer Heritage. *J. Hydrometeorol.*, 10(2), 555-563.
- Njoku, E., Entekhabi, D. (1996): Passive Microwave Remote Sensing of Soil Moisture. *J. Hydrol.* 184, 101-129.
- Oh, Y., Sarabandi, K., Ulaby, F.T. (1992): An Empirical-Model and an Inversion Technique for Radar Scattering from Bare Soil Surfaces. *IEEE Trans. Geosci. and Remote Sens.* 30, 370-381.
- Oki, T., Kanae, S. (2006): Global hydrological cycles and world water resources. *Science* 313, 1068-1072.
- Okuyama, A., Imaoka, K. (2015): Intercalibration of Advanced Microwave Scanning Radiometer-2 (AMSR2) Brightness Temperature. *IEEE Trans. Geosci. and Remote Sens.* 53, 4568-4577.
- Oliva, R., Daganzo-Eusebio, E., Kerr, Y.H., Mecklenburg, S., Nieto, S., Richaume, P., Gruhier, C. (2012): SMOS Radio Frequency Interference Scenario: Status and Actions Taken to Improve the RFI Environment in the 1400-1427-MHz Passive Band. *IEEE Trans. Geosci. and Remote Sens.* 50, 1427-1439.
- O'Neill, P., Chan, S., Njoku, E., Jackson, T., Bindlish, R. (2014): Soil Moisture Active Passive (SMAP) - Algorithm Theoretical Basis Document Level 2 & 3 Soil Moisture (Passive) Data Products. Jet Propulsion Laboratory, California Institute of Technology.
- Owe, M., de Jeu, R., Walker, J. (2001): A Methodology for Surface Soil Moisture and Vegetation Optical Depth Retrieval Using the Microwave Polarization Difference Index *IEEE Trans. Geosci. and Remote Sens.* 39, 1643-1654.
- Owe, M., de Jeu, R., Holmes, T. (2008): Multisensor historical climatology of satellite-derived global land surface moisture. *J. Geophys. Res.-Earth* 113.
- Pan, M., Sahoo, A., Wood, E.F., Al Bitar, A., Leroux, D., Kerr, Y.H. (2012): An Initial Assessment of SMOS Derived Soil Moisture over the Continental United States *IEEE J. Sel. Top. Appl. Earth Observ.* 5, 1448-1457.
- Parinussa, R.M., Holmes, T.R.H., Wanders, N., Dorigo, W.A., de Jeu, R.A.M. (2015): A Preliminary Study toward Consistent Soil Moisture from AMSR2. *J. Hydrometeorol.* 16, 932-947.
- Parrens, M., Zakharova, E., Lafont, S., Calvet, J.C., Kerr, Y.H., Wagner, W., Wigneron, J.P. (2012): Comparing soil moisture retrievals from SMOS and ASCAT over France. *Hydrol. Earth Syst. Sci.* 16, 423-440.
- Patton, J., Hornbuckle, B. (2013): Initial Validation of SMOS Vegetation Optical Thickness in Iowa. *IEEE Trans. Geosci. Remote Sens.* 10, 647-651.

- Peel, M.C., Finlayson, B.B., McMahon, T.A. (2007): Updated world map of the Köppen-Geiger climate classification. *Hydrol. Earth Syst. Sci.* 11, 1633-1644.
- Peschke, G. (1977). Ein zweistufiges Modell der Infiltration von Regen in geschichtete Böden. *Acta Hydrophysica*, XXII(1): 39-48.
- Piepmeyer, J.R., Johnson, J.T., Mohammed, P.N., Bradley, D., Ruf, C., Aksoy, M., Garcia, R., Hudson, D., Miles, L., Wong, M. (2014): Radio-Frequency Interference Mitigation for the Soil Moisture Active Passive Microwave Radiometer *IEEE Trans. Geosci. Remote Sens.* 52, 761-775.
- Piles, M., Entekhabi, D., Camps, A. (2009): A Change Detection Algorithm for Retrieving High-Resolution Soil Moisture From SMAP Radar and Radiometer Observations *IEEE Trans. Geosci. Remote Sens.* 47, 4125-4131.
- Piles, M., Camps, A., Vall-Llossera, M., Corbella, I., Panciera, R., Rudiger, C., Kerr, Y.H., Walker, J. (2011): Downscaling SMOS-Derived Soil Moisture Using MODIS Visible/Infrared Data. *IEEE Trans. Geosci. Remote Sens.* 49, 3156-3166.
- Piles, M., McColl, K.A., Entekhabi, D., Das, N., Pablos, M. (2015): Sensitivity of Aquarius Active and Passive Measurements Temporal Covariability to Land Surface Characteristics. *IEEE Trans. Geosci. Remote Sens.* 53, 4700-4711.
- Qu, W., Bogena, H., Huisman, J.A., Vereecken, H. (2013): Calibration of a novel low-cost soil water content sensor based on a ring oscillator. *Vadose Zone J.* 12 (2).
- Rawls, W.J., Brakensiek D. L. (1985): Prediction of soil water properties for hydrologic modeling. In: Jones, E.B., Ward, T.J. (eds.). *Watershed Management in the Eighties. Proc. Symp. Denver, CO. 30 Apr.–1 May 1985.* Am. Soc. Civil Eng., New York, 293–299.
- Reichle, R.H., Koster, R.D., Dong, J.R., Berg, A.A. (2004): Global soil moisture from satellite observations, land surface models, and ground data: Implications for data assimilation. *J. Hydrometeorol.* 5, 430-442.
- Reichle, R.H., Koster, R.D. (2005): Global assimilation of satellite surface soil moisture retrievals into the NASA Catchment land surface model. *Geophys. Res. Lett.* 32.
- Reichstein, M., Tenhunen, J.D., Rouspard, O., Ourcival, J.M., Rambal, S., Miglietta, F., Peressotti, A., Pecchiari, M., Tirone, G., Valentini, R. (2002): Severe drought effects on ecosystem CO₂ and H₂O fluxes at three Mediterranean evergreen sites: revision of current hypotheses? *Global Change Biol.* 8, 999-1017.
- Rodell, M., Houser, P.R., Jambor, U., Gottschalck, J., Mitchell, K., Meng, C.J., Arsenault, K., Cosgrove, B., Radakovich, J., Bosilovich, M., Entin, J.K., Walker, J.P., Lohmann, D., Toll, D. (2004): The Global Land Data Assimilation System. *B. Am. Meteorol. Soc.* 85, 381-394.

- Rodriguez-Iturbe, I., Vogel, G.K., Rigon, R., Entekhabi, D., Castelli, F., Rinaldo, A. (1995): On the spatial organization of soil moisture fields. *Geophys. Res. Lett.* 22, 2757-2760.
- Rosenbaum, U., Bogena, H., Herbst, M., Huisman, J.A., Peterson, T., Weuthen, A., Western, A., Vereecken, H. (2012): Seasonal and event dynamics of spatial soil moisture patterns at the small catchment scale. *Water Resour. Res.* 48(10), W10544.
- Rosenqvist, A., Shimada, M., Ito, N., Watanabe, M. (2007): ALOS PALSAR: A Pathfinder mission for global-scale monitoring of the environment. *IEEE Trans. Geosci. Remote Sens.* 45, 3307-3316.
- Rötzer, K., Montzka, C., Bogena, H., Wagner, W., Kerr, Y.H., Kidd, R., Vereecken, H. (2014): Catchment scale validation of SMOS and ASCAT soil moisture products using hydrological modeling and temporal stability analysis. *J. Hydrol.* 519, 934–946.
- Rowell, D.P., Blondin, C. (1990): The Influence of Soil Wetness Distribution on Short-Range Rainfall Forecasting in the West African Sahel. *Q. J. Roy. Meteor. Soc.* 116, 1471-1485.
- Rowlandson, T., Hornbuckle, B., Bramer, L., Patton, J., Logsdon, S. (2012): Comparisons of Evening and Morning SMOS Passes Over the Midwest United States. *IEEE Trans. Geosci. Remote Sens.* 50, 1544-1555.
- Rowlandson, T.L., Berg, A.A. (2015): Errors associated with estimating vegetation water content from radar for use in passive microwave brightness temperature algorithms. *Int. J. Remote Sens.* 36, 782-796.
- Ryu, D., Famiglietti, J.S. (2006): Multi-scale spatial correlation and scaling behavior of surface soil moisture. *Geophys. Res. Lett.* 33, L08404.
- Sánchez, N., Martínez-Fernández, J., Scaini, A., Pérez-Gutiérrez (2012): Validation of the SMOS L2 Soil Moisture Data in the REMEDHUS Network (Spain). *IEEE Trans. Geosci. and Remote Sens.* 50, 1602-1611.
- Saxton, K.E., Rawls, W.J. (2006): Soil water characteristic estimates by texture and organic matter for hydrologic solutions. *Soil. Sci. Soc. Amer. J.*, 70(5): 1569-1578.
- Schaefer, G.L., Cosh, M.H., Jackson, T.J. (2007): The USDA Natural Resources Conservation Service Soil Climate Analysis Network (SCAN). *J. Atmos. Ocean. Tech.* 24, 2073-2077.
- Schmugge, T., Gloersen, P., Wilheit, T., Geiger, F. (1974): Remote Sensing of Soil Moisture with Microwave Radiometers. *J. Geophys. Res.* 79, 317-323.
- Schulla, J., Jasper, K. (2007): Model Description WaSiM-ETH, Zurich.
- Scipal, K., Scheffler, C., Wagner, W. (2005): Soil moisture-runoff relation at the catchment scale as observed with coarse resolution microwave remote sensing. *Hydrol. Earth Syst. Sci.* 9, 173-183.

- Scipal, K., Drusch, M., Wagner, W. (2008): Assimilation of a ERS scatterometer derived soil moisture index in the ECMWF numerical weather prediction system. *Adv. Water Resour.* 31(8), 1101-1112.
- Seneviratne, S.I., Corti, T., Davin, E.L., Hirschi, M., Jaeger, E.B., Lehner, I., Orlowsky, B., Teuling, A.J. (2010): Investigating soil moisture–climate interactions in a changing climate: A review. *Earth-Sci. Rev.* 99, 125-161.
- Sheffield, J., Wood, E.F., Chaney, N., Guan, K.Y., Sadri, S., Yuan, X., Olang, L., Amani, A., Ali, A., Demuth, S., Ogallo, L. (2014): A Drought Monitoring and Forecasting System for Sub-Sahara African Water Resources and Food Security. *B. Am. Meteorol. Soc.* 95, 861-882.
- Sophocleous, M. (2002): Interactions between groundwater and surface water: the state of the science. *Hydrogeol. J.* 10, 52-67.
- Srivastava, P., O'Neill, P., Cosh, M., Kurum, M., Lang, R., Joseph, A. (2015): Evaluation of Dielectric Mixing Models for Passive Microwave Soil Moisture Retrieval Using Data From ComRAD Ground-Based SMAP Simulator. *IEEE J. Sel. Top. Appl. Earth Observ.*
- Su, C.-H., Ryu, D., Young, R.I., Western, A.W., Wagner, W. (2013): Inter-comparison of microwave satellite soil moisture retrievals over the Murrumbidgee Basin, southeast Australia. *Remote Sens. Environ.* 134, 1-11.
- Torres, R., Snoeij, P., Geudtner, D., Bibby, D., Davidson, M., Attema, E., Potin, P., Rommen, B., Floury, N., Brown, M., Traver, I.N., Deghaye, P., Duesmann, B., Rosich, B., Miranda, N., Bruno, C., L'Abbate, M., Croci, R., Pietropaolo, A., Huchler, M., Rostan, F. (2012): GMES Sentinel-1 mission. *Remote Sens. Environ.* 120, 9-24.
- Trenberth, K.E., Fasullo, J.T., Kiehl, J. (2009): Earth's Global Energy Budget. *B. Am. Meteorol. Soc.* 90, 311-324.
- Ulaby, F.T., Bradley, G.A., Dobson, M.C. (1979): Microwave Backscatter Dependence on Surface-Roughness, Soil-Moisture, and Soil Texture .2. Vegetation-Covered Soil. *IEEE Trans. Geosci. and Remote Sens.* 17, 33-40.
- Uppala, S.M., Kallberg, P.W., Simmons, A.J., Andrae, U., Bechtold, V.D., Fiorino, M., Gibson, J.K., Haseler, J., Hernandez, A., Kelly, G.A., Li, X., Onogi, K., Saarinen, S., Sokka, N., Allan, R.P., Andersson, E., Arpe, K., Balmaseda, M.A., Beljaars, A.C.M., Van De Berg, L., Bidlot, J., Bormann, N., Caires, S., Chevallier, F., Dethof, A., Dragosavac, M., Fisher, M., Fuentes, M., Hagemann, S., Holm, E., Hoskins, B.J., Isaksen, L., Janssen, P.A.E.M., Jenne, R., McNally, A.P., Mahfouf, J.F., Morcrette, J.J., Rayner, N.A., Saunders, R.W., Simon, P., Sterl, A., Trenberth, K.E., Untch, A., Vasiljevic, D., Viterbo, P., Woollen, J. (2005): The ERA-40 re-analysis. *Q. J. Roy. Meteor. Soc.* 131, 2961-3012.

- Vachaud, G., Passerat de Silans, A., Balabanis, P., Vauclin, M. (1985): Temporal Stability of Spatially Measured Soil Water Probability Density Function. *Soil Sci. Soc. Am. J.*, 49, 822-828.
- Van de Griend, A.A., Owe, M. (1993): Determination of Microwave Vegetation Optical Depth and Single Scattering Albedo from Large-Scale Soil-Moisture and Nimbus Smmr Satellite-Observations. *Int. J. Remote Sens.* 14, 1875-1886.
- Van de Griend, A.A., Wigneron, J.P. (2004): The b-factor as a function of frequency and canopy type at h-polarization. *IEEE Trans. Geosci. and Remote Sens.* 42, 786-794.
- van Genuchten, M.T. (1980): A Closed-form Equation for Predicting the Hydraulic Conductivity of Unsaturated Soils. *Soil Sci. Soc. Am. J.* 44(5), 892-898.
- Vanderlinden, K., Vereecken, H., Hardelauf, H., Herbst, M., Martínez, G., Cosh, M.H., Pachepsky, Y.A. (2012): Temporal Stability of Soil Water Contents: A Review of Data and Analyses. *Vadose Zone J.* 11 (4).
- Vereecken, H., Huisman, J.A., Bogaen, H., Vanderborght, J., Vrugt, J.A., Hopmans, J.W. (2008): On the value of soil moisture measurements in vadose zone hydrology: A review. *Water Resour. Res.* 44, W00D06.
- Vereecken, H., Huisman, J., Pachepsky, Y.A., Montzka, C., van der Kruk, J., Bogaen, H., Weihermüller, L., Herbst, M., Martinez, G., Vanderborght, J. (2014): On the spatio-temporal dynamics of soil moisture at the field scale. *J. Hydrol.* 516, 76-96.
- Vittucci, C., Guerriero, L., Ferrazzoli, P., Rahmoune, R., Barraza, V., Grings, F. (2013): Study of multifrequency sensitivity to soil moisture variations in the lower Bermejo basin. *Eur. J. Remote Sens.* 46, 775-788.
- Wagner, W., Lemoine, G., Rott, H. (1999a): A Method for Estimating Soil Moisture from ERS Scatterometer and Soil Data. *Remote Sens. Environ.* 70, 191-207.
- Wagner, W., Lemoine, G., Borgeaud, M., Rott, H. (1999b): A Study of Vegetation Cover Effects on ERS Scatterometer Data. *IEEE Trans. Geosci. and Remote Sens.* 37, 938-948.
- Wagner, W., Hahn, S., Kidd, R., Melzer, T., Bartalis, Z., Hasenauer, S., Figa-Saldana, J., de Rosnay, P., Jann, A., Schneider, S., Komma, J., Kubu, G., Brugger, K., Aubrecht, C., Zuger, J., Gangkofner, U., Kienberger, S., Brocca, L., Wang, Y., Blöschl, G., Eitzinger, J., Steinnocher, K., Zeil, P., Rubel, F. (2013a): The ASCAT Soil Moisture Product: A Review of its Specifications, Validation Results, and Emerging Applications. *Meteorol. Z.* 22, 5-33.
- Wagner, W., Brocca, L., Naeimi, V., Reichle, R., Draper, C., de Jeu, R., Ryu, D., Su, C.-H., Western, A., Calvet, J., Kerr, Y.H., Leroux, D., Drusch, M., Jackson, T., Hahn, S., Dorigo, W., Paulik, C. (2013b): Clarification on the "Comparison Between SMOS, VUA, ASCAT, and ECMWF Soil

- Moisture Products Over Four Watersheds in U.S.". *IEEE Trans. Geosci. and Remote Sens.* 52, 1901-1906.
- Wanders, N., Karssenber, D., de Roo, A., de Jong, S., Bierkens, M. (2014): The suitability of remotely sensed soil moisture for improving operational flood forecasting. *Hydrol. Earth Syst. Sci.* 18, 2343–2357.
- Wang, J.R., Schmugge, T.J. (1980): An Empirical-Model for the Complex Dielectric Permittivity of Soils as a Function of Water-Content. *IEEE Trans. Geosci. and Remote Sens.* 18, 288-295.
- Wang, J.R., Choudhury, B.J. (1981): Remote sensing of soil moisture content over bare field at 1.4 GHz frequency. *J. Geophys. Res.* 86, 5277-5282.
- Wang, L., Qu, J.J. (2009): Satellite remote sensing applications for surface soil moisture monitoring: A review. *Front. Earth Sci. China* 3(2), 237-247.
- Werninghaus, R., Buckreuss, S. (2010): The TerraSAR-X Mission and System Design. *IEEE Trans. Geosci. and Remote Sens.* 48, 606-614.
- Western, A., Blöschl, G. (1999): On the spatial scaling of soil moisture. *J. Hydrol.* 217, 203-224.
- Wigneron, J., Kerr, Y.H., Waldteufel, P., Saleh, K., Escorihuela, M., Richaume, P., Ferrazzoli, P., Derosnay, P., Gurney, R., Calvet, J. (2007): L-band Microwave Emission of the Biosphere (L-MEB) Model: Description and calibration against experimental data sets over crop fields. *Remote Sens. Environ.* 107, 639-655.
- Yilmaz, M.T., Crow, W.T. (2013): The Optimality of Potential Rescaling Approaches in Land Data Assimilation. *J. Hydrometeorol.* 14, 650-660.
- Zacharias, S., Bogen, H., Samaniego, L., Mauder, M., Fuß, R., Pütz, T., Frenzel, M., Schwank, M., Baessler, C., Butterbach-Bahl, K., Bens, O., Borg, E., Brauer, A., Dietrich, P., Hajsek, I., Helle, G., Kiese, R., Kunstmann, H., Klotz, S., Munch, J.C., Papen, H., Priesack, E., Schmid, H.P., Steinbrecher, R., Rosenbaum, U., Teutsch, G., Vereecken, H. (2011): A Network of Terrestrial Environmental Observatories in Germany. *Vadose Zone J.* 10 (3), 955-973.
- Zhan, X.W., Houser, P.R., Walker, J.P., Crow, W.T. (2006): A method for retrieving high-resolution surface soil moisture from hydros L-band radiometer and radar observations *IEEE Trans. Geosci. and Remote Sens.* 44, 1534-1544.
- Zhang, J.Y., Wang, W.C., Wu, L.Y. (2009): Land-atmosphere coupling and diurnal temperature range over the contiguous United States. *Geophys. Res. Lett.* 36.
- Zhao, L., Yang, K., Qin, J., Chen, Y., Tang, W., Montzka, C., Wu, H., Lin, C., Han, M., Vereecken, H. (2013): Spatiotemporal analysis of soil moisture observations within a Tibetan mesoscale area and its implication to regional soil moisture measurements. *J. Hydrol.* 482, 92-104.

Acknowledgements

This work was supported by the Federal Ministry of Economics and Technology under the Project Number 50 EE 1040. The data used in this thesis was obtained from different sources: The SMOS products were downloaded from ESA data server, the ASCAT soil moisture product has been obtained from the Vienna University of Technology and Eumetsat download portal, and the ECMWF ERA Interim data have been provided by ECMWF data server.

This work would not have been possible without the support of many people at the Agrosphere and elsewhere. I wish to thank everyone who contributed to this thesis in one way or another.

First, I would like to express my gratitude for my supervisor Prof. Dr. Harry Vereecken, head of IBG-3, for the discussions on my work, his input on this thesis and all the possibilities I had at the Agrosphere.

I particularly want to thank my “everyday” supervisor Dr. Carsten Montzka for his guidance and support. His constructive comments and the scientific discussions throughout this work were always very valuable for me. Without his constant encouragement this work would never have been finished.

Furthermore, I would like to thank Prof. Dr. Gunter Menz of the University of Bonn (Department of Geography) for taking over the co-supervision.

My stay abroad at MIT emerged a very special experience for me, both personal and professional. Therefore, I would like to express my gratitude to Prof. Dara Entekhabi of the Department of Civil and Environmental Engineering / Parsons Lab for the opportunity to work at his lab and the kind guidance and support during my stay. Many thanks to Alex Konings and Kaighin McColl for their valuable ideas and productive discussions and collaboration. Furthermore, I want to thank Pardeep Garg for mutual encouragement during our stay at Parsons.

I would also like to thank my colleagues from IBG-3. You made my time at the institute a great experience! Thanks to Thomas and Horst, for the support with all the computer stuff. Special thanks go to my fellow PhD students and friends at IBG-3, who made work and free time so enjoyable, in particular Anja, Daniela, Katrin, Laura, Maria, Markus, Michael, Nina, Sadam, Sebastian (yes, you are in here twice!), Stephan, Wei, and Wolfgang.

Last, I want to thank my family, especially my parents and my sister Sophie for their constant emotional support and encouragement. And of course, I want to thank my husband Sebastian for his love and understanding, his patience and support whenever I need it.

Band / Volume 308

Emissions of Biogenic Volatile Organic Compounds and Ozone Balance under Future Climate Conditions

C. Wu (2016), VI, 105 pp

ISBN: 978-3-95806-121-7

Band / Volume 309

Computerunterstützte Auslegung eines Brennstoffzellen-Batterie-Hybridsystems für die Bordstromversorgung

C. Krupp (2016), iii, 207 pp

ISBN: 978-3-95806-124-8

Band / Volume 310

Influence of H₂O, HCl and H₂S on the Release and Condensation of Trace Metals in Gasification

M. Benito Abascal (2016), XIX, 172 pp

ISBN: 978-3-95806-125-5

Band / Volume 311

Mechanical and Thermochemical Properties of Nano-structured Membranes for Gas Separation in Fossil-fired Power Plants

J. Zhang (2016), II, 134 pp

ISBN: 978-3-95806-126-2

Band / Volume 312

Development of Embedded Thermocouple Sensors for Thermal Barrier Coatings (TBCs) by a Laser Cladding Process

Y. Zhang (2016), II, 108 pp

ISBN: 978-3-95806-129-3

Band / Volume 313

Streamwater transit time distributions at the catchment scale: constraining uncertainties through identification of spatio-temporal controls

M. Stockinger (2016), XIX, 161 pp

ISBN: 978-3-95806-131-6

Band / Volume 314

Entwicklung eines metallbasierten Substratkonzepts für energieeffiziente Gastrennmembranen

J. A. Kot (2016), xi, 201 pp

ISBN: 978-3-95806-134-7

Band / Volume 315

**Langzeitbeobachtung der Dosisbelastung der Bevölkerung
in radioaktiv kontaminierten Gebieten Weißrusslands –
Korma-Studie II (1998 – 2015)**

P. Zoriy, H. Dederichs, J. Pillath, B. Heuel-Fabianek, P. Hill, R. Lennartz
(2016), ca 104 pp
ISBN: 978-3-95806-137-8

Band / Volume 316

**Oxidation Mechanisms of Metallic Carrier Materials
for Gas Separation Membranes**

M. Schiek (2016), 148 pp
ISBN: 978-3-95806-138-5

Band / Volume 317

**Thermoschockverhalten und temperaturabhängige Eigenschaften
kohlenstoffarmer und -freier Feuerfestwerkstoffe**

A. Böhm (2016), VI, 153 pp
ISBN: 978-3-95806-139-2

Band / Volume 318

**Theoretical and experimental studies of runaway electrons
in the TEXTOR tokamak**

S.S. Abdullaev, K.H. Finken, K. Wongrach, O. Willi (2016), X, 109 pp
ISBN: 978-3-95806-140-8

Band / Volume 319

**Modelling Thermodynamic Properties of Intercalation Compounds
for Lithium Ion Batteries**

S. O. Dang (2016), x, 133 pp
ISBN: 978-3-95806-141-5

Band / Volume 320

Atmospheric Mixing in a Lagrangian Framework

M. Tao (2016), 146 pp
ISBN: 978-3-95806-142-2

Band / Volume 321

**Statistical analysis and combination of active and passive
microwave remote sensing methods for soil moisture retrieval**

K. Rötzer (2016), XIV, 112 pp
ISBN: 978-3-95806-143-9

**Energie & Umwelt /
Energy & Environment
Band / Volume 321
ISBN 978-3-95806-143-9**

